IMAGE: A MAP OF THE STARS OF THE ORION CONSTELLATION

JournalPreview

London Journal of Engineering Research

Volume 25 | Issue 6 | Compilation 1.0

Great Britain Journals Press

WWW.JOURNALSPRESS.COM

Journal Content
In this Issue

Great Britain Journals Press

Numeric-Symbolic Composite Derivative Calculations

James Daniel Turner

ABSTRACT

Composite derivative calculations arise in many applications in computational science and engineering. Since 1857 the gold standard for computing composite derivatives is the celebrated formula of Faà Di Bruno. The equation is an identity for generalizing the chain rule of calculus to higher dimensions. It is very complicated. Each sub calculation must satisfy two integer constraint equations. An alternative problem formulation, proposed in 1861 by George Scott, is analytically very simple: nevertheless, the requirement for computing hand-generated complex derivatives while enforcing a boundary condition, has limited its application. Symbolic methods are also available, but computationally expensive to embed in application software. This paper combines the best features of symbolic processing and Scott's formulation. The symbolic preprocessor computes (1) derivatives, and (2) enforces the derivative boundary condition appearing in Scott's method. For n requested composite derivatives; the preprocessor generates a lower triangular nxn array that is embedded in the application software for computing the numerical composite derivatives. Unless the number of requested composite work derivatives increases, the preprocessor is only called one time.

Keywords: NA

Classification: FoR Code: 0102

Language: English

Great Britain Journals Press

LJP Copyright ID: 392961
Print ISSN: 2631-8474
Online ISSN: 2631-8482

London Journal of Engineering Research

Volume 25 | Issue 6 | Compilation 1.0

Numeric-Symbolic Composite Derivative Calculations

James Daniel Turner

ABSTRACT

Composite derivative calculations arise in many applications in computational science and engineering. Since 1857 the gold standard for computing composite derivatives is the celebrated formula of Faà Di Bruno. The equation is an identity for generalizing the chain rule of calculus to higher dimensions. It is very complicated. Each sub calculation must satisfy two integer constraint equations. An alternative problem formulation, proposed in 1861 by George Scott, is analytically very simple: nevertheless, the requirement for computing hand-generated complex derivatives while enforcing a boundary condition, has limited its application. Symbolic methods are also available, but computationally expensive to embed in application software. This paper combines the best features of symbolic processing and Scott's formulation. The symbolic preprocessor computes (1) derivatives, and (2) enforces the derivative boundary condition appearing in Scott's method. For n requested composite derivatives; the preprocessor generates a lower triangular nxn array that is embedded in the application software for computing the numerical composite derivatives. Unless the number of requested composite work derivatives increases, the preprocessor is only called one time. The symbolic preprocessor easily scales for handling ten's to hundred's of composite derivatives. A numerical example is provided, where 1..5 composite derivatives are computed.

Author: Amdyn Systems Inc.

I. INTRODUCTION

Composite function calculations arise in all areas of scientific and engineering computing. Low-order applications present no technical problems for manually derived calculations. High-order applications, however, rapidly become cumbersome to manage the bookkeeping involved. Alternatively, symbolic tools are available, such as Maple, Mathematica, Octave (used herein) and others, for generating arbitrary order derivative calculations. Unfortunately, run-time penalties make it is impractical to embed a algebraic symbolic program within an application program. Since *1857* the work of Faa Di Bruno [1],[2],[3] has served as the gold standard for computing composite derivatives. This work combines the power of symbolic computing with the simple elegance of George Scott's *1861* formulation [4]. For five requested composite derivative calculations, the symbolic software generates a *5x5* lower triangular array, that is embedded in the application software for computing numerical derivative values. A numerical example is provided to demonstrate the effectiveness of the proposed algorithm.

1.1 Faa Di Bruno Formulation

Since 1857 scalar composite function calculations have been theoretically handled by invoking the celebrated work of *Faà* Di Bruno [1],[2],[3]. His formula for computing the *nth* derivative of the function $u = F\left(G\left(x\right)\right)$ is given by

London Journal of Engineering Research

$$\frac{d^n}{dx^n}F\left(G\left(x\right)\right)=\sum\frac{n!}{b_{1!}b_{2!}...b_{n!}}F^{(k)}\left(G\left(x\right)\right)\left(\frac{G'}{1}\right)^{b_1}\left(\frac{G''}{1.2}\right)^{b_2}\left(\frac{G'''}{1.2.3}\right)^{b_3}...\left(\frac{G^{(n)}}{1.2...n}\right)^{b_n}$$

where the summation process is subject to the following integer constraint conditions

$$b_1+b_2+b_3+...+b_n=k$$
$$b_1+2b_2+3b_3+...+nb_n=n$$

No additional derivative calculations are required. Not surprisingly the calculation represents a daunting bookkeeping challenge.

1.2 Scott's Composite Derivative Formulation

In 1861 George Scott [4] proposed the following alternative composite function derivative formulation

$$\frac{d^n}{dx^n}F\left(G\left(x\right)\right)=\sum_{k=1}^{n}\frac{F^{(k)}\left(G\left(x\right)\right)}{k!}\left\{\frac{d^n}{dx^n}G^k\left(x\right)\right\}\Bigg|_{G=0} \tag{1}$$

which is analytically much simpler than *Faà* Di Bruno's identity. Unfortunately, the requirement for generating hand-derived derivatives for $\frac{d^n}{dx^n}G^k\left(x\right)\Big|_{G=0}$, where n denotes the nth derivative and k denotes derivative summation index, has limited its broader application in the computational research community.

II. NUMERIC-SYMBOLIC COMPOSITE DERIVATIVE FORMULATION

This paper presents a composite derivative algorithm that combines: (1) the simplicity of Scott's formulation [4], and, (2) the power of algebraic symbolic manipulation. Only two function routines are required (see Figure 1 and Appendix A). Symbolic function derivatives are computed for a generic *G(x)* function. The use of a generic function (see Figure 1), eliminates the need for embedding a symbolic program in the application software. The algorithm consists of two parts. First, a symbolic preprocessor (see Figure A) computes the derivatives for $\frac{d^n}{dx^n}G^k\left(x\right)\Big|_{G=0}$ and enforces a *G=0* boundary condition on each derivative. The derivative calculations become very complicated as the requested number of composite derivatives increase. Nevertheless, after the boundary condition *G=0* is enforced, the elements of the output derivative array are very simple. The symbolically generated derivative array consists of a lower triangular *nxn* array; which is copied into the application software for numerical derivative calculations. The elements of the array consist of components of the vector array {V1 V2 ...Vn}, where Vi denotes $\frac{d^i}{dx^i}G$. The array is only recomputed if the number of requested derivative increases.

Second, the application program embeds the computational function routine appearing in *Figure 1*, for numerically computing the composite derivatives. An *elegantly* simple double summation algorithm generates the numerical results for the composite derivatives.

For *nd = five* requested composite derivatives, the symbolic preprocessor, presented in Appendix A, generates the following *dGdx* lower triangular *nd* x *nd* array:

$$dGdx = \begin{bmatrix} V_1 & & & & \\ V_2 & 2V_1^2 & & & \\ V_3 & 6V_1V_2 & 6V_1^3 & & \\ V_4 & 8V_1V_3+6V_2^2 & 36V_1^2V_2 & 24V_1^4 & \\ V_5 & 10V_1V_4+20V_2V_3 & 60V_1^2V_3+90V_1V_2^2 & 240V_1^3V_2 & 120V_1^5 \end{bmatrix} \tag{2}$$

where $Vi = \frac{d^iG}{dx^i}\Big|_{G=0}$. The *dGdx* array of Eq. 2 enables 1 through 5 composite derivatives to be evaluated. Elements of the array are nonlinear, for example, the element *dGdx*(4,2) = $8V_1V_3+6V_2^2$. During the preprocessing operations, the following change of variables eliminates potential problems with Processing the nonlinear terms:

$$\{G' \quad G'' \quad G''' \quad G^{(4)} \quad G^{(5)}\} = \{V_1 \quad V_2 \quad V_3 \quad V_4 \quad V_5\}$$

The change of variables substitution starts with the highest order derivative and continues until the lowest order derivative variable has been replaced (see Appendix A).

An additional benefit of this approach is that for applications only requiring three composite derivatives, one only uses the sub portion of the array dGdx(1:3,1:3) for all numerical derivative calculations.

III. COMPOSITE DERIVATIVE CALCULATIONS

Taking the symbolically generated *dGdx* array of Eq. 2 as input for the application software; composite derivatives are computed with following *function routine*:

Function Composite = Derivative(nd, x, *DF*, *DG*, *Rfac*)

%% This function computes composite derivatives for nd derivatives.
%% The Maximum number of derivatives is five(5), otherwise the
%% symbolic preprocessor is recomputed to generate a new *dGdx* array.

%% *INPUT*:

%% nd number of composite derivatives requested
%% x evaluation point for the composite derivative

%% $DF = \{F' \quad F'' \quad F''' \quad F^{(4)} \quad F^{(5)}\}\Big|_{F|_{G|=x}}$

%% $DG = \{G' \quad G'' \quad G''' \quad G^{(4)} \quad G^{(5)}\}\Big|_{G(x)}$

%% where *x* denotes the evaluation point for the derivatives
%% *DF & DG* are *user supplied nd x 1* arrays of derivatives numerically
%% evaluated at the application points
%% *Rfac* = reciprocal factorial array *nd x 1*
%% *OUTPUT*:

%% *Composite* denotes the *nd x 1* array of requested composite derivatives
%%==========

%%==========

$$V_1 = DG(1);\ V_2 = DG(2); V_3 = DG(3); V_4 = DG(4); V_5 = DG(5);$$

%% Introduce Current G(x) Derivative values in the following *dGdx* array

%% *dGdx* is copied from the symbolic preprocessor of *Appendix A*

$$dGdx(1,\ 1) = V_1,\ dGdx(2,\ 1) = V_2,\ dGdx(3,\ 1) = V_3,\ dGdx(4,\ 1) = V_4,\ dGdx(5,\ 1) = V_5$$
$$dGdx(2,\ 2) = 2V_1^2$$
$$dGdx(3,\ 2) = 6V_1V_2$$
$$dGdx(4,\ 2) = 8V_1V_3 + 6V_2^2$$
$$dGdx(5,\ 2) = 10V_1V_4 + 20V_2V_3$$
$$dGdx(3,\ 3) = 6V_1^3$$
$$dGdx(4,\ 3) = 36V_1^2V_2$$
$$dGdx(5,\ 3) = 60V_1^2V_3 + 90V_1V_2^2$$
$$dGdx(4,\ 4) = 24V_1^4$$
$$dGdx(5,\ 4) = 240V_1^3V_2$$
$$dGdx(5,\ 5) = 120V_1^5$$

```
%% Begin Main Derivative Summation Loop
for n = 1:nd     %% Number of requested composite derivatives
    s = 0;       %% initialize each derivative summation
   for k = 1:n   %% Number of summation terms for each derivative
       s = s  +  DF(k)*dGdx(n,k)*Rfac(k);
   endfor        %% Sum current Derivative Series Expansion
   Composite(n) = s; %% Save nth value of the composite derivative
endfor %% double summation algorithm
endfuction
```

Figure 1: Numerical Composite Derivative Function Routine

This double summation algorithm is extremely simple when compared with Faa Di Bruno's formulation [1],[2],[3].

IV. NUMERICAL APPLICATION

This Section presents a numerical composite derivative example, where *five(5)* composite derivatives are requested. The assumed composite derivative function is given by:

$$\frac{d^n}{dx^n} F\left(G(x)\right) = \tan\left(\cosh(x)\right)\Big|_{x=0.5} \tag{3}$$

There are two numerical evaluation points for the function appearing in Eq. (3). Namely,
Evalpt = 0.5 for G(Evalpt), and
FEvalpt = cosh(Evalpt)

The user is assumed to have provided numerical values for the following analytic derivative arrays for *F* & *G*:

$$DF = \left\{ F' \quad F'' \quad F''' \quad F^{(4)} \quad F^{(5)} \right\}\Big|_{\cosh(x)} \tag{4}$$

$$DG = \left\{ G' \quad G'' \quad G''' \quad G^{(4)} \quad G^{(5)} \right\}\Big|_{x} \tag{5}$$

These numerical arrays are processed in the double summation algorithm presented in *Figure 1*. Assuming that the evaluation point for the composite derivative is *x=0.5*, the above derivative arrays have the following truncated numerical values

$$DF = \begin{bmatrix} 3.5495\text{e+}00 & 1.1335\text{e+}01 & 6.1395\text{e+}01 & 4.3746\text{e+}02 & 3.9112\text{e+}03 \end{bmatrix}$$

$$DG = \begin{bmatrix} 1.5056\text{e-}01 & 1.0113\text{e+}00 & 1.5056\text{e-}01 & 1.0113\text{e+}00 & 1.5056\text{e-}01 \end{bmatrix}$$

Using the double summation algorithm presented in *Figure 1*, the five requested composite derivatives are given by:

$$CD = \begin{bmatrix} 5.3442\text{e-}01 & 3.8464\text{e+}00 & 5.9215\text{e+}00 & 4.8062\text{e+}01 & 1.8572\text{e+}02 \end{bmatrix}$$

which have been crossed checked with purely symbolic derivative calculations.

V. CONCLUSION

This work links (1) the power of symbolic processing for computing derivative values for $\frac{d^n}{dx^n} G^k(x)\Big|_{G=0}$ and the simplicity of Scott's algorithm presented in Eq. (1). Numerical composite derivative calculations are preformed using the elegantly simple double summation algorithm presented in *Figure 1*. Up to five composite derivatives are handled by the algorithm. If more composite derivatives are required; the symbolic preprocessor of Appendix A is recomputed to generate an updated derivative array for *dGdx*. The symbolic preprocessor performs derivative calculations and enforces a boundary condition on each derivative. The output of the symbolic preprocessor consists of a lower triangular 5x5 matrix. The elements *dGdx* functionally depend on the nonlinear derivatives of generic function *G(x)* . The derivative array *dGdx* is embedded in function routine presented in *Figure 1* for computing the numerical composite derivatives. Assuming that the upper limit for the requested number of composite derivatives does not change; the preprocessor is only executed one time. The algorithm scales for tens to hundreds of composite derivatives. A numerical example is presented that demonstrates the effectiveness of the proposed methodology.

REFERENCES

1. Faa di Bruno, "Noet sur une nouvelle formule de calcul differntiel," Quart. J. Pure Appl. Math. 1 (1857) pp. 359-360.
2. S. Roman, "Faa di Bruno's formula," The Mathematical Association of America, Monthly, Vo. 87, No. 10. (Dec., 1980), pp. 805-809.
3. Warren P. Johnson, "The Curious History of Faá di Bruno's formula," The Mathematical Association of America, Monthly 109, March 2002, pp. 217-234.
4. George Scott, "Formulae of successive differentiation," Quaterly J. Pure Appl. Math. Vol. 4, (1861), pp. 77-92.

London Journal of Engineering Research

APPENDIX A

Symbolic Constrained Derivative Preprocessor

This function routine uses symbolic processing to compute and enforce derivative boundary conditions. A generic function is used to generate the derivatives and enforce boundary conditions on $\left.\frac{d^n}{dx^n} G^k(x)\right|_{G=0}$. The use of a generic function *G(x)* eliminates the need for embedding a symbolic manipulation tool in the application software. The generation of symbolic derivatives is straight forward. Enforcing the *G=0* boundary condition of the derivative expressions requires an indirect approach to avoid a potential loss of nonlinear terms. This is handled by introducing a change of variables to eliminate the explicit derivative expressions in the symbolic derivative results. The calculation is started by eliminating the highest derivatives first. The calculation generates a lower triangular array *dGdx*, that is inserted in the application software as the function routine appearing in *Figure 1*. This array is computed only one time, and is only recomputed if the number of requested composite derivative increases.

```
function dgk = Sym_dGdk_preprocessor ( nd )
%% Symbolic PreProcessor for composite derivatives
%% Math Model:  phi = f( g(x) ), @ x = evaluation point
%% INPUT: nd number of implicit derivatives required on output
%%=====================================================
%% INPUT:      nd Number of implicit derivatives required
%% OUTPUT: dgk nxn lower triangular array of derivatives @ G = 0
%% COPYRIGHT (2025) James D. Turner Allrights reserved
syms G(x);       %% Declare variables to be symbolic
syms k;
%% Create change of variables array to eliminate analytic dervs:
symbols = sym( zeros( 1, nd ) ); % Preallocate symbolic array
for i = 1:nd
   symbols(i) = sym( sprintf('v%d', i));
   % Create symbols = { v1, v2, ..., vn }
End  %% => ( G' = V1, G'' = V2, ...,G(n) = Vn )

old   = sym ( zeros( nd,1) );
new = sym ( zeros( nd,1) );     %% allocate memory for derivative transformations

for i = 1:nd
 old(i,1)  = diff( G(x), x, i );     %% Load G derivatives
 new(i,1) = symbols(i) ;          %% Load { v1, v2, ..., vn }
endfor                           %% Store derivative transformation equations
oldr  =  old( end:-1:1 );
newr =  new( end:-1:1 );           %% Reverse order of derivative & V arrays
dgk  = sym( zeros( nd, nd ) );     %% allocate array for enforcing G = 0 BC
    %%================================
    %% Symbolic Preprocessor Loop
    %%================================
for n  = 1:nd                      %% n-th derivative loop
 for k = 1:n                       %% summation terms for each derivative
```

```
   deriv = diff( G(x)^k, x, n );      %% compute nth derivative ( vary complicated )
   ans   = expand( deriv );           %% ans = { G^(n)*f0 + G^(n-1)*f1 + ... + fn }
   ans   = subs( ans, oldr, newr );  %% change of variables for higher derivatives
   G_BC  = subs( ans, G(x), 0);    %% enforce G = 0 Boundary Condition
   dgk( n, k ) = [ G_BC ];           %% save nk th element of constrained derivative array
    endfor
endfor
endfunction
```

This page is intentionally left blank

Wave Energy Considerations for the Concept Design of Rock Armored Coastal Revetments

Alexander Nielsen

ABSTRACT

Current practice for assessing toe scour, requisite armor mass and wave overtopping of rock-armored coastal revetments is based empirically on flume study data. Flume data are normalized, which is done to synthesize large datasets to a notionally common scale, making equations dimensionless. Factors that normalize laboratory data for developing current predictive formulae for scour, requisite armor mass and overtopping discharges are based universally on wave height and gravitational acceleration. This article utilizes data from comprehensive scale model studies of various rock armored coastal revetments from which current-practice formulae have been derived, but normalizing the laboratory data using factors based on wave energy rather than wave height alone. This has resulted in predictions of toe scour, requisite armor mass and average overtopping discharges that are more accurate than those from formulae in current use. The influence of wave period is examined with wave period being incorporated into predictive equations, resulting in further improvements. Some model and scale effects are identified, recommending further research.

Keywords: coastal revetment, rock armor, toe scour, requisite armor mass, overtopping discharge, wave energy.

Classification: DDC Code: 627.58

Language: English

Great Britain Journals Press

LJP Copyright ID: 392962
Print ISSN: 2631-8474
Online ISSN: 2631-8482

London Journal of Engineering Research

Volume 25 | Issue 6 | Compilation 1.0

Wave Energy Considerations for the Concept Design of Rock Armored Coastal Revetments

Alexander Nielsen

ABSTRACT

Current practice for assessing toe scour, requisite armor mass and wave overtopping of rock-armored coastal revetments is based empirically on flume study data. Flume data are normalized, which is done to synthesize large datasets to a notionally common scale, making equations dimensionless. Factors that normalize laboratory data for developing current predictive formulae for scour, requisite armor mass and overtopping discharges are based universally on wave height and gravitational acceleration. This article utilizes data from comprehensive scale model studies of various rock armored coastal revetments from which current-practice formulae have been derived, but normalizing the laboratory data using factors based on wave energy rather than wave height alone. This has resulted in predictions of toe scour, requisite armor mass and average overtopping discharges that are more accurate than those from formulae in current use. The influence of wave period is examined with wave period being incorporated into predictive equations, resulting in further improvements. Some model and scale effects are identified, recommending further research.

Keywords: coastal revetment, rock armor, toe scour, requisite armor mass, overtopping discharge, wave energy.

Author: Worley Consulting, Sydney, Australia.

I. INTRODUCTION

1.1 Background

Coastal revetments are designed to protect shoreline assets from the natural processes of wave erosion and inundation. Generally, they are located in shallow nearshore waters, subjected to depth-limited breaking waves *(Figure 1)*.

The breakers may be spilling, plunging or surging *(Figure 2)*, depending upon the steepness of the incident breaking waves and the bed slope upon which they are shoaling and breaking, that is, the breaking wave surf similarity parameter (or breaking wave Iribarren Number), ξ_b:

$$\xi_b = \frac{m}{\sqrt{H_b/L_0}} \tag{1}$$

where m is the tangent of the bed slope α (-), H_b is the breaking wave height (m) and L_0 is the deepwater wavelength (m), given by $gT_p^2/2\pi$[1] (pII-I-66) where g is gravitational acceleration (m/s²) and T_p is the wave period (s). Spilling breakers occur when $\xi_b < 0.4$, plunging breakers when $0.4 \leq \xi_b \leq 2.0$ and surging breakers when $\xi_b > 2.0$.[2] On steep to flat slopes in shallow water around 2-4 m depth $H_b \approx 1.4\ H_s$.[3](p91)

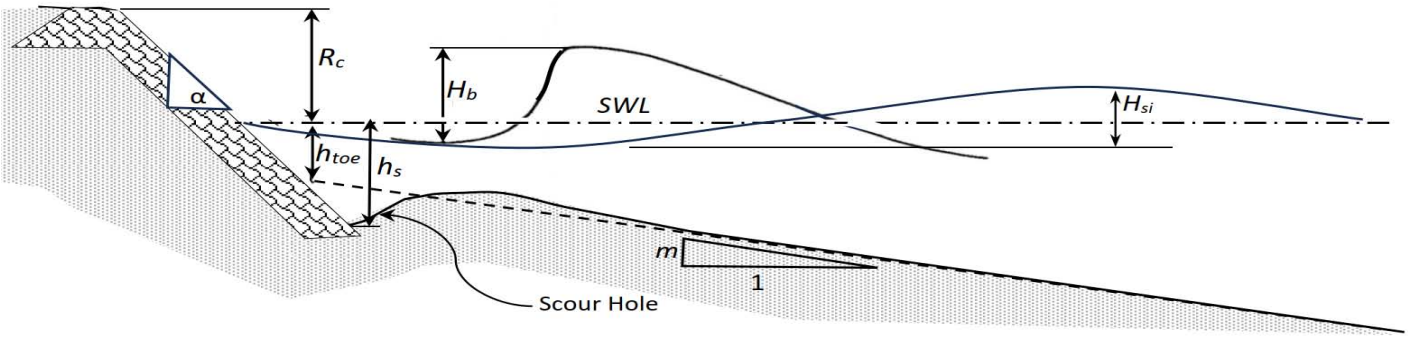

Figure 1: Definition schema for depth-limited waves breaking onto a rock armored coastal revetment (distorted scale, *SWL* is still water level, H_{si} is incident significant wave height).

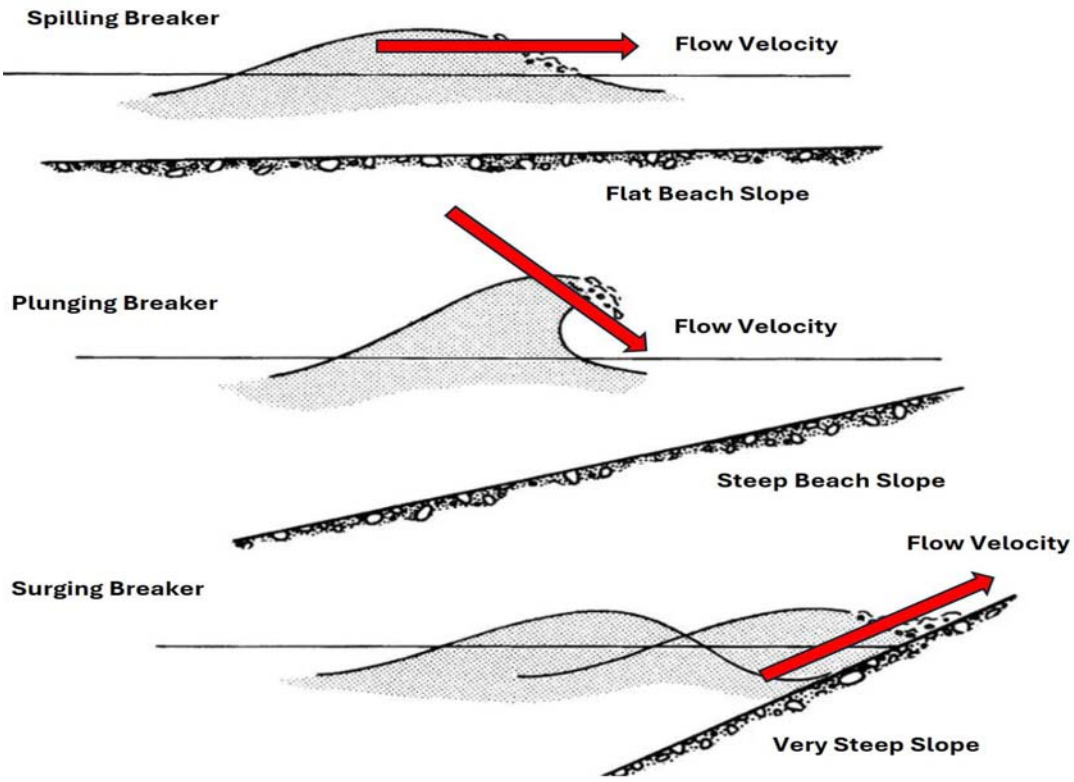

modified from [4](Figure 27)

Figure 2: Types of breaking waves

Hydrodynamic considerations for the design of rock armored coastal revetments include:

- Seabed scour
- Armour stability
- Wave overtopping.

Further consideration may need to be given to the design methodology, with much current practice relying on scale modelling results.

These considerations deal with natural random processes that cannot be determined accurately. This behoves conservatism in design, which may depend upon the appetite adopted for the level of risk, which will be informed by the available data, confidence in theoretical understanding, empirical evidence, and confidence in climate change predictions. Factors of safety are adopted, and empirical data are enveloped by design equations with acceptable levels of non-exceedance.

1.2 Seabed Toe Scour

The Coastal Engineering Manual (CEM) presents a simple "rule-of-thumb" that serves as an engineering guideline for sloping revetments under breaking waves, a conservative estimate being:[1](p.VI-5-236-237)

$$h_s = H_{max} \tag{2}$$

where h_s is the toe scour depth (m) below the still water level (*SWL*), H_{max} is the maximum wave height sustainable in the water depth (m).

Assuming H_{max} = 1.4 H_s, data from moveable bed model studies of toe scour at sloping revetments over a large range of scales are presented in *Table 1* and *Figure 3*.[5-10]

Table 1: Scour data from movable bed flume model studies for sloping revetments[5]

Researcher (Revetment slope V:H)	Test No. (-)	H_{si} (m)	h_{toe} (m)	m (-)	T_p (s)	h_s (m)
[10] Salauddin & Pearson (2019)		0.100	0.060	0.050	1.13	0.110
(1V:2H)		0.100	0.075	0.050	1.13	0.113
		0.100	0.100	0.050	1.13	0.134
[9] Sutherland et al. (2006)	26	0.190	0.199	0.013	1.87	0.270
(1V:2H)	27	0.192	0.199	0.013	3.24	0.308
	28	0.194	0.199	0.013	1.55	0.274
	34	0.200	0.126	0.013	3.24	0.179
[8] Steetzel (1993)	T1, H298-I	1.500	0.816	0.027	5.40	1.500
(1V:1.8H)	T2, H298-I	1.500	0.816	0.027	5.40	1.500
[7] Van der Meer & Pilarczyk (1988)	1:7 scale	0.860	1.238	0.033	6.40	2.000
(1V:2H)	1:35 scale	0.170	0.247	0.033	2.90	0.380
[6] Steetzel (1985)	T2, M2501-II	0.253	0.121	0.027	3.10	0.239
(1V:1.8H)	T3, M2501-II	0.253	0.119	0.027	3.40	0.302

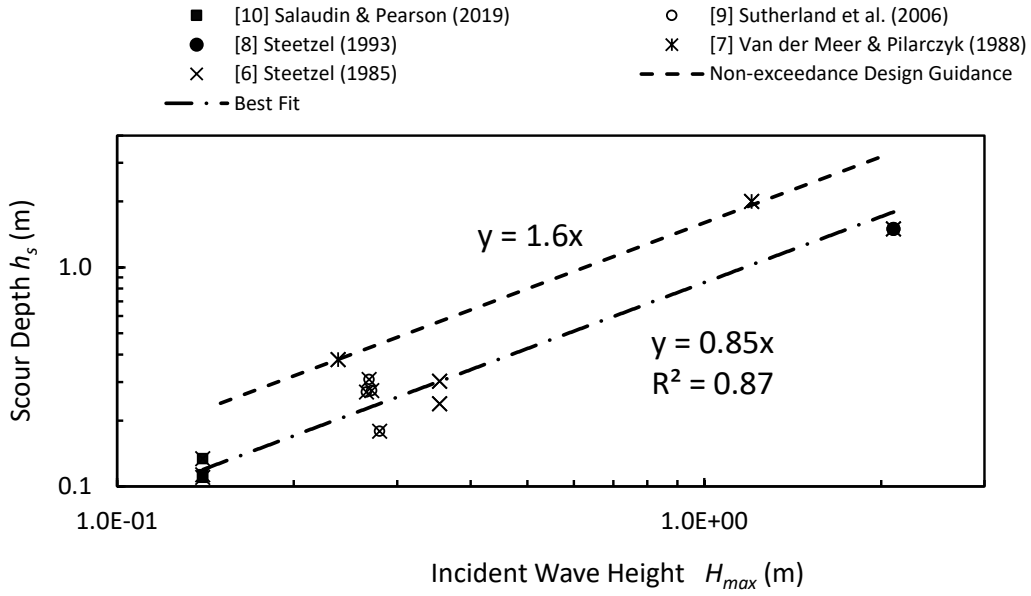

Figure 3: Scale model research results for toe scour depth versus maximum wave height at the toe for sloping revetments (1V:1.8 – 2.0H)

1.3 Requisite Armour Mass

Concept design formulae for revetment rock armor define the median requisite armor mass as a function of wave height, rock density, water density, and revetment slope following the passage of a number of waves. The formulae are in the form:

$$M_{50} = \frac{\rho_a H_s^3}{K_D \Delta^3 cot\alpha^n} \quad (3)$$

where M_{50} is the median requisite stable armor mass (kg), ρ_a is the armor density (kg/m^3), H_s is the incident significant wave height (m), Δ is the relative submerged density of the armor to water ($(\rho_a - \rho_w)/\rho_w$), α is the revetment armor slope and K_D is a damage coefficient derived empirically.[11] Subsequent developments of this formula have included additional factors in the calibration coefficient for the extent of damage,[12,13] the number of waves and the porosity of the revetment core,[14,15,16] and wave period giving formulae variations for plunging and surging wave fronts.[16] For a two-layered rock armor on an impermeable core revetment, these formulae are compared in *Table 2* where D is damage (%), $S = D/1.25$ (-),[16] N is the number of waves (-),[16] ξ_m surf similarity parameter based on mean wave period (-).[16] The formulae are compared also for "no damage" ($S = 2$, $D = 2.5\%$) in *Figure 4*.

Table 2: Damage coefficients recommended by various researchers for application to the Hudson equation for standard rock armor placed pell-mell[11]

Researcher Reference	n; K_D	Remarks
[15] Van Gent (2004)	1; 1	1000 waves
[12,13] Gordon (1972)	$1;\ 1.2D^{0.51}$	2000 Plunging breakers
[16] Van der Meer (1988)	$0;\ 79\left(\frac{S}{\sqrt{N}}\right)^{0.6}\varepsilon_m^{-1.5}$	N Plunging breakers
[16] Van der Meer (1988)	$1.5;\ 2.2\left(\frac{S}{\sqrt{N}}\right)^{0.6}\varepsilon_m^{0.3}$	N Surging breakers
[14,15] Van Gent *et al.* (2003)	$1;\ 5.4\left(\frac{S}{\sqrt{N}}\right)^{0.6}$	N All breaker types

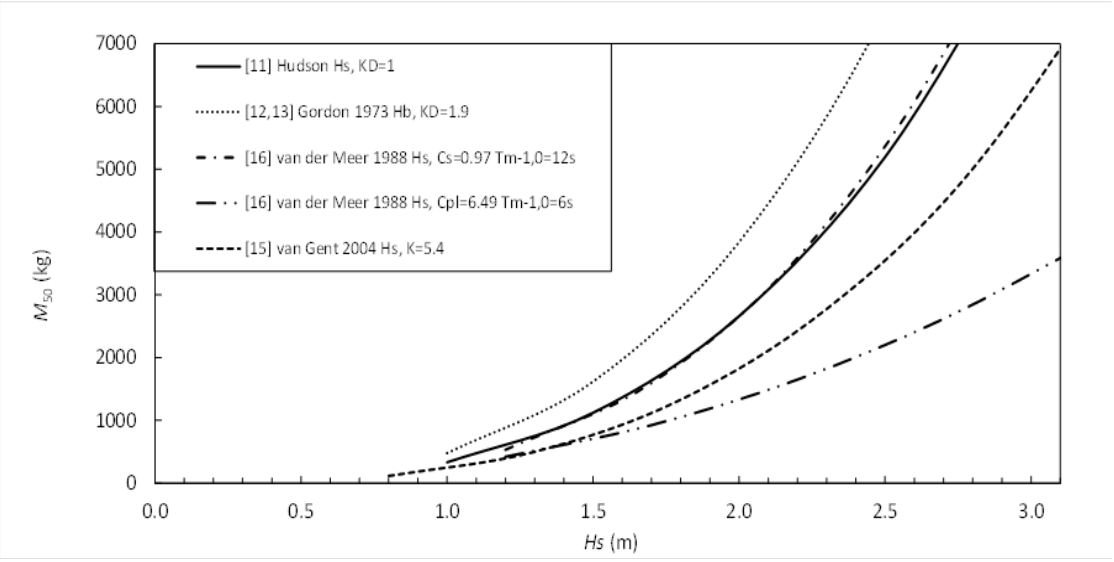

Figure 4: Current practice concept design formulae for sizing rock armor mass for no damage of a typical two-layered standard rock armored coastal revetment, impermeable core, $N = 1000$, $cot\alpha = 2$, $\Delta = 1.65$

1.4 Wave Overtopping

For various seawall and revetment configurations, the EurOtop 2018 Overtopping Manual[17] presents current practice for the relationships between measured discharges, q (m³/s/m), normalized by the factor $\left(gH_{m0}^{3}\right)^{0.5}$ and the freeboards, R_c (m), normalized by the factor H_{mo}.[18] For mild rubble-mound structures, current practice uses Equation (4) for mean overtopping discharge:[17](Eqn5.10 p115):

$$\frac{q}{\sqrt{g\ .\ H_{si}^{3}}} = \frac{a}{\sqrt{tan\alpha}}\gamma_b.\xi_{m-1,0}\exp\left[-\left(b\frac{R_c}{\xi_{m-1,0}.H_{si}\ .\gamma_b.\gamma_f\ .\gamma_\beta\ .\gamma^*}\right)^{1.3}\right] \quad (4)$$

where a = 0.023, b = 2.7, $\varepsilon_{m-1,0}$is the surf similarity parameter tan$\alpha/(H_{si}/L_o)^{0.5}$ (-), with α being the revetment slope, and γ_b, γ_f, γ_β and γ^* are influence factors that account for revetment berms, armor slope roughness, angle of wave incidence and a range of geometrical factors (respectively). Guidance for their quantification is given in the EurOtop 2018 Overtopping Manual.[17]

II. METHOD AND MATERIALS

2.1 Thesis

The energy of breaking waves is dissipated in various ways including the sound of and shudder from wave breaking producing sea spray,[18] seabed scour,[5,8] rocking and moving of revetment armor,[19] wave runup and overtopping, gravity and infragravity wave reflection.[18]

Incident wave energy, E, is a function of the product of wave height squared and wavelength thus:[20](p2-26, Eqn.2-38)

$$E = \frac{\rho_w g H_{si}^{2} L_{toe}}{8} \quad (5)$$

where ρ_w is the unit mass of seawater (kg/m³), g is gravitational acceleration (m/s²), H_{si} is the incident significant wave height (m), L_{toe} is the nearshore wavelength (m). In shallow water, the nearshore wavelength can be approximated by:[2],[20](p2-25Eqn.2-37)

$$L_{toe} = T_p\sqrt{gh_{toe}} \quad (6)$$

where h_{toe} is the nearshore depth at the revetment toe (m).

In the following, data from comprehensive scale model studies of rock armored coastal revetments are used to derive concept design formulae for seabed scour, stable rock armor mass and overtopping discharge by normalizing laboratory data with factors based on wave energy, rather than using current practice with factors based on wave height alone.

2.2 Scour

Equation (7) is a concept design formula for revetment toe scour, based on wave energy, which has been calibrated empirically with results from several moveable bed model studies covering a large range of scales (Table 1, *Figure 5):*

$$h_s = 0.8\left(H_{si}^{2}T_p\sqrt{gh_{toe}}\right)^{\frac{1}{3}} \quad (7)$$

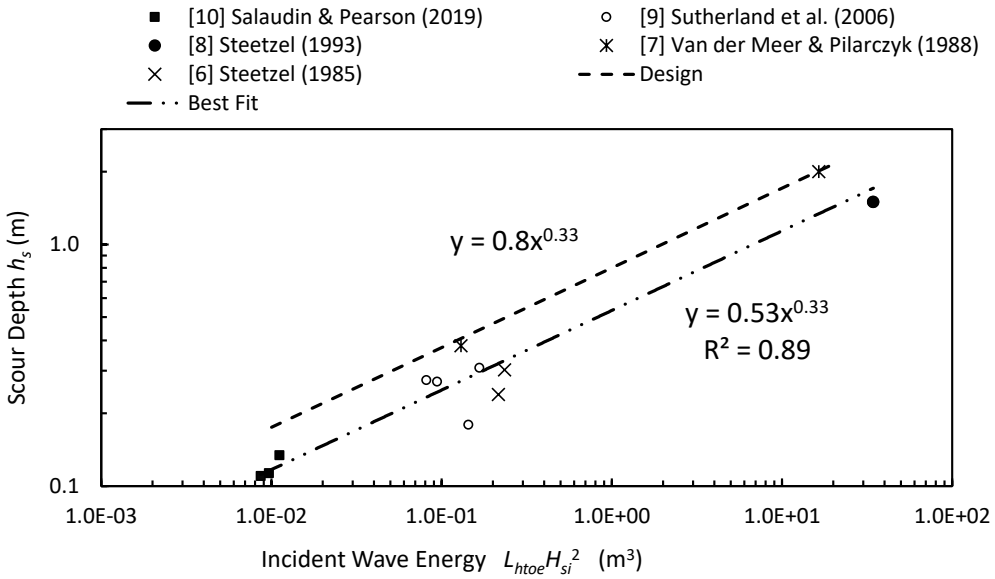

Figure 5: Scale model calibration of a toe scour formula for the design of 1V:2H sloping rock armored revetment

2.3 Armour Mass

It is the energy in breaking waves, that is, the breaking velocity of the fluid mass, that applies the disturbing forces of lift and drag to revetment armor that may cause it to rock and shift, and for rock armor placed pell-mell it is the mass of that armor under the restoring force of gravity that secures or otherwise its stability.[19] The wave energy method for rock armor stability was calibrated empirically with results from flume studies on rock-armored impermeable mounds under a range of random wave conditions *(Table 3, Figure 6)*.

Table 3: Range of test conditions for data in Figure 6

Data Source	D_{n50} (m)	H_s/h_{toe} (g)	T (s)	Damage (%)	m (-)	cotα (-)	ξ_b (-)	Breaker type
[21] Thomson and Shuttler (1975)	0.016 – 0.032	0.07 - 0.16	Ts: 1.0 – 1.3	15	0.000	2,3,4,6	1.2 - 3.0	Plunging & surging
[16] van der Meer (1988)	0.036, 0.210	0.06 – 0.32	Tm: 1.3 – 3.3	1 - 40	0.033	2,3,4,6	0.5 – 5.3	Plunging & surging
[14] van Gent et al. (2003)	0.026	0.42-0.59	Tp: 1.2 – 3.0	2 - 30	0.033	2,4	0.4 – 1.0	Spilling & Plunging

For the wave energy method under the breaking wave conditions in Table 3, the best fit relationship between armor mass M_{50} (kg), level of damage D (-), number of waves N (-), revetment slope tanα (-), relative density $\Delta = (\rho_a/\rho_w - 1)$ (-) where ρ_a is armor mass (kg/m³), and wave energy is given in Equation (8):

$$M_{50} = \frac{\rho_a H_{si}^2 T_p \sqrt{g h_{toe}}}{370\left(\frac{D}{\sqrt{N}}\right)^{0.28} \Delta^3 cot\alpha^{1.5}} \quad (8)$$

with Equation (9), being a 95% non-exceedance relationship, recommended for concept design:

$$M_{50} = \frac{\rho_a H_{si}^2 T_p \sqrt{g h_{toe}}}{310\left(\frac{D}{\sqrt{N}}\right)^{0.33} \Delta^3 cot\alpha^{1.5}} \quad (9)$$

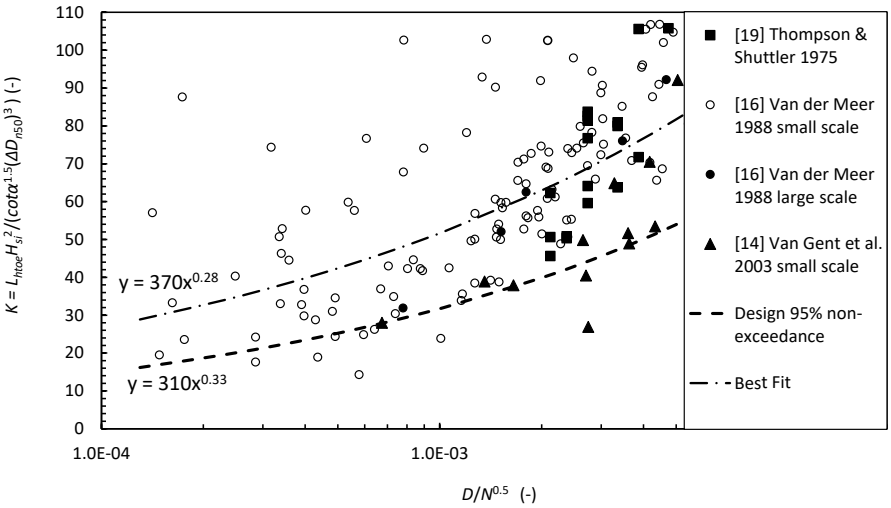

Figure 6: Wave energy damage coefficient versus damage by a number of waves for double layered standard rough angular rock armored revetments placed pell-mell over impermeable underlayers

2.4 Wave Overtopping

Scale model wave overtopping data comprised results from a comprehensive set of flume experiments undertaken at the US Army Engineer Waterways Experiment Station's Coastal Engineering Research Centre (CERC) to investigate the amelioration of flooding at Roughans Point Massachusetts.[22] The data was sourced from a 16:1 (prototype:model) scale model of a rock armored revetment *(Figure 7)* conducted in a 1 m by 1 m by 45 m long wave flume.

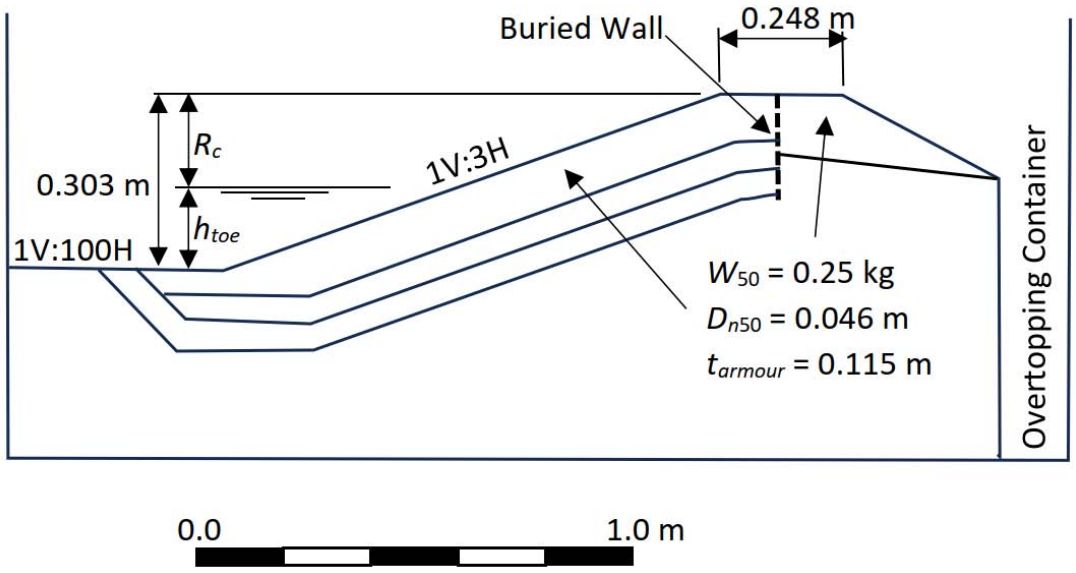

Figure 7: Revetment model schema[22]

A wide range of wave conditions was represented in these tests, with the incident significant wave heights measured at the revetment toe. During a single test run, irregular waves were generated continuously for 33 minutes, each test comprising some 1,000 waves. The wave paddle was programmed to produce a modified Joint North Sea Wave Program (JONSWAP) wave spectrum for the water depth at the wave generation blade, with waves shoaling and breaking on the seabed and spilling onto the revetment.[22] Overtopping rates were determined by measuring the change in water level in the overtopping container behind the model during a test run using point gauges.

The overall influence factor, Υ, providing for the rock armor slope roughness, porosity and specific geometric properties of the revetment, was assessed by calibrating Υ to Equation (4). The calibration achieved the best fit result with $\Upsilon = 0.35$.[18]

Equation (4) was modified for wave energy normalizing factors in Equation (11):

$$\frac{q}{\left(gLH_{m0}^2\right)^{0.5}} = \frac{a}{(tan\alpha)^{0.5}} exp\left[-\left(b\frac{R_c}{\gamma\left(LH_{m0}^2\right)^{0.33}}\right)^{1.3}\right] \quad (11)$$

The model data allowed for further calibration of the remaining factors a and b to wave period. For the wave energy factored equation, this was undertaken for each wave period dataset by varying a and b to optimise scatter and accuracy, which allowed derivation of relationships for the factors a and b to the modelled wave periods.[18] This allowed the derivation of Equation (12), which incorporates wave period at prototype scale, the values for a and b having been determined at model scale $(R_c + h_{toe})/0.303$:1 (prototype:model) according to Froude scaling.[18]

$$\frac{q}{\left(gLH_s^2\right)^{0.5}} = \frac{0.0000594\left(\frac{0.55T_p}{\sqrt{R_c+h_{toe}}}\right)^{7.40}}{(tan\alpha)^{0.5}} exp\left[-\left(1.29\left(\frac{0.55T_p}{\sqrt{R_c+h_{toe}}}\right)^{1.26}\frac{R_c}{\gamma\left(gLH_s^2\right)^{0.33}}\right)^{1.3}\right] \quad (12)$$

III. DISCUSSION

3.1 Toe Scour

The scale model data do not support current practice, being the "rule-of-thumb" that the toe scour depth is the maximum wave height that can be sustained in the water depth *(Figure 8)*. Large and small scale (1:7, 1:35) modelling undertaken at Delft Hydraulics has indicated that the maximum scour depth can exceed the maximum sustainable wave height by a factor of around 1.6,[5,7] which is shown to have occurred at a relative toe depth $h_{toe}/L_o \approx 0.02$, as predicted.[23] Hence, Equation (7) is recommended for concept design for revetment toe scour.

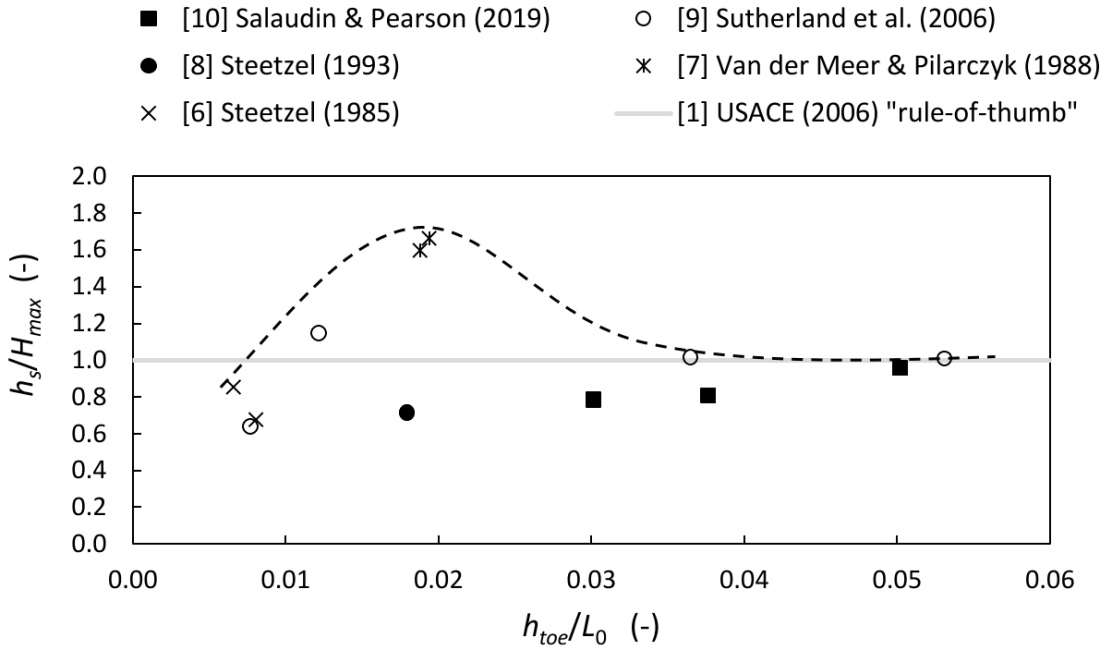

Figure 8: Ratio of maximum measured scour depth to maximum wave height *versus* relative toe depth for physical scale modelled sloping revetments (Table 1)

3.2 Armour Mass

The proposed wave energy formula for requisite rock armor mass, Equation (9), is compared with commonly used rock armor sizing formulae in *Figure 9*.[11-13,15,16] For a wide range of wave periods, it

compares well with the equations of van der Meer[16] up to a significant wave height of around 2.5 m, beyond which it gives smaller mass for longer periods and larger mass for shorter periods. The formula cannot be compared meaningfully with those of Hudson,[11] Gordon[12,13] or van Gent[15] as those formulae do not include wave period.

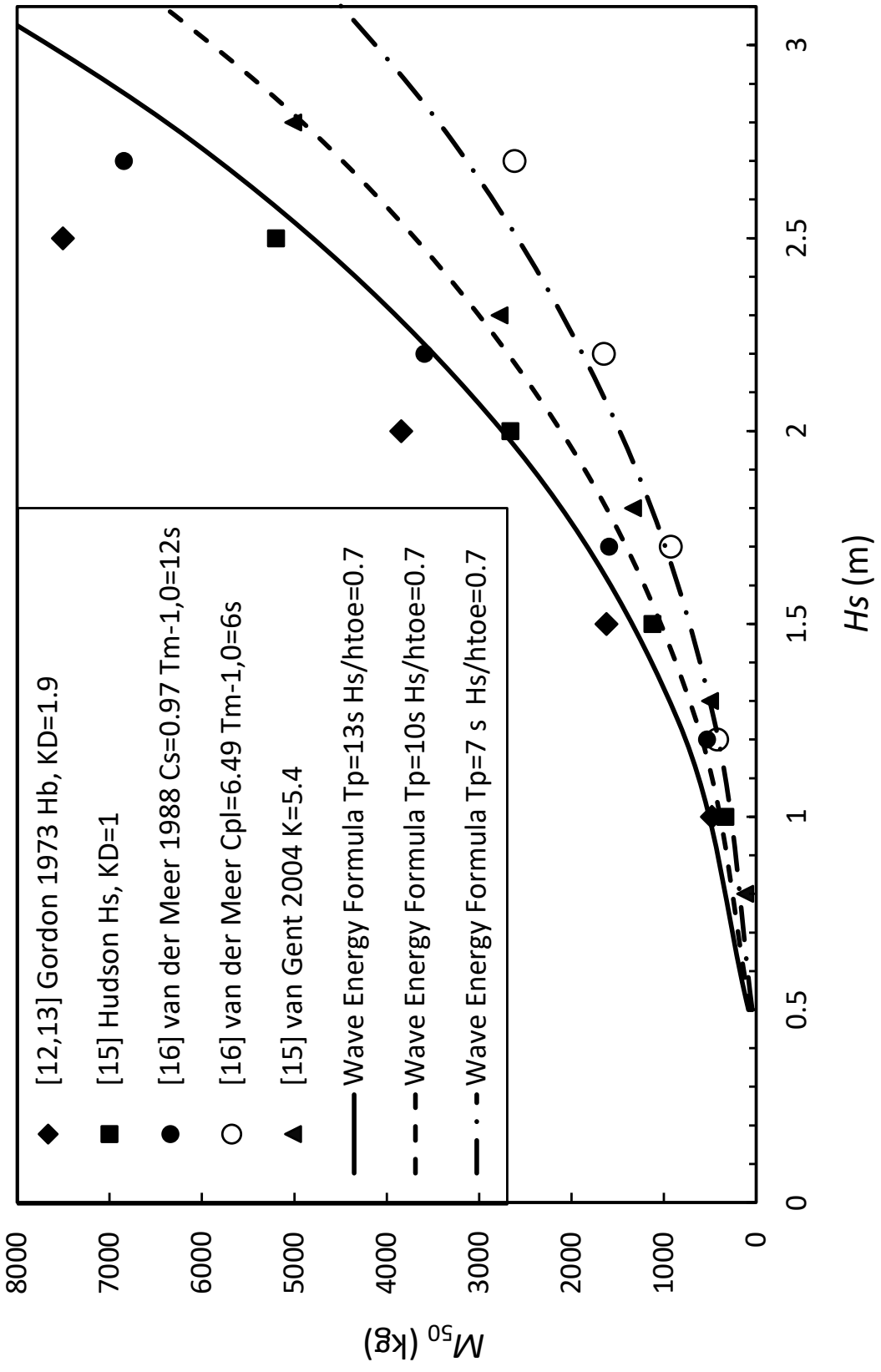

Figure 9: Comparison of commonly used rock armor sizing formulae[11-13,15,16] with the proposed wave energy formula for $S = 2$, $D = 2.5\%$. Assumed: $T_m = 0.9T_p$,[16] $N = 1000$; $m \approx 0.04$; $H_s = 0.7h_{toe}$.

The coherence of the flume data normalised with wave height alone and with wave energy is compared in *Figure 10*. The data normalised with wave height gives K_D values over a spread of two orders of

magnitude, whereas that normalised with wave energy has a spread of one order of magnitude. This is reflected in the Coefficient of Determination, which is higher for the data normalised with wave energy.

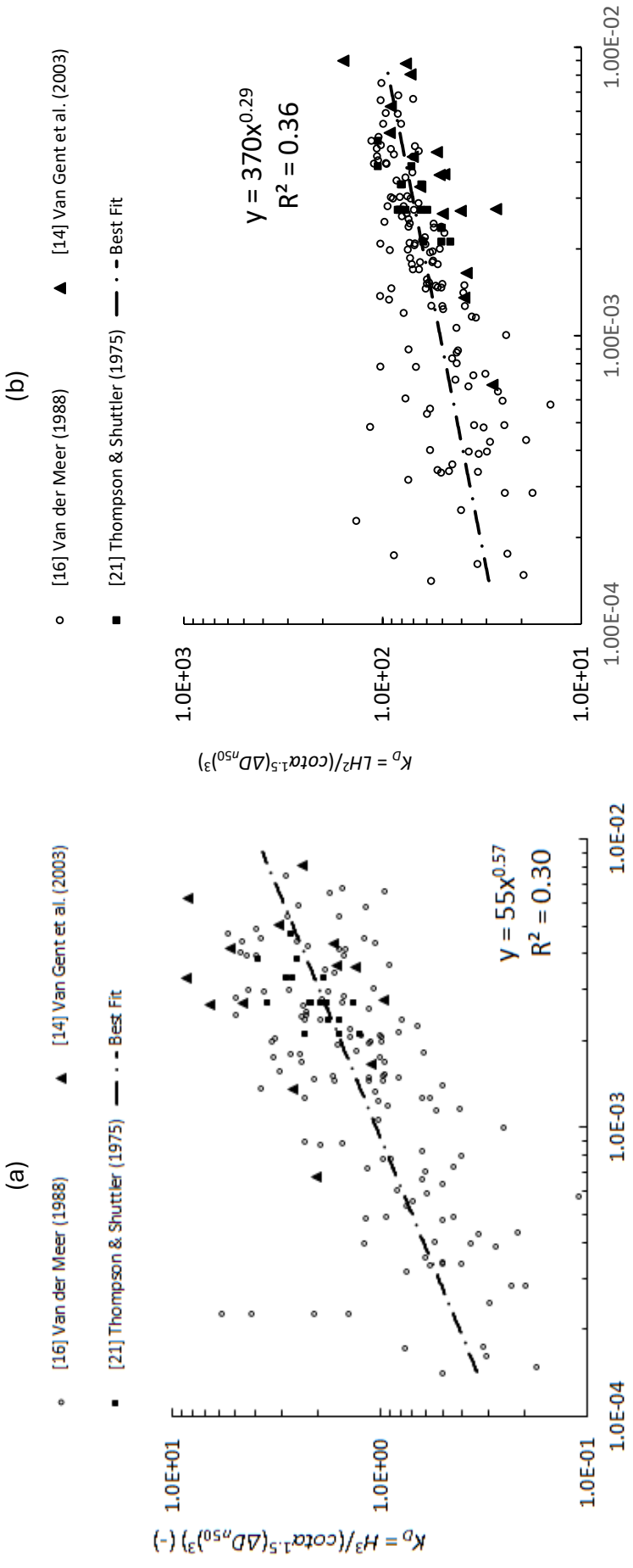

Figure 10: Coherence of flume data normalised with (a) wave height and (b) wave energy

3.3 Overtopping Discharge

The revetment model data *versus* the prediction equations normalised with wave height factors and wave energy factors are compared in *Figure 11(a)* and *Figure 11(b)* respectively. The prediction equation based on data normalised with wave energy factors is more coherent, with a coefficient of determination of 0.87 compared with 0.76 for the prediction equation based on data normalised with wave height alone.[18] Further, however, the data based on wave energy normalization show a clear trend with wave period, which is not unexpected and which is not apparent with the data normalised using wave height alone.

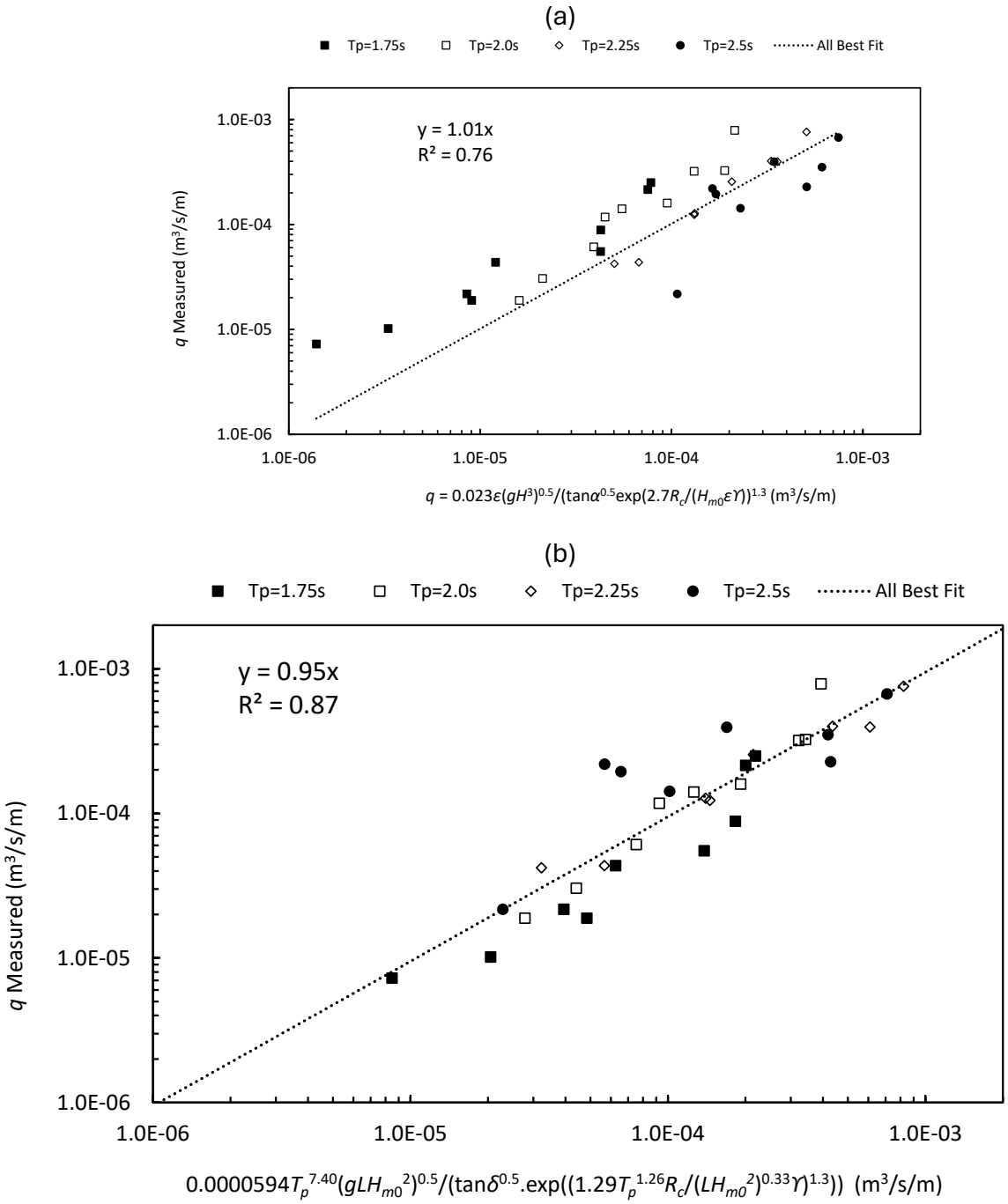

Figure 11: Revetment model data for measured versus predicted discharges with calibrated equations normalised with (a) wave height factors and (b) wave energy factors including calibration to wave period,[18] with $\tan\delta = \tan\alpha_{sf}$[17 p118-119]

The predictions using the equation based on wave energy normalization including wave period are more accurate than those using the equation developed from wave height normalization *(Figure 12)*.[18]

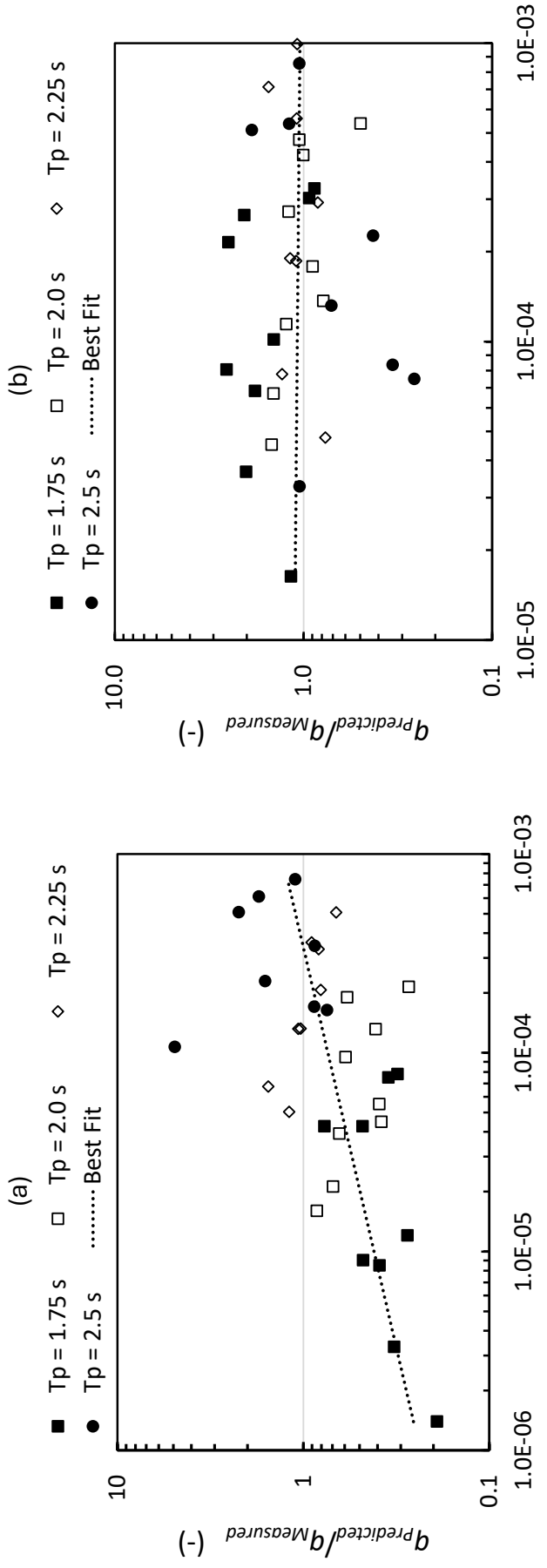

Figure 12: Comparison of predictions with measured revetment model data for (a) the current practice equation normalised with wave height factors and (b) the proposed equation normalised with wave energy factors and calibrated to wave period

3.4 Design Methodology

Results from physical scale modelling may not represent prototype behavior correctly because of experimental model effects and/or scale effects.[18] Depending on the scale applied for concept design, prototype conditions could lay beyond some of the limits of the modelling parameters used for concept design formulae. Extrapolating model results should consider experimental constraints including:

- The fronting seabed slope affects wave shoaling and breaking. Seabed slopes of the scour tests varied widely from m = 0.013 – 0.05. However, for armor mass only one bed slope, m = 0.033, was modelled, as was the case for overtopping with m = 0.01.
- Revetment slopes varied little for scour with cotα = 1.8 – 2.0, for armor mass cotα = 2,3,4,6 but for overtopping considered herein cotα = 3.0.
- Model wave periods varied from 1 s to 3 s. This would limit a 9:1 Froude scale model to schematise prototype wave periods from 3 s to 9 s [18]. For a smaller scale model of 50:1, say, the prototype periods schematised by the modelling would range from 7s to 21 s [18]. Scaling up to prototype dimensions using equations developed from scale modelling may include test results that have schematised unrealistic prototype wave periods.[18]
- Much of the data used to develop concept design formulae is based on around 1,000 zero-crossing waves. Revetments in depth-limited situations are likely to be subjected to a much larger number of waves, in which case average overtopping discharges and requisite armor mass may be underestimated.[18,19]
- Results of two-dimensional flume studies do not replicate any three-dimensional processes that occur in the nearshore surf zone fronting revetments.[5,18,19]

Site-specific scale modelling is recommended for the detailed design of coastal revetments. Apart from experimental constraints, Reynolds number scale effects are possible.[18,19] The drag coefficient for spheres increases for Re < 2×10^3 but decreases for Re > 2×10^5.[24] Should that apply to rock armor, then if the model data are applied at normal scales for prototype concept design, for the likely prototype ranges of Reynolds number the drag force coefficient of the flow on rock armor would be relatively lower in the prototype than that in the model, leading to conservative estimates for requisite armor mass,[19],[21](p6) but non-conservative estimates for runup and overtopping.[18]

IV. CONCLUSIONS

Formulae for the concept design of coastal revetments located in shallow water have been presented that relate toe scour, the requisite stable mass of armor rock and overtopping discharges to the energy of the incident breaking waves. These formulae include parameters for significant wave height, wave period, toe depth, degree of armor damage, the number of waves, revetment slope, armor and water densities, and revetment crest freeboard. The formulae have been calibrated using flume data generated by research at university and government hydraulic laboratories in the UK, USA and the Netherlands. The formulae are compared with current practice and show more coherence with the available flume data. Scale effects have been considered, with requisite armor mass likely to be over-estimated and average overtopping under-estimated. This research would benefit from more laboratory data, which is recommended particularly to investigate the impacts of seabed slope, wave period and Reynolds number scale effects.

Funding: This research has been self-funded by the author.

*Data Availability Statement: A*ll data, models and code generated or used during the study appear in the submitted article and are available as referenced.

Conflicts of Interest: The author declares no conflicts of interest. The author was employed by the company Worley Consulting. The author declares that the research was conducted in the absence of any commercial or financial relationships that could be construed as a potential conflict of interest.

REFERENCES

1. USACE. Coastal Engineering Manual, Coastal Engineering Research Centre, Waterways Experiment Station, US Army Corps of Engineers, EM 1110-2-1100. 2006. 6 volumes.
2. Battjes, J.A. Surf similarity. Proceedings 14th Int. Conf. on Coastal Engg., 1974, vol. 1, pp. 466–480, DOI:10.9753/icce.v14.26.
3. Goda, Y. Random Seas and Design of Maritime Structures. World Scientific, Singapore, 2000, 443pp.
4. Coastal Wiki. Available online: https://www.coastalwiki.org/wiki/Shallow-water_wave_theory Figure 27 (accessed on 7-10-2025).
5. Nielsen, A.F. Design scour levels for dune revetments and seawalls. ASCE J. Waterway, Port, Coastal, Ocean Eng., 2023, 149(3): 04023005, 8pp, DOI: 10.1061/JWPED5.WWENG-1963.
6. Steetzel, H.J. Systematic Research into the Functioning of Dune Toe Structures - Model Study into Scour near the Dune Revetment Toe (in Dutch). Delft Hydraulics Technical Report, 1985,135pp.
7. Van der Meer, J.W., Pilarczyk, K.W. Large verification tests on rock slope stability, Coastal Engineering 1988, Chapter 157, 13pp.
8. Steetzel, H.J. Cross-shore Transport during Storm Surges. Thesis Tech. Univ. Delft, Published also as Delft Hydraulics Communication No. 476, September 1993, 294pp.
9. Sutherland, J, Obhrai, C., Whitehouse, R.J.S., Pearce A.M.C. Laboratory tests of scour at a seawall, Proc. 3rd Int. Conf. on Scour and Erosion. Amsterdam, CUR Bouwn & Infra, 2006, 19pp.
10. Salauddin, M., Pearson, J.M. Experimental study on toe scouring at sloping walls with gravel foreshores, J. Mar. Sci. Eng., 7,198, 2019; DOI:103390/jmse7070198, 12pp.
11. Hudson, R.Y. Design of Quarry-Stone / Cover Layers for Rubble-Mound Breakwaters - Hydraulic Laboratory Investigation, U.S. Army Engineer Waterways Experiment Station, Corps of Engineers, Vicksburg, Mississippi, Research Report No. 2-2 July 1958, 68pp.
12. Gordon, A.D. Stability of breakwaters under the action of breaking waves, MEngSc thesis, UNSW, 1973, 60pp.
13. Foster, D.N., Gordon, A.D. Stability of armor units against breaking waves. Proc. 1st Aust. Conference on Coastal Engineering, Sydney, Australia, 1973, 98-107.
14. Van Gent, M.R.A., Smale, A.J., Kuiper, C. Stability of Rock Slopes with Shallow Foreshores, ASCE, Proc. Coastal Structures, Portland, January 2003, DOI:10.1061/40733(147)9
15. Van Gent, M.R.A. On the stability of rock slopes, Keynote, NATO-workshop, May 2004, Bulgaria, 20pp.
16. Van der Meer, J.W. Rock Slopes and Gravel Beaches Under Wave Attack. Ph.D. Thesis, Delft University of Technology, Delft, The Netherlands, 1988. Delft Hydraulics Communication No. 396, 214pp.
17. EurOtop 2018. Manual on wave overtopping of sea defences and related structures. An overtopping manual largely based on European research, but for worldwide application. Van der Meer, J.W., Allsop, N.W.H., Bruce, T., De Rouck, J., Kortenhaus, A., Pullen, T., Schüttrumpf, H., Troch, P., Zanuttigh, B. 2018, www.overtopping-manual.com.
18. Nielsen, A.F. Wave energy considerations for predicting average overtopping discharges of depth limited waves breaking onto rock-armoured coastal revetments. Taylor and Francis, Australasian Journal of Water Resources, 2025, DOI:10.1080/13241583.2025.2599522.
19. Nielsen A.F., Gordon A.D. Revetment rock armour stability under depth-limited breaking waves. MDPI, Coasts 5(2), 12, 2025, https://DOI.org/10.3390/coasts5020012

20. USACE. Shore Protection Manual. Coastal Engineering Research Centre, Waterways Experiment Station, US Army Corps of Engineers, 1984, 2 volumes.
21. Thompson, D.M., Shuttler, R.M. Riprap design for wind-wave attack – A laboratory study in random waves. Hydraulics Research Station Wallingford Report EX 707, September 1975, 129pp.
22. Ahrens, J.P., Heimbaugh, M.S., Davidson, D.D. Irregular Wave Overtopping of Seawall/Revetment Configurations Roughans Point Massachusetts, Coastal Engineering Research Center, Department of the Army, Waterways Experiment Station, Corps of Engineers Report CERC-86-7, September 1986, 64pp.
23. Sutherland, J., Obhrai, C., Whitehouse, R.J.S. Understanding the lowering of beaches in front of coastal defence structures, Phase 2. Improved predictors for wave-induced scour at seawalls. Technical Note TN CBS0726/09. Contractor: HR Wallingford Ltd., Client UK Department for Environment, Food and Rural Affairs (Defra), 2006, Available from http://science-search.defra.gov.uk, (Accessed 6 May 2022), 39pp.
24. Yager, R.J. Calculating drag coefficients for spheres and other shapes using C++. Report ARL-TN-612, US Army Research Laboratory, Aberdeen Proving Ground, MD 21005-5066, June 2014.

This page is intentionally left blank

Prony Analysis -A Case Study in Eastern Regional Power System in India

Lakshmi Gayatri Chintalapati & Yesuratnam Guduri

University college of engineering

ABSTRACT

The stability of the Indian power grid is frequently challenged by Low-Frequency Oscillations (LFOs), particularly in the hydro-dominant Eastern Region, where evacuation corridors are constrained. This paper presents a detailed analysis of a cascade tripping event that occurred on July 7, 2017, involving the 400 kV Teesta-III to Rangpo corridor. Utilizing high-resolution synchro phasor data obtained from Phasor Measurement Units (PMUs), this study characterizes the oscillatory behavior of the grid during the disturbance. While conventional Fast Fourier Transform (FFT) methods are often employed for spectral monitoring, this work employs Prony Analysis due to its superior capability in analyzing non-stationary, transient signals and its ability to directly extract modal damping ratios. The analysis identifies the dominant inter-area and local modes, quantifying their energy, damping percentage, and frequency content. The results demonstrate that specific modes exhibited insufficient damping during the event, contributing to system separation.

Keywords: WAMS, PMU, Prony analysis, Linear state estimation, Synchrophasor technology, Low-frequency oscillations, Small-signal stability.

Classification: LCC Code: TK3091

Language: English

Great Britain Journals Press

LJP Copyright ID: 392963
Print ISSN: 2631-8474
Online ISSN: 2631-8482

London Journal of Engineering Research

Volume 25 | Issue 6 | Compilation 1.0

Prony Analysis -A Case Study in Eastern Regional Power System in India

Lakshmi Gayatri Chintalapati[α] & Yesuratnam Guduri[σ]

ABSTRACT

The stability of the Indian power grid is frequently challenged by Low-Frequency Oscillations (LFOs), particularly in the hydro-dominant Eastern Region, where evacuation corridors are constrained. This paper presents a detailed analysis of a cascade tripping event that occurred on July 7, 2017, involving the 400 kV Teesta-III to Rangpo corridor. Utilizing high-resolution synchro phasor data obtained from Phasor Measurement Units (PMUs), this study characterizes the oscillatory behavior of the grid during the disturbance. While conventional Fast Fourier Transform (FFT) methods are often employed for spectral monitoring, this work employs Prony Analysis due to its superior capability in analyzing non-stationary, transient signals and its ability to directly extract modal damping ratios. The analysis identifies the dominant inter-area and local modes, quantifying their energy, damping percentage, and frequency content. The results demonstrate that specific modes exhibited insufficient damping during the event, contributing to system separation. These findings are subsequently used to derive necessary control parameters for the design of robust Power System Stabilizers (PSS) and oscillation damping filters, aimed at enhancing the dynamic stability of the Eastern Regional Grid.

Keywords: WAMS, PMU, prony analysis, linear state estimation, synchrophasor technology, low-frequency oscillations, small-signal stability.

Author α: Master of Engineering (Power systems) Dept. of Electrical Engineering University college of engineering, Osmania University, Hyderabad, India.
σ: Senior Professor Dept. of Electrical Engineering University college of engineering, Osmania University, Hyderabad, India.

I. INTRODUCTION

Day by day, the power system is becoming increasingly complex due to the growing demand for electricity and the widespread integration of power electronic devices. As a result, the power grid is undergoing continuous and rapid changes. These developments introduce several operational challenges and contingencies, making timely monitoring of system data crucial for identifying faults and preventing major economic losses [1–3].

Traditionally, utilities have relied on Remote Terminal Units (RTUs) in Supervisory Control and Data Acquisition (SCADA) systems, which provide system information to operators every 4 to 10 seconds. However, this steady-state data is no longer sufficient for effective monitoring, control, and operation of large interconnected grids [4,5]. To overcome these limitations, a more advanced technology—synchronized measurement technology—has been introduced, and systems based on this concept are known as Wide Area Measurement Systems (WAMS). The key device in synchronized measurement technology is the Phasor Measurement Unit (PMU). A PMU is generally defined as a device that measures the magnitude, phase angle, frequency, and rate of change of frequency of electrical quantities in real time. These measurements are synchronized with GPS signals. The overall process from data collection to WAMS applications is shown in Fig. 1 [6]. At the substation, the PMU

London Journal of Engineering Research

receives both analog and digital inputs, filters them using an anti-aliasing filter, converts analog data into digital form, and performs phasor estimation. The phasor data is then transmitted through a modem. IEEE Standard C37.118-2011 specifies the measurement requirements, communication message formats, and protection classes for PMU data. The GPS-synchronized PMU data is transmitted to a Phasor Data Concentrator (PDC) through various communication channels. The PDC collects, sorts, and time-aligns the data based on timestamps and measurement types. Using communication networks, this processed data is then forwarded to SCADA or WAMS control centres. Finally, the data supports a wide range of WAMS applications, including real-time monitoring, control, protection, and post-event (historian) analysis [6].

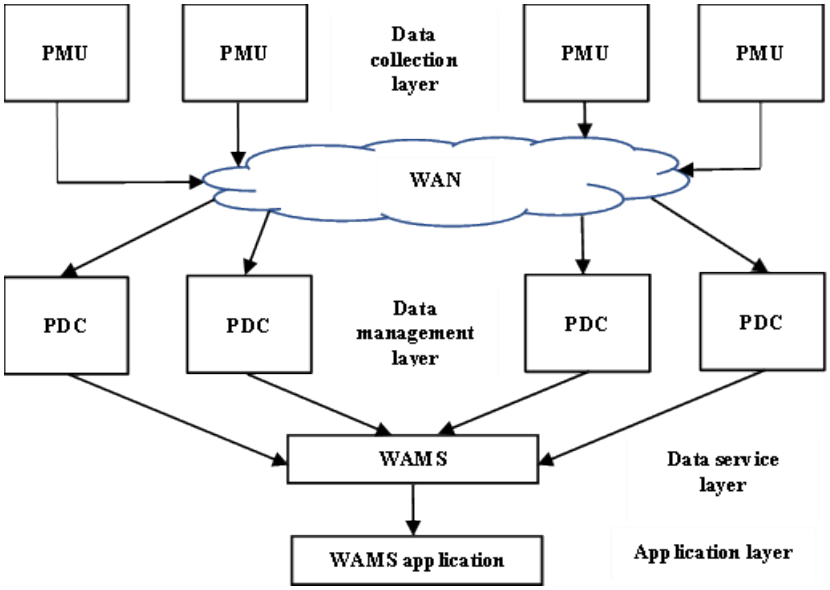

In this paper, Section 2 describes the TEESTA-III case study, Prony analysis, and its implementation in MATLAB. Section 3 presents the results obtained from the Prony analysis, and Section 4 provides the conclusions drawn from the analyses performed.

II. PRONY ANALYSIS

The Prony method was introduced by Gaspard de Prony, a French engineer, mathematician, and scientist. Prony analysis is an extension of the Fast Fourier Transform (FFT), and it fits a linear combination of damped exponential terms to a uniformly sampled signal. The general linear exponential function is defined as given in equation (1) [9–13].

The estimation of low-frequency inter-area oscillations is challenging when using a conventional SCADA system, as its measurements are derived from RTUs. RTUs cannot provide synchronized phasor measurements of voltage, current, and system frequency at multiple locations with the same time stamp. Therefore, for transient and dynamic analysis, the required data must be obtained from Phasor Measurement Units (PMUs), which provide time-synchronized measurements essential for accurate oscillation analysis.

$$X(t) = \sum_{i=1}^{P} A_i \, e^{\alpha i t} \cos(\omega_i t + \theta_i) \quad (1)$$

Where i=1 to P (number of damping exponential modes), $A_i$is the amplitude, $\alpha_i$is the damping factor, $\omega_i$is the frequency, and θ_i is the phase angle. Prony analysis gives a complete analysis of the given signal by providing amplitude, phase, frequency, and damping coefficients of the signal, whereas Fourier analysis does not provide the damping coefficients.

After applying Euler's formula and after approximations, the above formula is deduced to the following function,

$$X(t) = \sum_{i=1}^{P} \frac{1}{2} A_i \left(e^{j\Theta_i} e^{\lambda^+ t} + e^{-j\Theta_i} e^{\lambda^- t} \right) \tag{2}$$

Where, $\lambda = \sigma_i \pm j\omega_i$, are the eigen values of the system

The above equation can also be written as follows

$$X(t) = \sum_{i=1}^{P} B_i \, e^{\lambda i t} \tag{3}$$

Let the above is sampled at intervals of time period 'T', then the above equation for X(t) can expressed as,

$$X(t) = \sum_{i=1}^{P} B_i \, e^{\lambda i t} \tag{4}$$

$$X(t) = \sum_{i=1}^{P} B_i \, e^{\lambda i k T} = \sum_{i=1}^{P} B_i \, \mu_i{}^k \tag{5}$$

Where, k = 0,1, 2,..... N-1; N= total number of samples

From the above equations it is clear that if we find out the values of B and μ we can get the values of A and α, which will decide the presence of oscillations. The following method is used in Prony analysis to find the values of B and μ.

$$\begin{bmatrix} X(0) \\ X(1) \\ \vdots \\ X(N-1) \end{bmatrix} = \begin{bmatrix} 1 & 1 & \dots & 1 \\ \mu_1 & \mu_2 & \dots & \mu_m \\ \vdots & \vdots & & \vdots \\ \mu_1{}^{N-1} & \mu_2{}^{N-1} & \dots & \mu_m{}^{N-1} \end{bmatrix} \begin{bmatrix} B_1 \\ B_2 \\ \vdots \\ B_m \end{bmatrix} \tag{6}$$

In generalized form the above matrix can be written as follows,

$$[X] = [U][b] \tag{7}$$

The M values of μ, can be considered as a solution of the following polynomial with $\alpha_i$as unknown coefficients,

$$\mu^m - a_1 \mu^{m-1} - a_1 \mu^{m-2} \dots \dots \dots \dots \dots - a_m = 0 \tag{8}$$

the 'a' can be represented in the vector form as follows,

$$\hat{a} = [-a_m \; -a_{m-1} \dots \dots \dots \dots \dots - a_1 \; 1 \; 0 \dots .0] \tag{9}$$

on multiplying the (6) and (9) equations we get

$$\hat{a}X = X(m) - [-a_m X(0) - a_{m-1} X(1) \dots \dots - a_1 \, X(m-1)] = \hat{a}[U][b] \tag{10}$$

$$= B_1[\mu_1{}^m - (a_1 \mu^{m-1} - a_m \mu_1{}^{m-1} + \cdots . + a_m \mu_1{}^0)] + B_2[\dots .] + \cdots . = 0 \tag{11}$$

The initial time instant is assumed, then the above equation is written as,

$$\begin{bmatrix} X(m) \\ X(m+1) \\ \vdots \\ X(N-1) \end{bmatrix} = \begin{bmatrix} X(m+1) & \dots & X(0) \\ X(m) & \dots & X(1) \\ \vdots & & \vdots \\ X(N-2) & \cdots & X(N-m-1) \end{bmatrix} \begin{bmatrix} a_1 \\ a_2 \\ \vdots \\ a_m \end{bmatrix} \quad (12)$$

The above matrix can be written as,

$$[d] = [D][a] \quad (13)$$

Assume $N > 2m$, the coefficient vector 'a' is calculated as,

$$[a] = [D^{'}][d] \quad (14)$$

$D^{'}$ is pseudo inverse of d

After we find vector 'a', the μ can be easily found out and finally we can find out B, and after that we can easily get the amplitude 'A' and damping factor 'α'. Prony analysis can be performed on various discrete signals of power, voltage, current, and frequency. In this project, the frequencies are taken into consideration and we can perform modal analysis. Prony analysis is basically a measurement-based analysis, which does not require any network model of the system. Using the real-time data obtained from the eastern region of the Indian power system, Prony analysis has been performed and the respective frequency components, damping, and amplitudes are found. This analysis helps in finding out the dominant low-frequency components in the system; there by, we can estimate the low-frequency oscillations in the system [9–13].The theoretical superiority of Prony analysis for this study lies in its resolution and damping extraction capabilities. FFT suffers from spectral leakage when analysing short, transient data windows and cannot distinguish between two closely spaced modes if the record length is insufficient. Prony analysis, being a parametric technique, is not limited by the uncertainty principle of the Fourier transform, allowing it to resolve low-frequency inter-area modes (0.1–0.8 Hz) even from short post-fault data records. Furthermore, the ability to directly quantify negative or low damping provides actionable data for the tuning of Power System Stabilizers (PSS), which FFT magnitude plots cannot provide.

2.1 Case Study in Eastern Region of India – TEESTA-III Event Description

On 07th of July 2017, at 10:26:00 hrs, a 400 kV Rangpo–Binaguri (RB)-II line tripped due to a line-to-ground fault in phase-B, which caused congestion in the 400 kV RB-I line. This is mitigated by the System Protection Scheme (SPS)-I at Teesta-III by tripping generating units at Chujachen (at 0.84 s), JLHEP, and Dikchu (both at 1.70 s) power stations. However, the RB-I line remained congested and caused the tripping of the 400 kV Teesta-III–Rangpo (at 2.50 s) single-circuit line (loss of 400 MW load). This is followed by the tripping of remaining units at Teesta-III and Dikchu (at 3.00 s) due to loss of evacuation path.

The PMU data of this event is collected from 12 PMUs at different locations in the eastern region of India, as shown in Figure 3, to perform the Prony analysis. The different locations are Bihar, Binaguri, Durgapur, Farakka, Jeypore, Patna, Ranchi, Rourkela, Sasaram, Talcher, Relangi, and Jamshedpur.

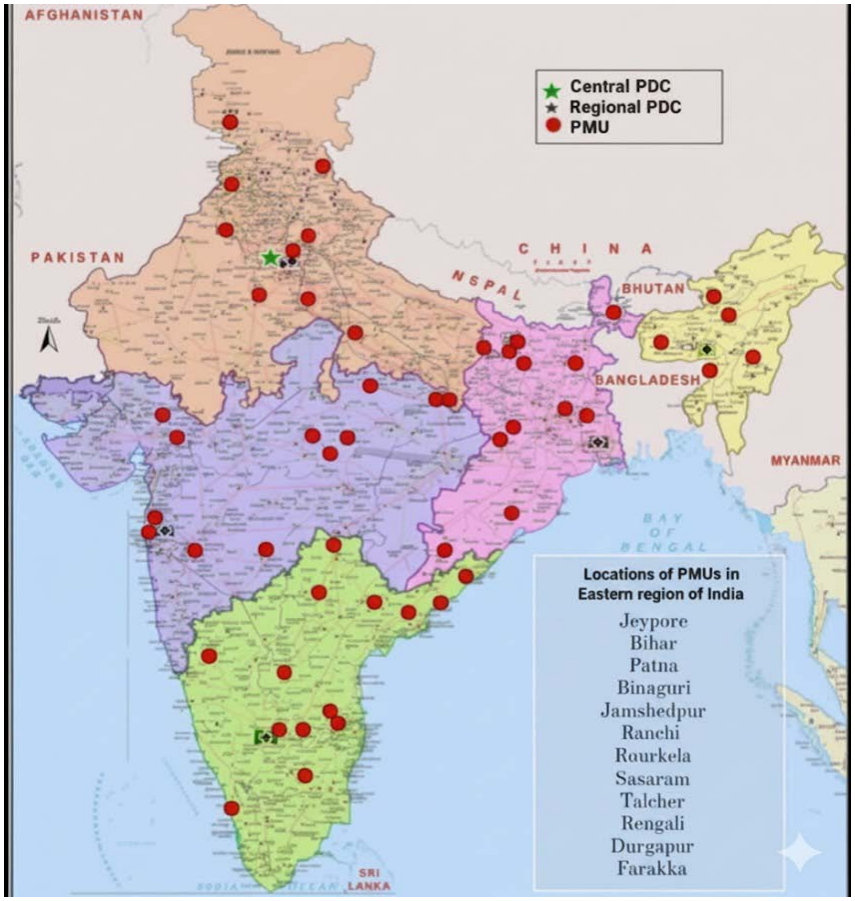

Fig. 2: Locations of PMUs in India During the TEESTA-III Event on 07th July 2017

2.2 Prony Analysis on TEESTA-III Data

The real-time historian data has been provided by the Eastern Region Power Grid, and it has been obtained from PMUs at 12 different locations, namely Bihar, Binaguri, Durgapur, Farakka, Jeypore, Patna, Ranchi, Rourkela, Sasaram, Talcher, Relangi, and Jamshedpur, along with the time stamps. In Prony analysis, the actual frequency variation with time is first plotted. The obtained signal is then detrended, as detrending improves the accuracy of the analysis. After detrending, the Prony fit for each signal is obtained, and the Prony-approximated linear curves for different locations are shown in Figures (3–14).

The sampling frequency of the obtained data from the Eastern Region Power Grid is 25 Hz. Hence, for satisfactory Prony analysis, the model order (M) must be at least half of the number of samples (N), i.e., 12.5. Therefore, the model order is chosen as 13 in this case [10].

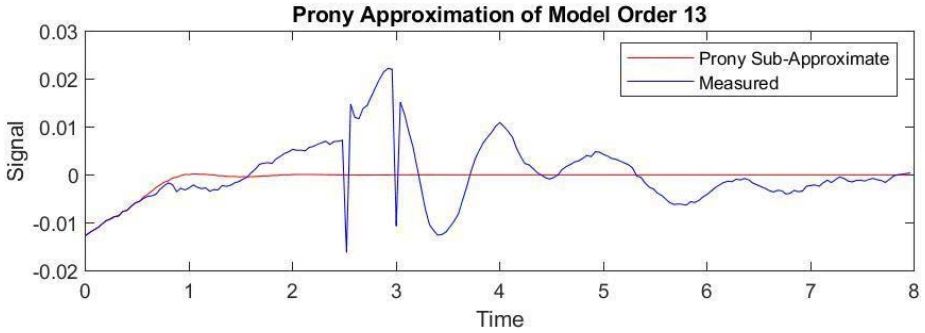

Fig. 3: Frequency Variation after Detrending and Prony Fit at Bihar

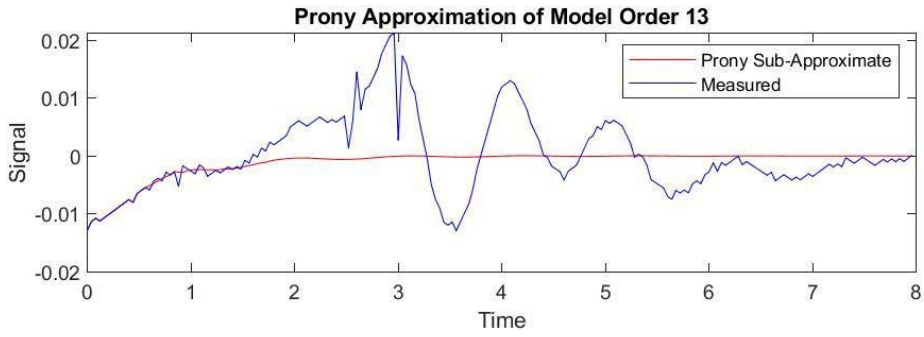

Fig. 4: Frequency Variation after Detrending and Prony Fit at Durgapur

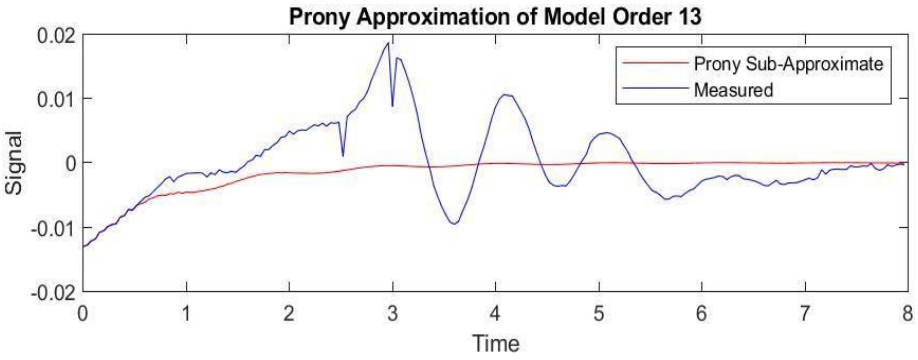

Fig. 5: Frequency Variation after Detrending and Prony Fit at Farakka

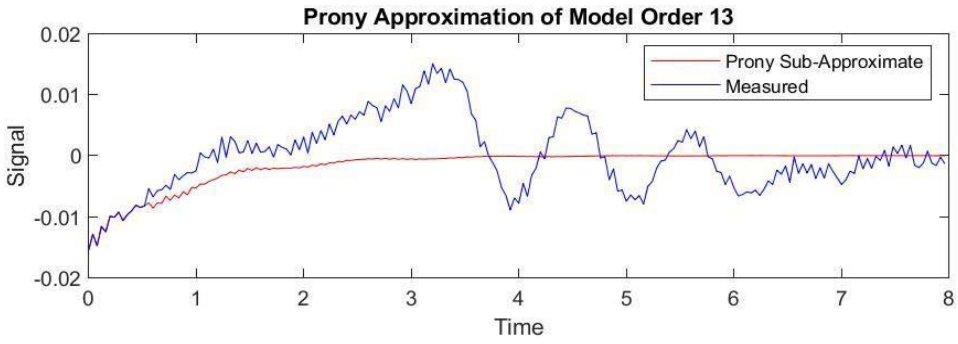

Fig. 6: Frequency Variation after Detrending and Prony Fit at Jeypore

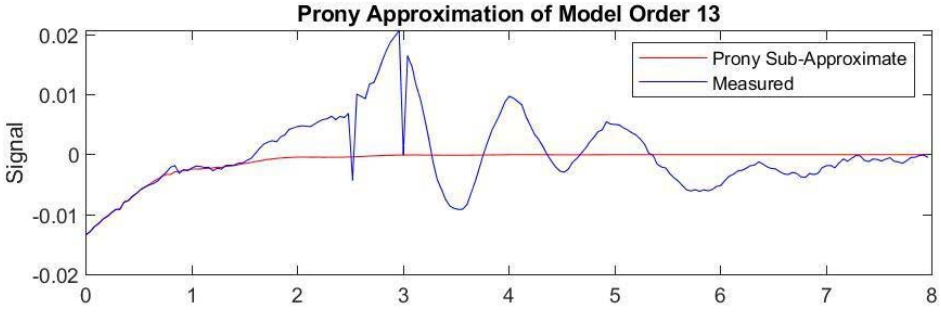

Fig. 7: Frequency Variation after Detrending and Prony fit at Patna

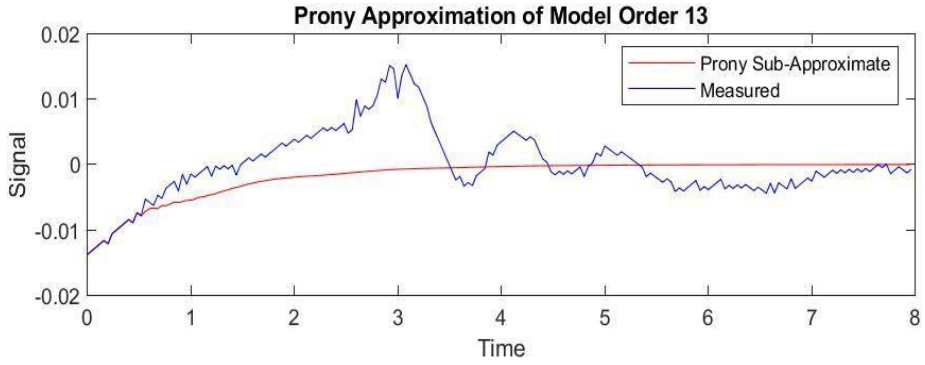

Fig. 8: Frequency Variation after Detrending and Prony Fit at Ranchi

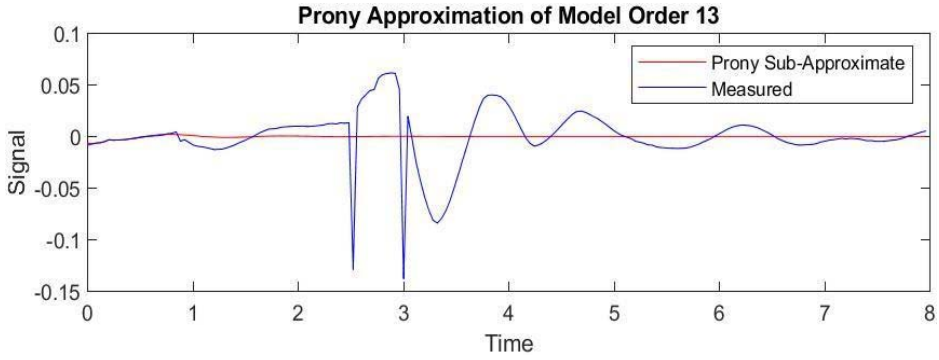

Fig. 9: Frequency Variation and Prony Fit at Binaguri

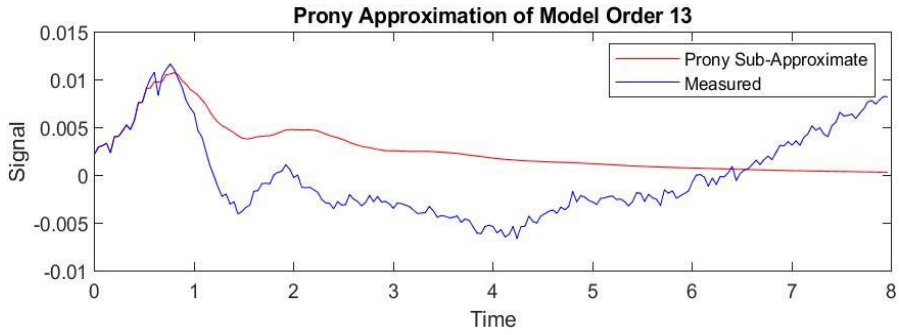

Fig. 10: Frequency Variation after Detrending and Prony Fit at Rourkela

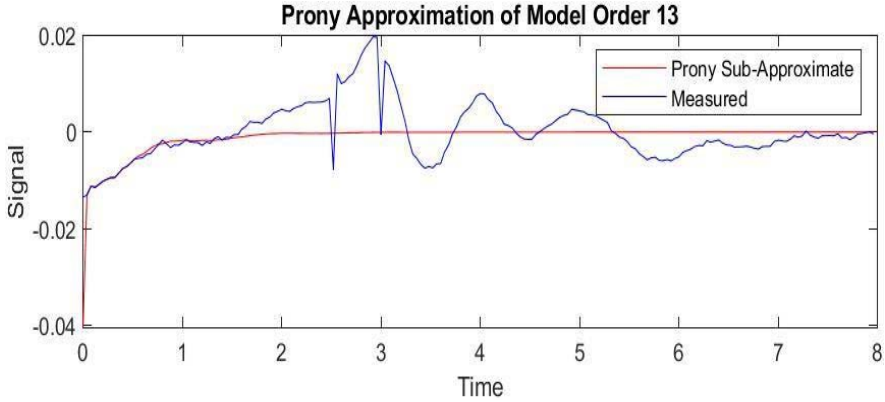

Fig. 11: Frequency variation after detrending and Prony fit at Sasaram

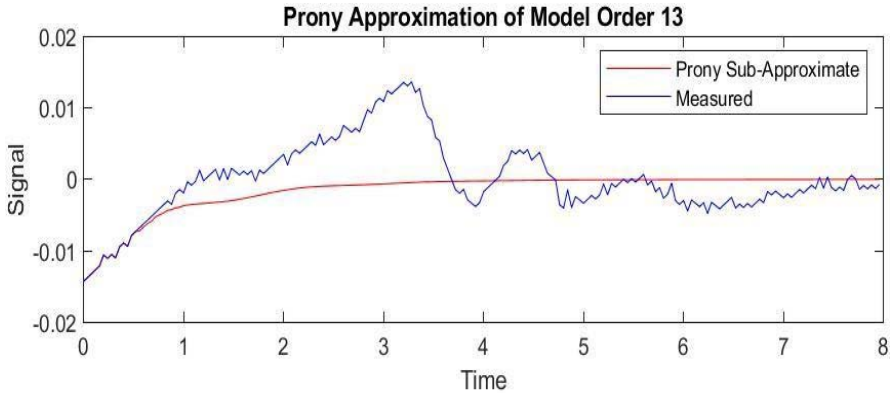

Fig. 12: Frequency variation after detrending and Prony fit at Talcher

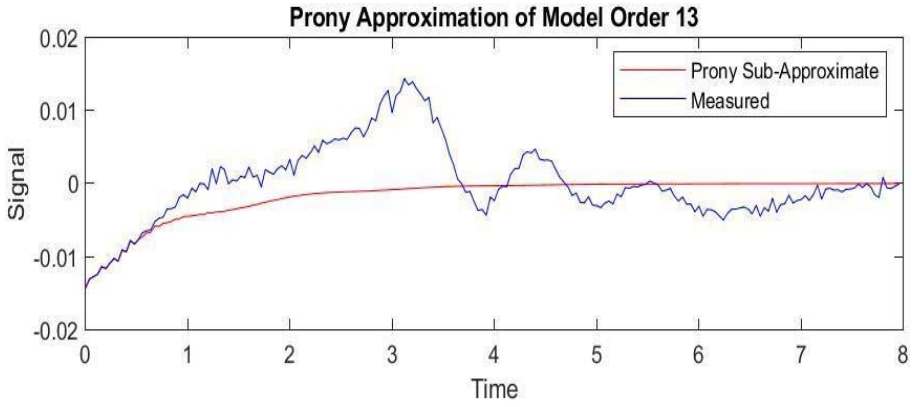

Fig. 13: Frequency Variation after Detrending and Prony Fit at Rengali

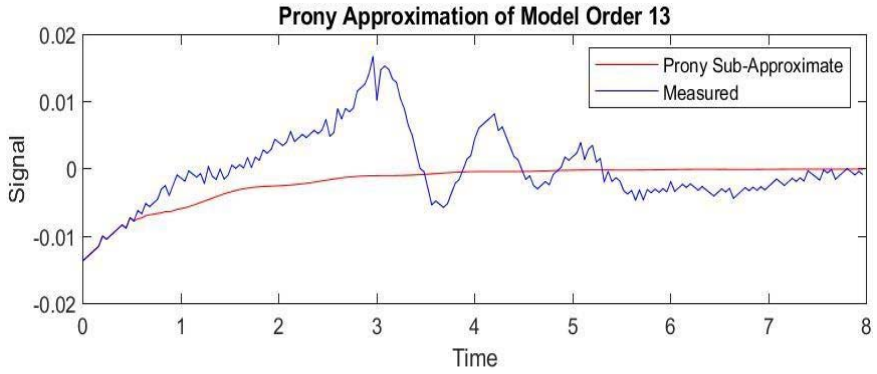

Fig. 14: Frequency Variation after Detrending and Prony Fit at Jamshedpur

III. RESULTS

3.1 Prony Analysis on Eastern Region of India

Prony analysis is performed on the Indian Eastern Grid data, and the respective frequency components present at different locations are tabulated. The mean squared error (MSE) between the original signal and the Prony fit is also calculated and presented in the figures.

Table 1: Prony Analysis of Frequency Variation at Bihar

Mode	Amplitude(Hz)	Damping(%)	Frequency(Hz)	Energy(J)
1	3.9e-02	3.4	0.031	1.6e-03
2	5.3e-03	1.9	0.9	5.0e-05
3	5.3e-03	1.9	0.9	5.0e-05

4	2.6e-04	1.4	10	1.6e-09
5	2.6e-04	1.4	10	1.6e-09
6	1.6e-04	1.5	8.3	5.7e-09
7	1.6e-04	1.5	8.3	5.7e-09
8	1.5e-04	1.9	3.9	4.0e-09
9	1.5e-04	1.9	3.9	4.0e-08
10	0.92e-04	1.4	12	2.0e-09
11	1.7e-05	1.7	6.2	5.8e-10
12	1.7e-05	1.7	6.2	5.8e-10

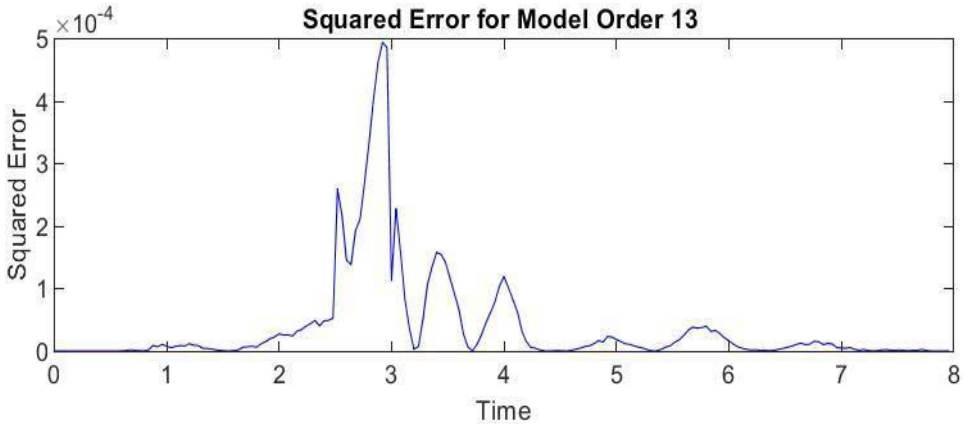

Fig. 15: Mean squared error of Prony analysis at Bihar

Table 1 shows the respective modes of frequencies, damping, energies, and their corresponding amplitudes at Bihar. Generally, frequencies between 0–2 Hz can be considered as electromechanical oscillations. From the results, it can be seen that the oscillations with frequencies 0.0031 Hz and 0.9 Hz are treated as low-frequency oscillations, and their damping is less than 10%; therefore, they may cause small-signal instability. As Prony analysis cannot differentiate noise signals, those with energy greater than 10^{-5} are considered spurious signals. Figure 15 shows the mean squared error between the original signal and the Prony approximation at Bihar.

Table. 2: Prony Analysis of Frequency Variation at Binaguri

Mode	Amplitude(Hz)	Damping(%)	Frequency(Hz)	Energy(J)
1	1.1e-02	1.1	1.8	5.1e-03
2	1.1e-02	1.1	1.81	5.1e-05
3	5.5e-03	1.3	0.92	7.8e-05
4	5.5e-03	1.3	0.92	7.8e-05
5	4.4e-04	2.2	4.1	3.0e-07
6	4.4e-04	2.2	4.1	3.0e-07
7	3.3e-04	1.6	6.3	2.2e-09
8	3.3e-04	1.6	6.31	2.2e-09
9	2.6e-04	1.5	8.4	1.5e-08
10	2.6e-04	1.5	8.4	1.5e-09
11	1.9e-04	1.3	10	9.2e-08
12	1.9e-04	1.3	10	9.2e-08

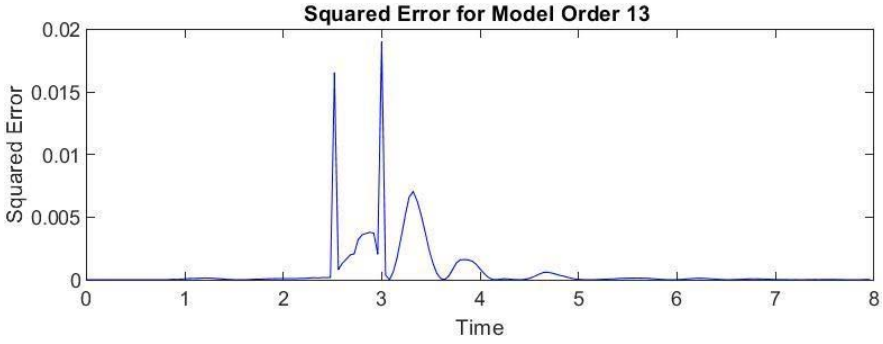

Fig. 16: Mean Squared Error of Prony Analysis at Binaguri

Table 2 shows the respective modes, frequencies, damping, energies, and their corresponding amplitudes at Binaguri. From the results, it can be seen that the oscillations with frequencies 1.8, 1.81, and 0.92 Hz are treated as low-frequency oscillations. Their energy is below the threshold, and their damping is less than 10%, so they may cause small-signal instability. As Prony analysis cannot differentiate noise signals, signals with energy greater than 10^{-5} are considered spurious. Figure 16 shows the mean squared error between the original signal and the Prony approximation at Binaguri.

Table 3: Prony analysis of frequency variation at Durgapur

Mode	Amplitude (Hz)	Damping (%)	Frequency(Hz)	Energy(J)
1	2.4e-02	0.97	0.03	1.9e-03
2	9.6e-04	0.45	0.9	6.4e-05
3	9.6e-04	1.45	0.9	6.4e-05
4	3.9e-04	1.7	10	3.0e-07
5	3.9e-04	1.7	10	3.0e-07
6	2.7e-04	1.6	12	1.5e-07
7	2.4e-04	1.9	4	1.0e-07
8	2.4e-04	1.9	4	1.0e-07
9	1.4e-04	1.9	6.2	3.7e-08
10	1.4e-04	1.9	6.2	3.8e-08
11	9.4e-05	1.7	8.3	1.8e-08
12	9.4e-05	1.7	8.3	1.8e-08

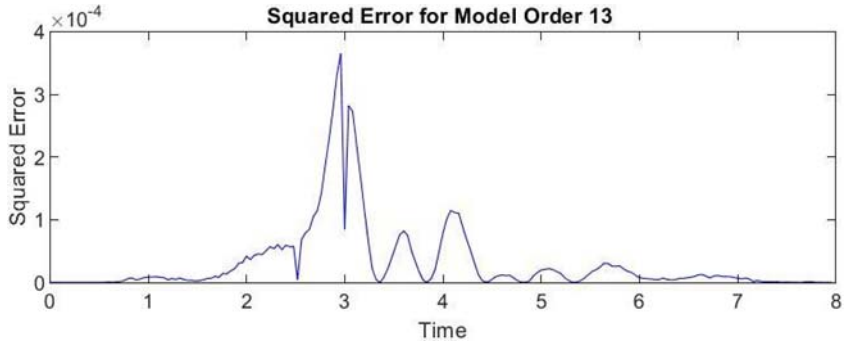

Fig. 17: Mean squared error of Prony analysis at Durgapur

Table 3 shows the respective modes, frequencies, damping, energies, and their corresponding amplitudes at Durgapur. From the results, it can be seen that the oscillations with frequencies 0.03 and 0.9 Hz are treated as low-frequency oscillations. Their energy is below the threshold, and their damping is less than 10%, so they may cause small-signal instability. As Prony analysis cannot differentiate noise signals, the signals with energy greater than 10^{-5} are considered spurious. Figure 17 shows the mean squared error between the original signal and the Prony approximation at Durgapur.

Table. 4: Prony Analysis of Frequency Variation at Farakka

Mode	Amplitude(Hz)	Damping(%)	Frequency(Hz)	Energy(J)
1	2.4e-02	1.4	0.03	1.4e-03
2	1.3e-02	39	12	4.5e-05
3	1.2e-02	18	12	4.6e-05
4	1.2e-03	6.4	0.89	7.7e-05
5	1.2e-03	6.4	0.89	7.7e-05
6	8.8e-04	3.2	11	8.6e-07
7	8.8e-04	3.2	11	8.6e-07
8	5.0e-04	2.0	3.9	4.3e-07
9	5.0e-04	2.0	3.9	4.3e-07
10	4.4e-04	1.9	6.2	3.6e-07
11	4.5e-04	1.9	6.2	3.6e-07
12	4.4e-04	2.0	8.6	3.3e-07
13	4.4e-04	2.0	8.6	3.3e-07

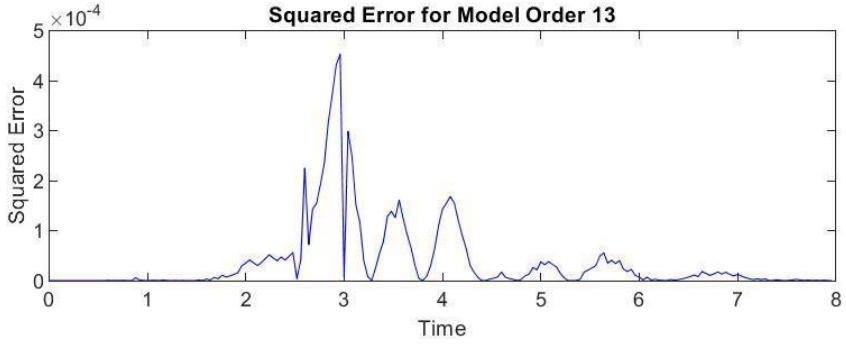

Fig. 18: Mean Squared Error of Prony Analysis at Farakka

Table 4 shows the respective modes, frequencies, damping, energies, and their corresponding amplitudes at Farakka. From the results, it can be seen that the oscillations with frequencies 0.03 and 0.89 Hz are treated as low-frequency oscillations, which decay very slowly, and their energy is below the threshold. Their damping is also less than 10%, so they may cause small-signal instability. The 12 Hz component is likely noise, as it is damped out very fast with damping values of 39% and 18%. As Prony analysis cannot differentiate noise signals, signals with energy greater than 10^{-5} are considered spurious. Figure 18 shows the mean squared error between the original signal and the Prony approximation at Farakka.

Table 5: Prony Analysis of Frequency Variation at Patna

Mode	Amplitude(Hz)	Damping(%)	Frequency(Hz)	Energy(J)
1	2.6e-02	1.5	0.03	1.4e-03
2	1.3e-03	0.98	0.91	5.5e-06
3	1.3e-03	0.98	0.91	5.5e-06
4	2.6e-04	1.8	12	1.3e-07
5	2.4e-04	1.7	10	1.2e-07
6	2.4e-04	1.7	10	1.2e-07
7	1.8e-04	1.7	8.3	6.9e-08
8	1.8e-04	1.7	8.3	6.9e-08
9	1.5e-04	1.8	3.9	4.0e-08

10	1.5e-04	1.8	3.9	4.0e-08
11	1.2e-04	1.9	6.2	2.8e-08
12	1.2e-04	1.9	6.2	2.8e-08

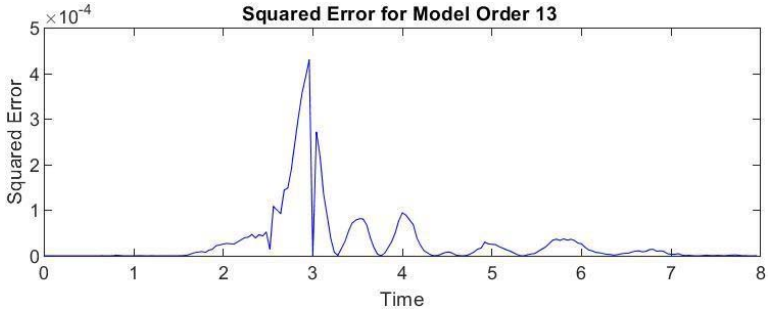

Fig. 19: Mean Squared Error of Prony Analysis at Patna

Table 5 shows the respective modes, frequencies, damping, energies, and their corresponding amplitudes at Patna. From the results, it can be seen that the oscillations with frequencies 0.03 and 0.91 Hz are treated as low-frequency oscillations. Their energy is below the threshold, and their damping is also less than 10%, so they may cause small-signal instability. As Prony analysis cannot differentiate noise signals, signals with energy greater than 10^{-5} are considered spurious. Figure 19 shows the mean squared error between the original signal and the Prony approximation at Patna.

Table. 6: Prony Analysis of Frequency Variation at Jeypore

Mode	Amplitude(Hz)	Damping(%)	Frequency(Hz)	Energy(J)
1	3.0e-02	1.2	0.03	2.6e-03
2	3.4e-03	13	6.1	4.4e-06
3	1.3e-03	0.69	0.84	8.0e-05
4	1.3e-03	0.69	0.84	8.0e-05
5	1.2e-03	2.4	3.8	2e-06
6	1.2e-03	2.4	3.8	2e-06
7	1.2e-03	2.9	6.8	1.7e-06
8	1.2e-03	2.9	6.8	1.7e-06
9	8.5e-04	0.9	12.1	2.6e-06
10	8.5e-04	0.9	12	2.6e-06
11	3.5e-04	2.4	9.3	1.8e-07
12	3.5e-04	2.4	9.3	1.8e-07

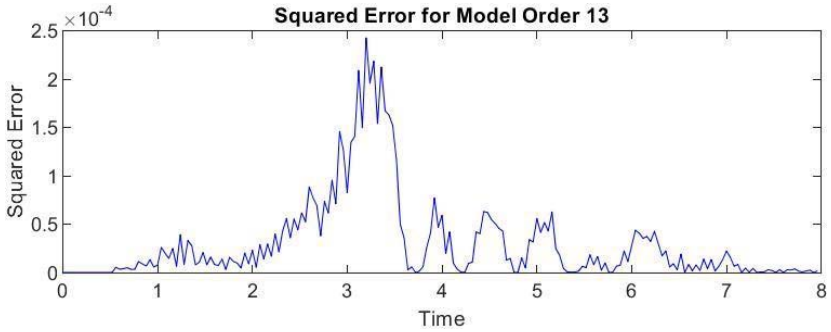

Fig. 20: Mean squared error of Prony analysis at Jeypore

Table 6 shows the respective modes, frequencies, damping, energies, and their corresponding amplitudes at Jeypore. From the results, it can be seen that the oscillations with frequencies 0.03 and 0.84 Hz are treated as low-frequency oscillations. Their energy is below the threshold, and their

damping is also less than 10%, so they may cause small-signal instability. The 6.1 Hz component is likely noise, as it is damped out very fast with a damping of 13%. As Prony analysis cannot differentiate noise signals, signals with energy greater than 10^{-5} are considered spurious. Figure 20 shows the mean squared error between the original signal and the Prony approximation at Jeypore.

Table. 7: Prony Analysis of Frequency Variation at Ranchi

Mode	Amplitude(Hz)	Damping(%)	Frequency(Hz)	Energy(J)
1	4.4e-02	22	11	5.9e-05
2	4.4e-02	22	11	5.9e-05
3	2.7e-02	0.94	0.031	2.4e-03
4	7.7e-03	6.9	12	3.5e-05
5	7.7e-03	6.9	12	3.5e-05
6	1.2e-03	2.8	8.6	1.8e-06
7	1.2e-03	2.8	8.6	1.8e-06
8	1.1e-03	1.0	8.1	3.6e-06
9	1.1e-03	1.0	8.1	3.6e-06
10	4.0e-04	2.2	3.9	2.4e-07
11	4.0e-04	2.2	3.9	2.4e-07
12	3.5e-04	3.3	6.3	1.3e-07
13	3.5e-04	3.3	6.3	1.3e-07

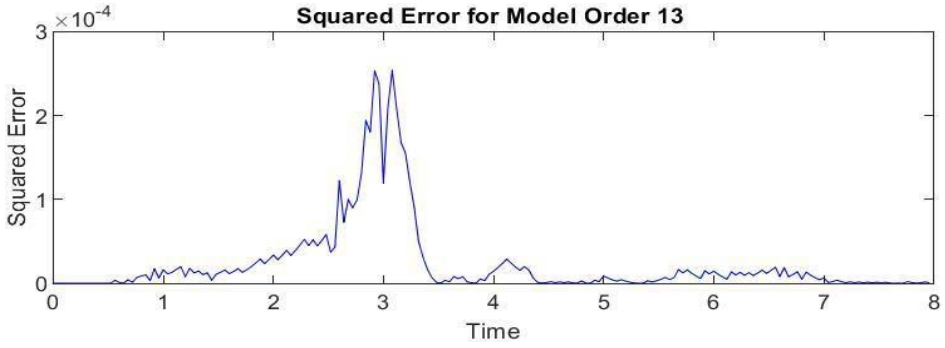

Fig. 21: Mean Squared Error of Prony Analysis at Ranchi

Table 7 shows the respective modes, frequencies, damping, energies, and their corresponding amplitudes at Ranchi. From the results, it can be seen that the oscillation with frequency 0.031 Hz is treated as a low-frequency oscillation. Its energy is below the threshold, and its damping is also less than 10%, so it may cause small-signal instability. The 11 Hz component is likely noise, as it is damped out very fast with a damping of 22%. As Prony analysis cannot differentiate noise signals, signals with energy greater than 10^{-5} are considered spurious. Figure 21 shows the mean squared error between the original signal and the Prony approximation at Ranchi.

Table 8: Prony Analysis of Frequency Variation at Rourkela

Mode	Amplitude(Hz)	Damping(%)	Frequency(Hz)	Energy(J)
1	2.1e-02	0.43	0.031	3.2e-03
2	7.7e-03	1.1	0.73	1.8e-04
3	7.7e-03	1.1	0.73	1.8e-04
4	4.6e-03	7.3	12	1.2e-06
5	4.6e-03	7.3	12	1.2e-06
6	1.5e-03	3.1	10	2.5e-06

7	1.5e-03	3.1	10	2.5e-06
8	8.8e-04	4.1	7.5	6.9e-07
9	8.8e-04	4.1	7.5	6.9e-07
10	8.0e-04	4.0	5.9	5.8e-07
11	8.0e-04	4.0	5.9	5.8e-07
12	6.8e-04	1.1	3.5	1.3e-06
13	6.8e-04	1.1	3.5	1.3e-06

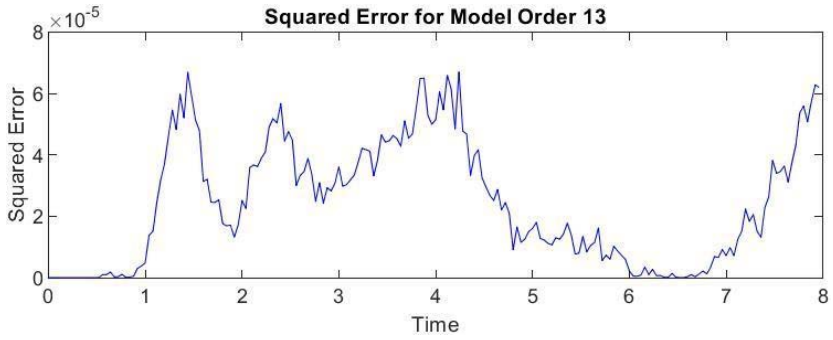

Fig. 22: Mean Squared Error of Prony Analysis at Rourkela

Table 8 shows the respective modes, frequencies, damping, energies, and their corresponding amplitudes at Rourkela. From the results, it can be seen that the oscillations with frequencies 0.03 and 0.73 Hz are treated as low-frequency oscillations. Their energy is below the threshold, and their damping is also less than 10%, so they may cause small-signal instability. As Prony analysis cannot differentiate noise signals, signals with energy greater than 10^{-5} are considered spurious. Figure 22 shows the mean squared error between the original signal and the Prony approximation at Rourkela.

Table 9: Prony Analysis of Frequency Variation at Sasaram

Mode	Amplitude(Hz)	Damping(%)	Frequency(Hz)	Energy(J)
1	5.8e-02	68	0.03	8.4e-05
2	2.4e-02	1.7	0.031	1.2e-03
3	3.0e-03	1.5	0.91	2.0e-05
4	3.0e-03	1.5	0.91	2.0e-05
5	3.6e-04	1.7	6.2	2.5e-07
6	3.6e-04	1.7	6.2	2.5e-07
7	2.6e-04	1.6	3.9	1.4e-07
8	2.6e-04	1.6	3.9	1.4e-07
9	1.7e-04	1.7	8.3	5.6e-08
10	1.7e-04	1.7	8.3	5.6e-08
11	1.2e-04	1.6	10	3.2e-08
12	1.2e-04	1.6	11	3.2e-08

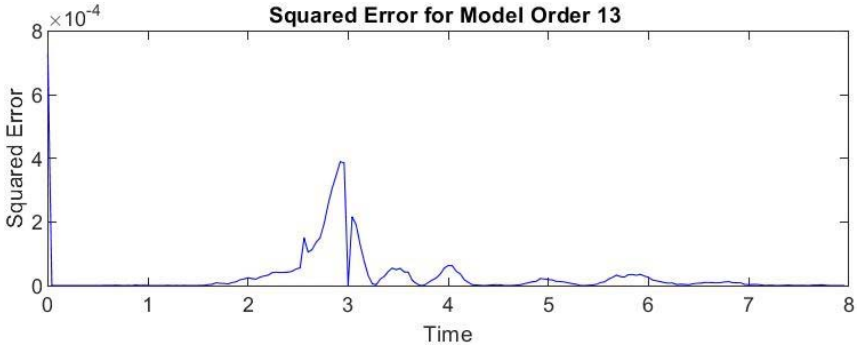

Fig. 23: Mean squared error of Prony analysis at Sasaram

Table 9 shows the respective modes, frequencies, damping, energies, and their corresponding amplitudes at Sasaram. From the results, it can be seen that the oscillations with frequencies 0.03 and 0.91 Hz are treated as low-frequency oscillations. Their energy is below the threshold, and their damping is also less than 10%, so they may cause small-signal instability. As Prony analysis cannot differentiate noise signals, signals with energy greater than 10^{-5} are considered spurious. Figure 23 shows the mean squared error between the original signal and the Prony approximation at Sasaram.

Table. 10: Prony Analysis of Frequency Variation at Talcher

Mode	Amplitude(Hz)	Damping(%)	Frequency(Hz)	Energy(J)
1	2.4e-02	1.0	0.031	1.9e-05
2	4.0e-03	6.2	8.0	1.0e-06
3	4.0e-03	6.2	8.0	1.0e-06
4	2.9e-03	5.7	9.4	6.0e-06
5	2.9e-03	5.7	9.4	6.0e-06
6	2.5e-03	5.7	6.0	4.2e-06
7	2.5e-03	5.7	6.0	4.2e-06
8	2.3e-03	1.3	0.75	1.4e-05
9	2.3e-03	1.3	0.75	1.4e-05
10	5.5e-04	3.0	3.6	3.5e-07
11	5.5e-04	3.0	3.6	3.5e-07
12	5.4e-04	3.9	11	2.8e-07
13	5.4e-04	3.9	11	2.8e-07

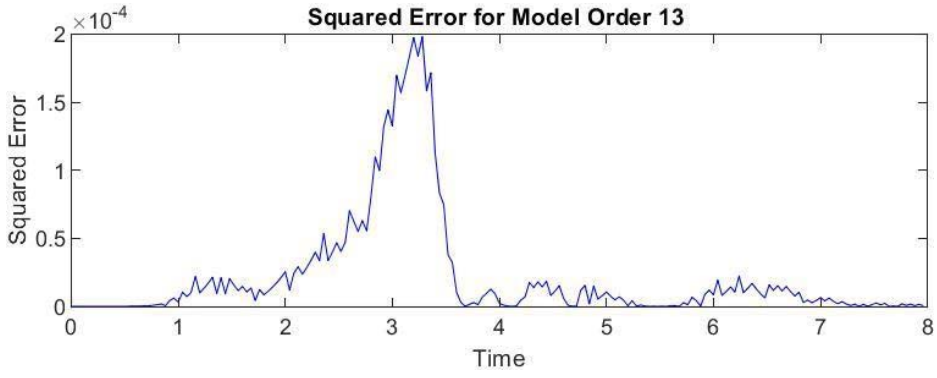

Fig. 24: Mean Squared Error of Prony Analysis at Talcher

Table 10 shows the respective modes, frequencies, damping, energies, and their corresponding amplitudes at Talcher. From the results, it can be seen that the oscillation with frequency 0.031 Hz is treated as a low-frequency oscillation. Its energy is below the threshold, and its damping is also less

than 10%, so it may cause small-signal instability. As Prony analysis cannot differentiate noise signals, signals with energy greater than 10^{-5} are considered spurious. Figure 24 shows the mean squared error between the original signal and the Prony approximation at Talcher.

Table 11: Prony Analysis of Frequency Variation at Rengali

Mode	Amplitude(Hz)	Damping(%)	Frequency(Hz)	Energy(J)
1	2.5e-02	0.93	0.031	2.2e-03
2	1.3e-03	0.94	0.71	6.2e-03
3	1.3e-03	0.94	0.71	6.2e-03
4	1.1e-03	2.8	1.2	1.6e-04
5	1.1e-03	2.8	1.2	1.6e-04
6	7.0e-04	5.6	5.8	3.4e-07
7	7.0e-04	5.6	5.8	3.4e-07
8	6.2e-04	2.3	9.5	5.7e-07
9	6.2e-04	2.3	9.5	5.7e-07
10	4.2e-04	3.3	7.4	2.0e-07
11	4.2e-04	3.3	7.4	2.0e-07
12	4.2e-04	2.3	3.7	2.4e-07
13	4.2e-04	2.3	3.7	2.4e-07

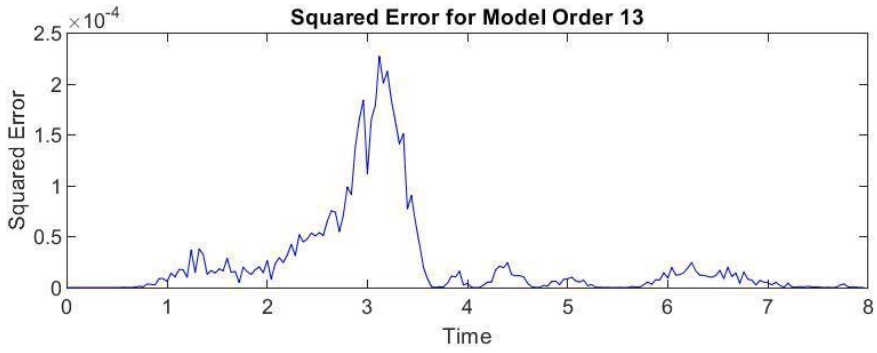

Fig. 25: Mean Squared Error of Prony Analysis at Rengali

Table 11 shows the respective modes, frequencies, damping, energies, and their corresponding amplitudes at Rengali. From the results, it can be seen that the oscillations with frequencies 0.031, 1.2, and 0.71 Hz are treated as low-frequency oscillations. Their energy is below the threshold, and their damping is also less than 10%, so they may cause small-signal instability. As Prony analysis cannot differentiate noise signals, signals with energy greater than 10^{-5} are considered spurious. Figure 25 shows the mean squared error between the original signal and the Prony approximation at Rengali.

Table 12: Prony analysis of frequency variation at Jamshedpur

Mode	Amplitude(Hz)	Damping(%)	Frequency(Hz)	Energy(J)
1	3.8e-02	13	12	5.6e-04
2	2.5e-02	0.83	0.031	2.5e-03
3	1.3e-02	8.0	11	1.0e-07
4	1.3e-02	8.0	11	6.0e-07
5	9.3e-04	3.8	8.3	6.0e-07
6	9.3e-04	3.8	8.3	4.2e-07
7	9.1e-04	3.6	6.3	4.2e-07
8	9.1e-04	3.6	6.3	1.4e-07

9	8.0e-04	5.7	0.87	3.5e-05
10	8.0e-04	5.7	0.87	3.5e-05
11	3.6e-04	3.7	4.0	1.2e-07
12	3.6e-04	3.7	4.0	1.2e-07

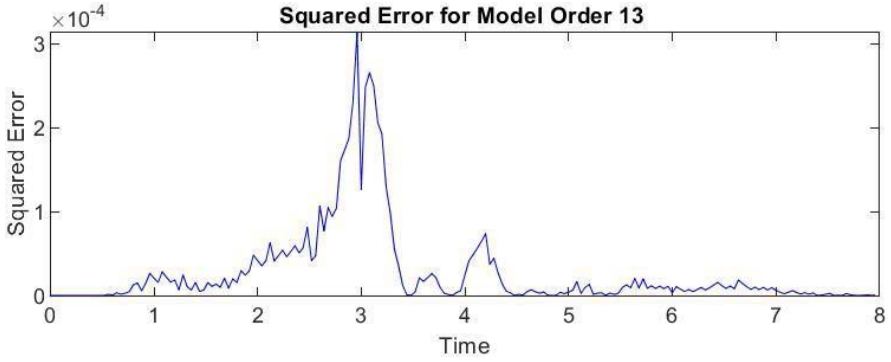

Fig. 26: Mean Squared Error of Prony Analysis at Jamshedpur

Table 12 shows the respective modes, frequencies, damping, energies, and their corresponding amplitudes at Jamshedpur. From the results, it can be seen that the oscillations with frequencies 0.031 and 0.87 Hz are treated as low-frequency oscillations. Their energy is below the threshold, and their damping is also less than 10%, so they may cause small-signal instability. The 12 Hz component is likely noise, as it is damped out very fast with a damping of 13%. As Prony analysis cannot differentiate noise signals, signals with energy greater than 10^{-5} are considered spurious. Figure 26 shows the mean squared error between the original signal and the Prony approximation at Jamshedpur.

IV. CONCLUSION

The stability of the Indian Eastern Regional Grid is frequently compromised by poorly damped Low-Frequency Oscillations (LFOs), a vulnerability amplified during system transients. This paper presents a detailed modal analysis of the cascading event that occurred on July 7, 2017, initiated by a fault on the 400 kV Rangpo–Binaguri (RB)-II line, which led to the System Protection Scheme (SPS) action and the eventual loss of the Teesta-III corridor.High-resolution synchro phasor data from 12 Phasor Measurement Units (PMUs) across the region were processed using Prony Analysis to accurately extract the frequency, damping percentage, and energy of the oscillatory modes. The low-frequency oscillations (LFOs) were detected at various locations. It was found that the 0.031 Hz component of LFOs is present at almost all locations, with comparatively low damping, indicating that this component requires close monitoring to prevent potential small-signal instability. At Binaguri and Rengali, most of the LFOs were observed, with frequencies of 1.8, 1.81, 0.92 Hz and 0.031, 0.71, 1.2 Hz, respectively. Although the amplitudes of these LFOs are low at all locations, the damping is consistently below 10%, indicating that the LFOs are somewhat predominant and sustain for a longer duration, which may cause small-signal instability in the system. Spurious noise signals were also observed at all locations, highlighting the inability of Prony analysis to differentiate between actual and noise signals. The mean squared error across all locations confirms the high accuracy of the Prony analysis. For performing these analyses, the data obtained from PMUs is the fundamental building block. It can be concluded that for real-time dynamic monitoring and obtaining accurate results, WAMS plays a critical role. Hence, a Wide Area Measurement System (WAMS) enhances the operation, monitoring, and control of complex power systems through synchro phasor measurement technology.

REFERENCES

1. C. Q. Liu, "A discussion of the WSCC 2 July 1996 outage," *IEEE Power Engineering Review*, vol. 18, no. 10, pp. 60–61, 1998.
2. U. S.-Canada Power Systems Outage Task Force, *Final Report on the August 14, 2003 Blackout in United States and Canada*, 2004.
3. A. Andersson, P. Donalek, and R. Farmer, "Causes of the 2003 major grid blackouts in North America and Europe, and recommended means to improve system dynamic performance," *IEEE Trans. Power Syst.*, vol. 20, no. 4, pp. 1922–1928, 2005.
4. M. Donolo, "Advantages of synchro phasor measurements over SCADA measurements for the power system state estimation," SEL Application Note LAN2006-10.
5. M. V. Mynam, A. Harikrishna, and V. Singh, *Synchro phasors Redefining SCADA Systems*, SEL, Inc., 2011.
6. M. A. Abdullah Sufyan, M. Zuhaib, M. Sefid, and M. Rihan, "Analysis of Effectiveness of PMU based Wide Area Monitoring System in Indian Power Grid," *2018 5th IEEE Uttar Pradesh Section International Conference on Electrical, Electronics and Computer Engineering (UPCON)*, 2018.
7. S. Soni, S. Bhil, D. Mehta, and S. Wagh, "Linear state estimation model using Phasor Measurement Unit (PMU) technology," *ICEE 2012*.
8. M. Hurtgen and J.-C. Maun, "Advantages of power system state estimation using Phasor Measurement Units," *Research Gate*, [Online]. Available. https://www.researchgate.net/publication/228892103-lseadv.
9. P. Ray, "Power system low frequency oscillation mode estimation using wide area measurement systems," *Engineering Science and Technology, an International Journal*, 2016. [Online]. Available: http://dx.doi.org/10.1016/j.jestch.2016.11.019.
10. S. Chitturi, S. Chakrabarti, and S. N. Singh, "Comparing performance of Prony analysis and Matrix pencil method for monitoring power system oscillations," *IEEE*, 2014, pp. 1–6.
11. D. P. Wadduwag, U. D. Annakkage, and K. Narendra, "Identification of dominant low-frequency modes in ring-down oscillations using multiple Prony models," *IET Gener. Transm. Distrib.*, pp. 1–9, 2015.
12. V. Rampurkar, F. Kazi, H. A. Mangalvedekar, P. Pentayya, C. Kumar, and R. A., "PMU Based Identification of Low Frequency Oscillations – A Case Study," *IEEE ISGT Asia*, 2013.
13. P. P. Dalawai and V. Pandey, "Application of synchrophasors – A case study in northern regional power system in India," *Water and Energy International*, Feb. 2013. [Online]. Available: https://www.researchgate.net/publication/289491655-prony.
14. P. Puviya and N. Priyadarshini, "State estimation in power system using weighted least squares method," *2017 International Conference on Innovations in Information, Embedded and Communication Systems (ICIIECS)*, 2017, pp. 1–6.

Objective Evaluation Criteria for the Safety Certification of Autonomous Navigation System

Shinya Nakamura & Tomoaki Yamada

ABSTRACT

In Japan, the commercialization of the autonomous ship is aiming at the full-scale commercial operation around 2030 with the cooperation of industry, academia and government. The autonomous navigation system that the ships will be equipped with is one of the main functions of the autonomous ship. Commercialized autonomous ships coming soon are scheduled to operate on domestic routes. In areas covered by the Collision avoidance Regulations (COLREGs), autonomous ships will basically navigate without human intervention, including in congested waters. The Japan Captains' Association believes that ships equipped with such autonomous navigation systems must have the same safety level as conventional ships and comply with the COLREGs. In other words, the autonomous ship should not cause anxiety to encountering ships. Based on the above basic policy, the Japan Captains' Association and ClassNK conducted a large-scale verification experiment aimed at formulating standards for classification companies to objectively evaluate the safety of autonomous navigation systems and developed evaluation area diagrams for certification.

Keywords: NA

Classification: LCC Code: VM300

Language: English

Great Britain Journals Press

LJP Copyright ID: 392964
Print ISSN: 2631-8474
Online ISSN: 2631-8482

London Journal of Engineering Research

Volume 25 | Issue 6 | Compilation 1.0

Objective Evaluation Criteria for the Safety Certification of Autonomous Navigation System

Shinya Nakamura[α] & Tomoaki Yamada[σ]

ABSTRACT

In Japan, the commercialization of the autonomous ship is aiming at the full-scale commercial operation around 2030 with the cooperation of industry, academia and government. The autonomous navigation system that the ships will be equipped with is one of the main functions of the autonomous ship. Commercialized autonomous ships coming soon are scheduled to operate on domestic routes. In areas covered by the Collision avoidance Regulations (COLREGs), autonomous ships will basically navigate without human intervention, including in congested waters. The Japan Captains' Association believes that ships equipped with such autonomous navigation systems must have the same safety level as conventional ships and comply with the COLREGs. In other words, the autonomous ship should not cause anxiety to encountering ships. Based on the above basic policy, the Japan Captains' Association and ClassNK conducted a large-scale verification experiment aimed at formulating standards for classification companies to objectively evaluate the safety of autonomous navigation systems and developed evaluation area diagrams for certification. This paper introduces the evaluation area diagrams that objectively evaluates autonomous navigation systems to have the same or higher safety level as conventional ships and to objectively evaluate compliance with COLREGs. In the evaluation area diagram, "Safety area", "Caution area", and "Danger area" are calculated based on the relative distance and bearing (compass bearing) change rate etc, between the autonomous ship and the encountered ships. When a ship using an autonomous navigation system navigates in a way that avoids entering "Caution area" and "Danger area", it can be said that the ship is reducing risk before there is a risk of collision.

ClassNK will use the evaluation area diagram introduced here to carry out certification work for the autonomous navigation system which will undergo demonstration experiments in 2025.

This paper also discusses how to objectively explain compliance with the COLREGs, which contains many ambiguous expressions.

Author α: President, Japan Captains' Association, Tokyo, Japan.
σ: ClassNK, Tokyo, Japan.

I. INTRODUCTION

In Japan, the autonomous ship (MASS) has been undergoing long-term demonstration experiments with the aim of implementing it in society. One of the main functions of MASS is the autonomous navigation system (ANS), an automatic collision avoidance system.

The Japanese government's Ministry of Land, Infrastructure, Transport and Tourism and ClassNK have stated that the basic approach to the inspection and certification of autonomous ships is that "ANS must ensure the same level of safety as conventional ships and comply with the Collision avoidance Regulations (COLREGs)". This basic concept is agreed upon by maritime stakeholders, including the Japan Captains' Association. In accordance with this basic concept, the Japan Captains' Association has proposed the following specific desirable requirements for ANS.

London Journal of Engineering Research

It is desirable for ANS to take advantage of its characteristic of being able to process a lot of information simultaneously without oversight anything and to perform risk reduction manoeuvres in advance. By performing risk reduction manoeuvres in advance, it is possible to ensure the same level of safety as conventional ships without violating COLREGs. In other words, it is important for ANS to perform risk reduction manoeuvres in advance so as not to cause anxiety to other ships. The reason for making this proposal is that, based on the current capabilities of ANS [1][2][3][4], although it has advantages over human navigation, such as fewer oversights, it is difficult to operate a ship in full compliance with COLREGs, which contains many ambiguous expressions.

Based on this idea, the authors have developed an automatic collision avoidance system and proposed an evaluation area diagram [5][6]. The paper aims to consider objective criteria for ClassNK to certify ANS in practice in 2025 and reports the results of new large-scale simulator experiments and a questionnaire survey carried out to improve the previously proposed evaluation area diagram.

II. TOWARDS THE CERTIFICATION OF COMPLIANCE WITH COLREGS

The Japan Captains' Association has held a study session on COLREGs with ClassNK for the purpose of certifying that ANS comply with COLREGs. In particular, detailed explanations were given on Section II, Article 17 (Action by stand-on vessel), and Part A, Article 2 (Ordinary practice of seaman) of COLREGs.

Figure 1 is an example of the rules regarding the behaviour of stand-on vessels that were explained to ClassNK at the study session. In addition to the rules for keeping the course and speed of stand-on vessels stipulated in Article 17(a)(i) of COLREGs, there are rules such as 17a(ii), 17b, Rule2a, Rule2b, etc. (within the square frame in Figure 1). However, there is no specific description of when and how to perform the best aid to avoid collision (the best cooperative action) in 17b. There is also no specific description of what should be done for "Ordinary practice of seamen". As such, COLREGs contains many ambiguous expressions, making it difficult for ANS development engineers who are not seafarers to understand.

Figure 2 shows the ship encounter situation (actual data from November 2024) based on AIS data in the sea area where domestic container ships that will undergo long-term demonstration experiments on a new MASS in 2025 will be sailing. There is a high possibility that ship A will be a stand-on vessel against ships B and C according to Article 17. Ships B and C may also be stand-on vessels against ships D and E. If ship A maintains its course and speed against ships B and C, while ships B and C also maintain their course and speed as stand-on vessels against ships D and E, and ship A approaches ships B and C quite closely and then performs a hard starboard turn as a best aid to avoid collision according to Article 17b, it may cause anxiety to other ships sailing nearby and create an extremely dangerous situation. MASS needs to avoid getting into such a situation as much as possible. The manoeuvring method of ship A recommended by Japan Captains' Association is to change course slightly in advance so as not to become a stand-on vessel against ships B and C, and at the same time consider passing ships D and E port-to-port.

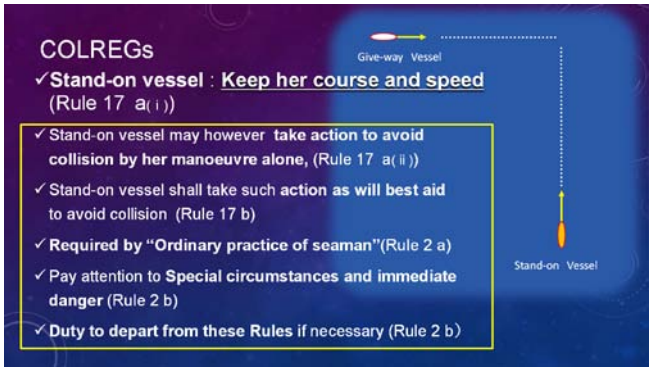

Figure 1: Rules Relating to Vessel That May Become Stand-On Vessel as Described in Colregs

Figure 2: The Ship Encounter Situation based on Ais Data (Actual Data from November 2024)

This type of manoeuvring should be considered to be applicable to Article 2 (Ordinary practice of seamen) of COLREGs, not Article 17 (Stand-on vessel). In Japan Marine Accident Tribunal, "Ordinary practice of Seaman" is often applied as the cause of an accident.

As these examples show, Japan Captains' Association proposed that it is desirable for MASS to perform risk reduction manoeuvre in advance so as not to violate COLREGs and to not cause anxiety to other ships. And, also pointed out that, at the current level of technology, unless such an approach is adopted for the time being, it will be difficult to provide a rational explanation for not violating COLREGs.

Specific objective criteria are required to fairly evaluate the "risk reduction manoeuvre in advance" proposed by Japan Captains' Association. The evaluation area diagrams proposed previously [6] was formulated based on the results of experiments conducted quite some time ago. So large-scale verification experiment and a questionnaire survey were conducted by Japan Captains' Association and ClassNK in order to formulate new evaluation area diagrams that will serve as a more reliable objective criterion for the ANS certification.

III. LARGE-SCALE VERIFICATION EXPERIMENTS FOR FORMULATING THE EVALUATION AREA DIAGRAM

3.1 Overview of the Verification Experiments

In order to formulate new objective certification criteria, large-scale experiments were conducted using a ship manoeuvring simulator and evaluation area diagrams were formulated. The evaluation area diagrams follow the basic concept of the area diagrams proposed previously [6] and were conducted from 2022 to 2023 with the aim of improving reliability. They were as conducted with the full cooperation of major Japanese shipping companies that own full mission ship-handling simulators, NYK Line, Mitsui O.S.K. Lines, and K Line. The relative distance between MASS and other ships that encounter it, and the bearing change rate (also some closest point of approach distances / CPA

Table 1: The Definition of Evaluation Area

Category	Definition
"Safetyarea"	Acceptable area
"Caution area"	The area where own ship commences to avoid or expect another ship to avoid
"Danger area"	Unacceptable area

distance) were used as indicators to formulate the evaluation area. The evaluation area was classified into "Safety area," "Caution area," and "Danger area" as defined in Table 1.

Even in situations where it is difficult to evaluate using only relative distance, by combining relative distance and the bearing change rate, it is possible to formulate an evaluation area diagram that is easy for seafarers to understand.

A total of 1,631 captains participated in the experiment, and verification experiments were conducted to develop evaluation area diagrams using 181 experimental cases. Experimental scenarios were prepared with multiple bearing change rates at any given relative distance, and captains/evaluators entered into the recorder the situation defined in Table 1 that corresponded to their situational awareness of being on board a target vessel that had encountered an autonomous vessel. Scenarios were prepared for the crossing case, with a bearing change rate of 1.2deg/min. to 9.0deg/min. at 1.5 miles. (The 1.5 miles point was chosen as the representative point for setting the bearing change rate.) In addition, scenarios were prepared for the same-way situation and overtaking and head-on situation, with the closest point of approach (CPA) distance was 0.1miles to 0.85miles. Captains/evaluators will board ships are set to LOA:147.9m to 400.0 m. The target autonomous ships are assumed to be autonomous ships that will undergo demonstration experiments in Japan in 2025 and are set to LOA: 81.5m to 107.4m in size. Additionally, to grasp the impact that differences in the size of MASS have on the area diagram, a ship (MASS) with LOA 333m was also added to the scenario.

Usually, when conducting such evaluation experiments, the scenario is set by setting only the closest point of approach (CPA) distance parametrically. However, this time, the evaluation area diagram is created by combining the relative distance and the bearing change rate, so the scenario setting work is somewhat complicated, but in the case of crossing situation, the scenario was set to change the bearing change rate parametrically at a relative distance of 1.5 miles.

One of the experimental scenarios is shown in Figure 3. This is the case where the bearing change rate is 2.1deg./min. when the relative distance is 1.5 miles (A scenario in which a MASS passes the bow of a target ship on which captains/evaluators are aboard). Part of the experimental results for this case are shown in Figure 4. The horizontal axis represents the relative distance, and the vertical axis represents the recognition status of six evaluators. Almost all six evaluators changed from "Safety" to "Caution" at

a relative distance of about 1.8 to 2 miles. The relative distance at which the recognition changes from "Caution" to "Danger" varies from almost 1miles to1.5 miles.

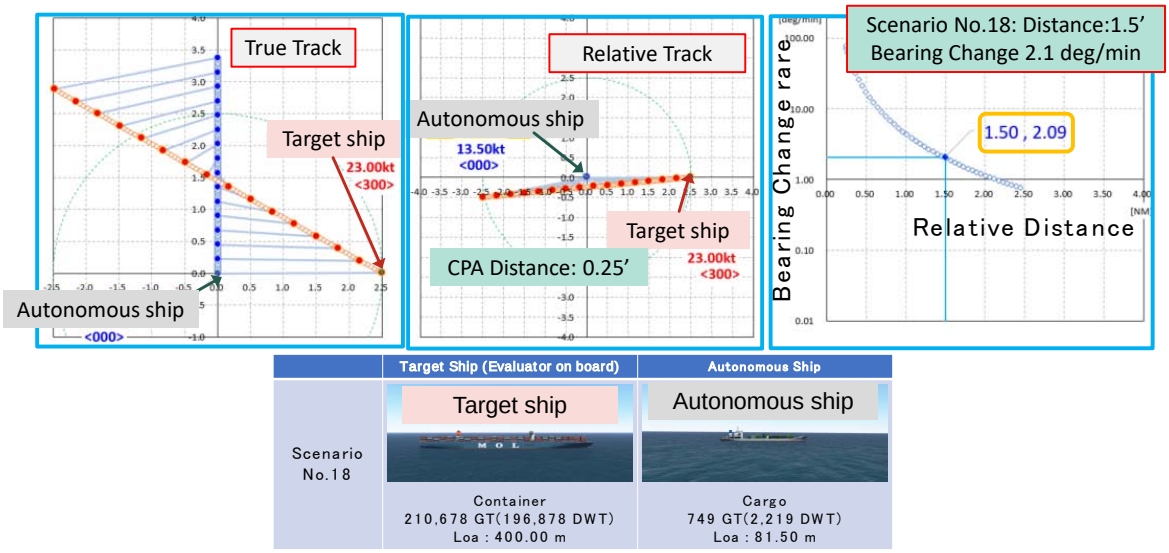

Figure 3: One of the Experimental Scenarios, the Case Where the Bearing Change Rate is 2.1deg./Min. When the Relative Distance is 1.5 Miles (A Scenario in Which a Mass Passes the Bow of a Target Ship on Which Captains/Evaluators are Aboard)

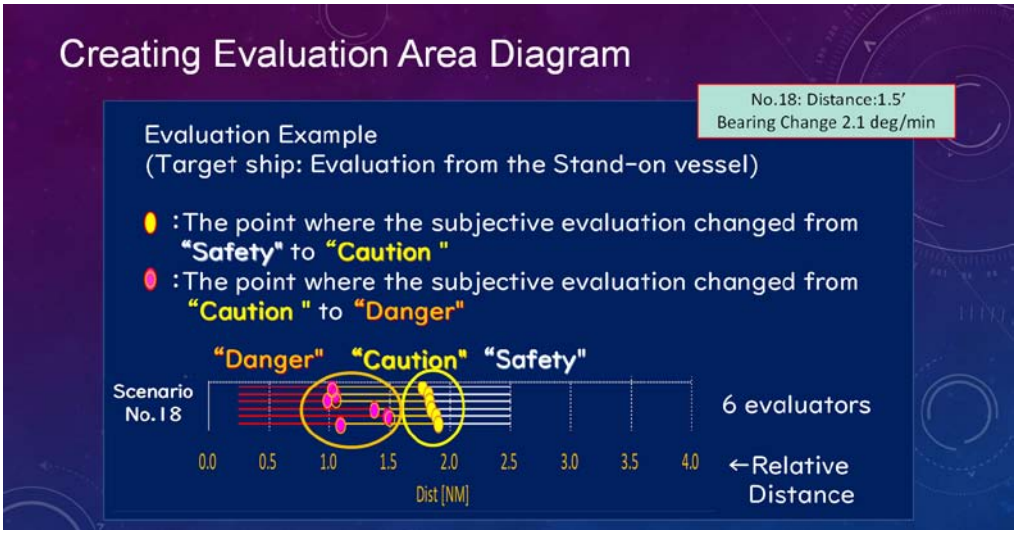

Figure 4: One of the Experimental Results, the Case Where the Bearing Change Rate is 2.1deg./Min. When the Relative Distance is 1.5 Miles (A Scenario in Which a Mass Passes the Bow of a Target Ship On Which Captains/Evaluators Are Aboard)

As shown in Figure 5, the experimental results were plotted by plotting the baring change rate at which 75% of the subjects changed their evaluation awareness from "safety" to "caution" or from "caution" to "danger" for every 0.1 mile of relative distance, and a regression equation was developed for the plot points. The vertical axis showing the bearing change rate is in logarithmic notation.

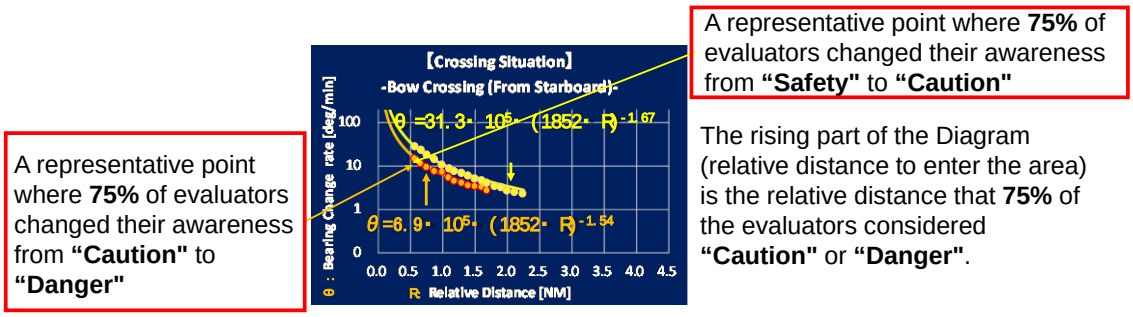

Figure 5: The Experimental Result (Crossing Situation/Bow Crossing from Starboard)

Crossing and overtaking are shown by relative distance and bearing change rate, while head-on situation is shown by relative distance and closest point of approach (CPA) distance.

The evaluation formula showing the boundary of the area determined from the experimental results is shown in Figure 6 and Figure 7. The details of the regression formula are shown in Figure 8.

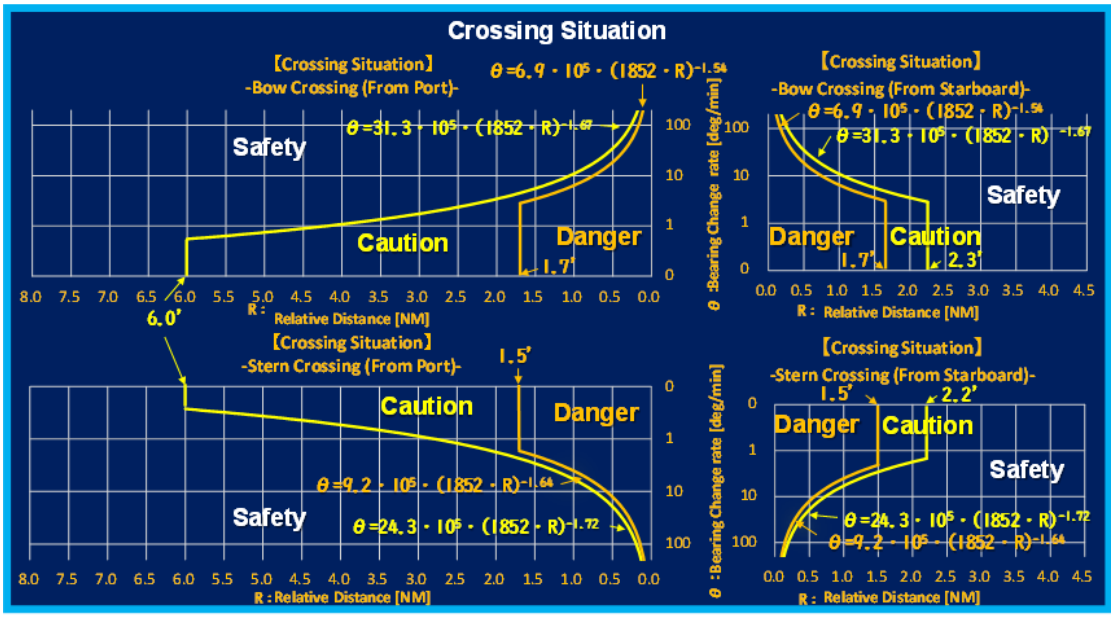

Figure 6: The Newly Created Evaluation Area Diagram (Crossing Situation)

Figure 6 shows the case of crossing, but for crossing from the port side, the starting point is 6 miles, which is the distance that avoids becoming a stand-on vessel as much as possible. These 6 miles is the result of a questionnaire survey conducted separately from the verification experiment. The questionnaire survey will be described in the next section.

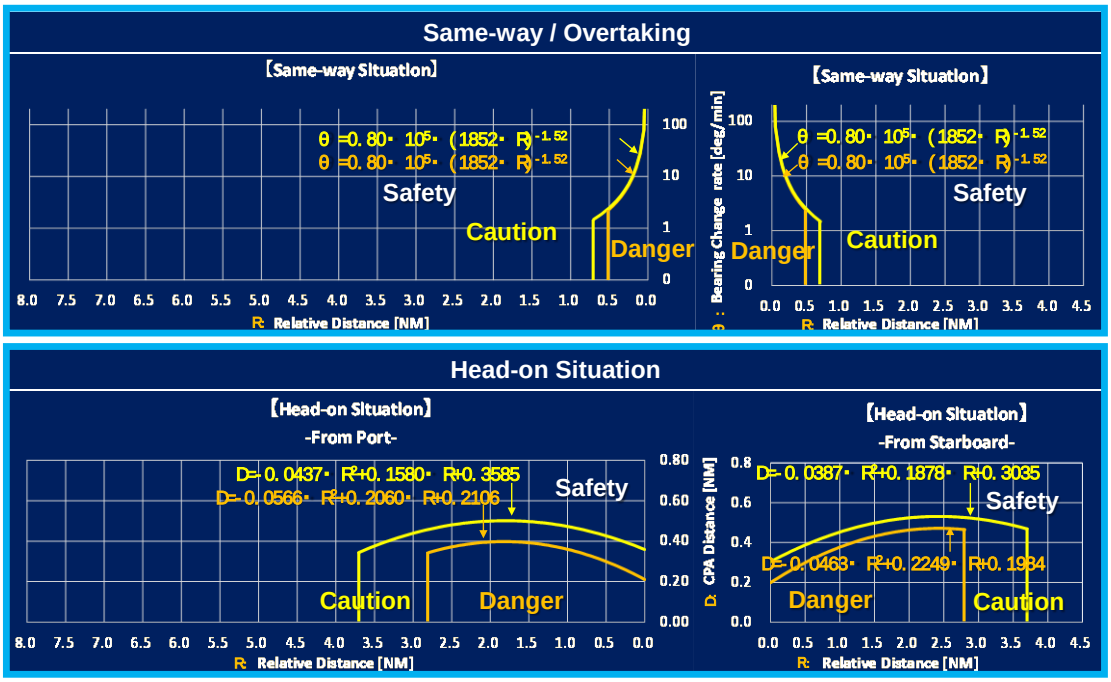

Figure 7: The Newly Created Evaluation Area Diagram (Same-Way, Overtaking, Head-On Situation)

Encounter situation		*Evaluation boundary formula*		*Evaluation*
Crossing from Starboard	Bow Crossing	$\theta \leqq 6.90 \times 10^5 \times (1852 \times R)^{-1.54}$	R < 1.7 [NM]	Danger
		$\theta \leqq 31.30 \times 10^5 \times (1852 \times R)^{-1.67}$	R < 2.3 [NM]	Caution
		Range excluding danger area and caution area		Safety
	Stern Crossing	$\theta \leqq 9.20 \times 10^5 \times (1852 \times R)^{-1.64}$	R < 1.5 [NM	Danger
		$\theta \leqq 24.30 \times 10^5 \times (1852 \times R)^{-1.72}$	R < 2.2 [NM]	Caution
		Range excluding caution area		Safety
Crossing from Port	Bow Crossing	$\theta \leqq 6.90 \times 10^5 \times (1852 \times R)^{-1.54}$	R < 1.7 [NM]	Danger
		$\theta \leqq 31.30 \times 10^5 \times (1852 \times R)^{-1.67}$	R < 6.0 [NM]	Caution
		Range excluding danger area and caution area		Safety
	Stern Crossing	$\theta \leqq 9.20 \times 10^5 \times (1852 \times R)^{-1.64}$	R < 1.5 [NM	Danger
		$\theta \leqq 24.30 \times 10^5 \times (1852 \times R)^{-1.72}$	R < 6.0 [NM]	Caution
		Range excluding caution area		Safety
Same-way	From Starboard / Port	$\theta \leqq 0.8 \times 10^5 \times (1852 \times R)^{-1.52}$	R < 0.5 [NM]	Danger
		$\theta \leqq 0.8 \times 10^5 \times (1852 \times R)^{-1.52}$	R < 0.7[NM]	Caution
		Range excluding caution area		Safety
Head-on	From Starboard	$D \leqq -0.0463 \times R^2 + 0.2249 \times R + 0.1984$	R < 2.8 [NM]	Danger
		$D \leqq -0.0387 \times R^2 + 0.1878 \times R + 0.3035$	R < 3.7 [NM]	Caution
		Range excluding danger area and caution area		Safety
	From Port	$D \leqq -0.0566 \times R^2 + 0.2060 \times R + 0.2106$	R < 2.8 [NM]	Danger
		$D \leqq -0.0437 \times R^2 + 0.1580 \times R + 0.3585$	R < 3.7 [NM]	Caution
		Range excluding caution area		Safety

θ: Rate of change in bearing [deg./min] D: CPA Distance [NM: Nautical Mile] R: Relative distance [NM: Nautical Mile]

Danger	: Unacceptable area
Caution	: The area where own ship commence to avoid or expect another ship to avoid
Safety	: Acceptable area

Figure 8: the Details of the Regression Formula (Evaluation Boundary Formula)

3.2 Example of Evaluation using Evaluation Area Diagram

Figure 9 shows the situation as seen from the autonomous ship (the give-way vessel) and the target ship (the stand-on vessel) in a typical crossing situation, reproduced by a simulator.

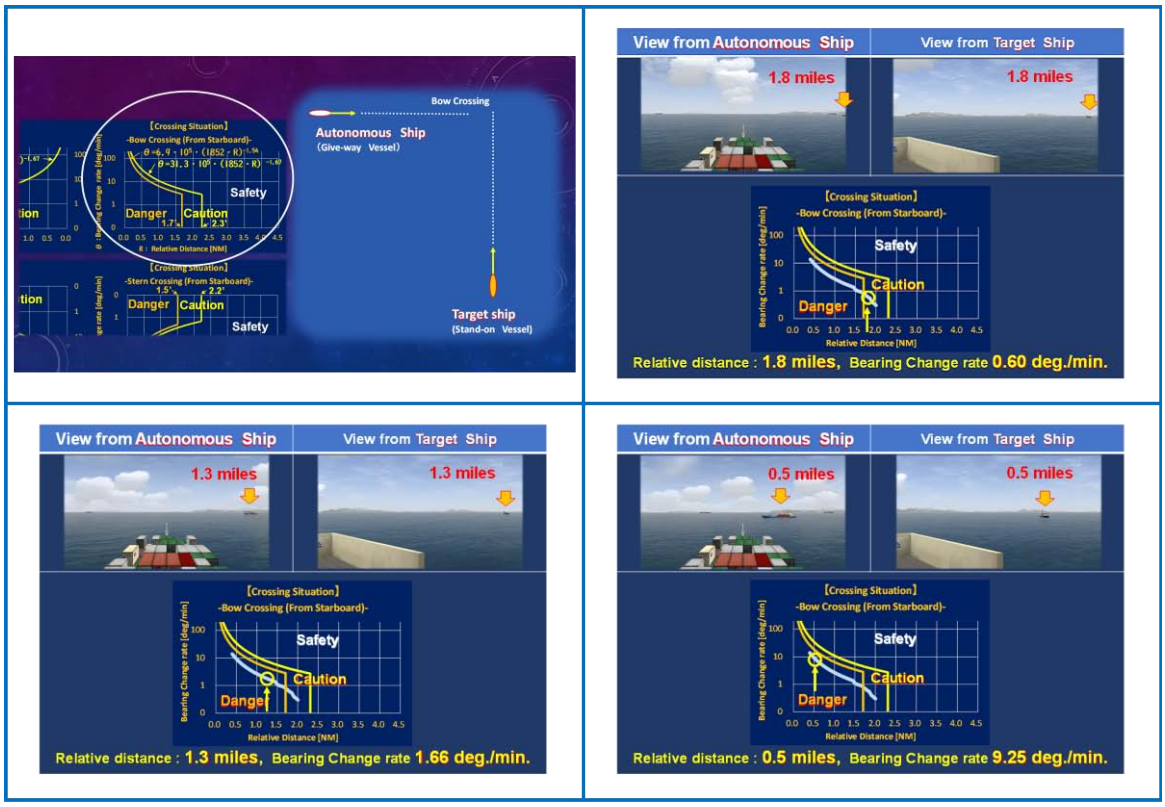

Figure 9: Example of Evaluation using Evaluation Area Diagram

At a relative distance of 1.8 miles, the bearing change rate is 0.60 deg./min., plotted in the "Caution area." (In the figure, top right). At a relative distance of 1.3 miles, the bearing change rate is 1.66deg/min., entering the "Danger area." (In the figure, bottom left). At a relative distance of 0.5 miles, the autonomous ship is about to pass by its bow, with the bearing change rate of 9.25 deg./min. (In the figure, bottom right). A collision is avoided, but the autonomous give-way vessel is still showing its starboard side.

In this situation, the target ship passed the bow of the autonomous ship at a distance of 0.4 miles, but in the newly formulated evaluation area diagram, 75% of the captains evaluated this situation as unacceptable. The certification standard for autonomous ships requires that the autonomous ship takes avoidance action with sufficient bearing change rate (more than 10 deg./min.) and with ample time (more than 2.3 miles away).

IV. QUESTIONNAIRE SURVEY

It is desirable for an autonomous ship to avoid situations where it is necessary to perform the "best aid to avoid collision" of COLREGs Article 17 shown in Figure 1 and Figure 2. As already mentioned, given the current level of ANS technology, acting to avoid becoming a stand-on vessel as much as possible will not violate COLREGs and will not cause anxiety to other ships that encounter it. In order to encourage such proactive risk reduction manoeuvres, a questionnaire survey was conducted to understand the distance at which the "Caution area" should be raised for crossing from the port, as shown in Figure 6.

The questionnaire survey asked, “in a situation where there is a possibility that a MASS encountered in a crossing may become a stand-on vessel, up to what distance would be acceptable for that MASS to perform risk reduction manoeuvre? “. In other words, from what distance would a stand-on vessel need to keep its course and speed.

The questionnaire was conducted with the cooperation of shipping companies and ship management companies, and responses were received from 523 captains from 12 countries. The nationalities of the captains who responded are shown in Figure 10.

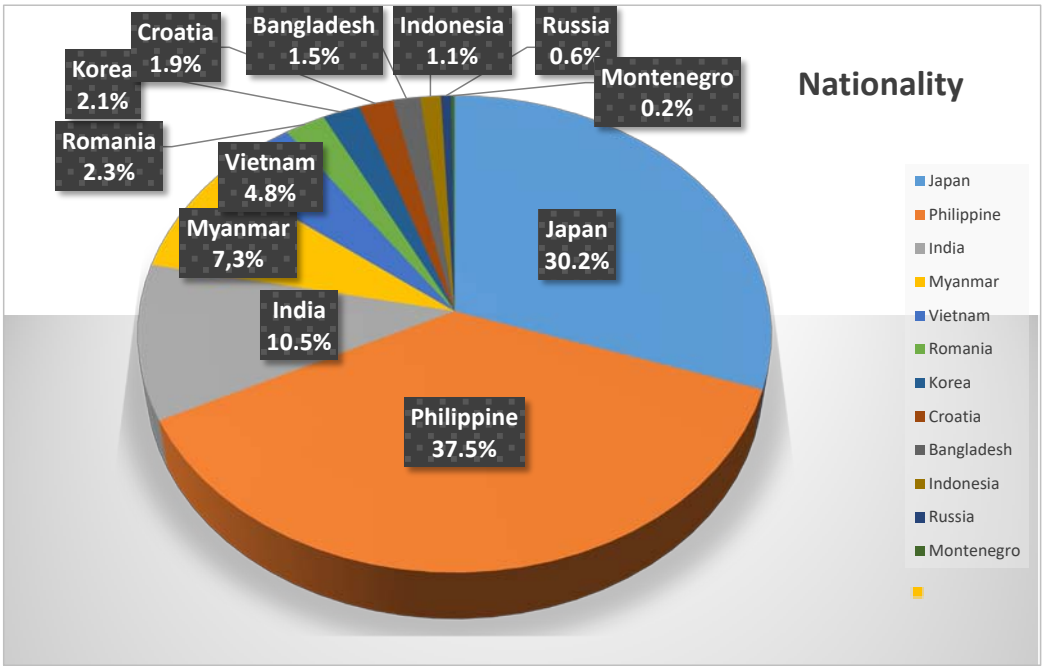

Figure 10: The Nationalities of the Captains Who Responded to the Questionnaire Survey

The questionnaire asked questions based on the LOA of their own ship (the ship the survey respondents assumed to be aboard) being between 100m and 360m, and the LOA of the other ship they may encounter (MASS that may become a stand-on vessel) being 100m. Figure 11 shows the results when the LOA of the own ship is 100m and the LOA of the other ship (MASS) is 100m. The left side of the figure shows examples of responses by distance, with the first one being a Japanese response, the second being a non-Japanese response, and the third being all responses. The right side shows the cumulative totals from the closest distance. The distance at which the cumulative total reached 75% was 6 miles. The cumulative total distance at which the cumulative total reached 75% varied slightly depending on the size of the ship, but 6 miles was used as the average.

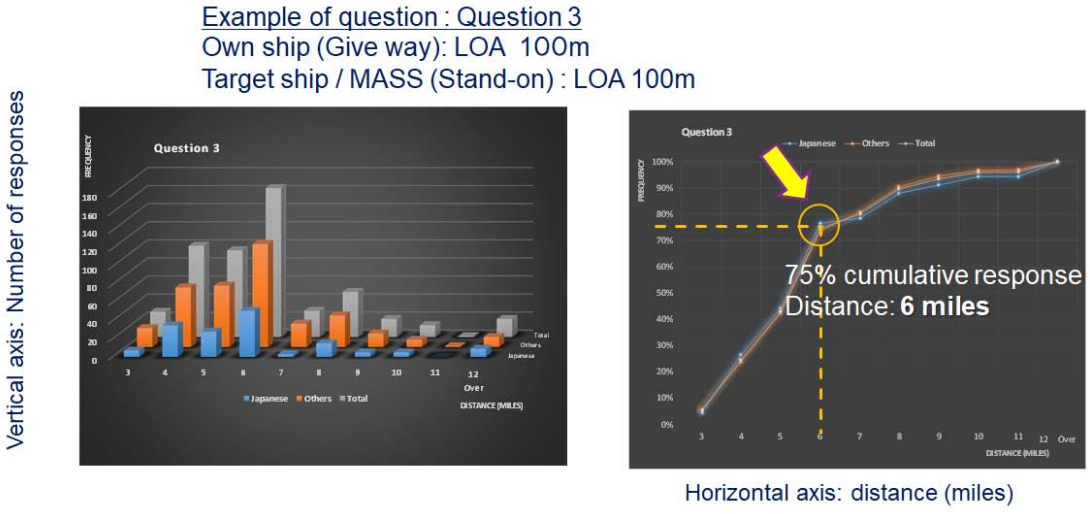

Figure 11: Part of The Questionnaire Survey Results

V. EXAMPLE OF CERTIFICATION USING EVALUATION AREA DIAGRAM (SIMULATED CERTIFICATION)

Verification is carried out using a ship-handling simulator incorporating the ANS to be certified. The scenario in Figure12 is a scenario simulated for demonstration purposes. [7]

The target MASS is a PCC (LOA: 200m). The MASS is surrounded by crossing ships from starboard (①, ②, ④), a ship sailing in the opposite direction (Head-on) from port head (③), a ship sailing slightly faster than the MASS at 300m starboard side (⑤), and ships crossing from port (⑥, ⑦), making it a difficult scenario to manoeuvre.

The results of automatic manoeuvring of the PCC incorporating the simulated verification ANS are shown in the top row of Figure 13. The results are shown as ships tracks and a time series of speed and steering conditions. First, the ship slowed down because there was a same-way ship ⑤ 300m to starboard that was slightly faster than MASS. After that, the ship changed course to starboard, avoided the same-way ship on the starboard side, resumed speed, and headed north on the original course.

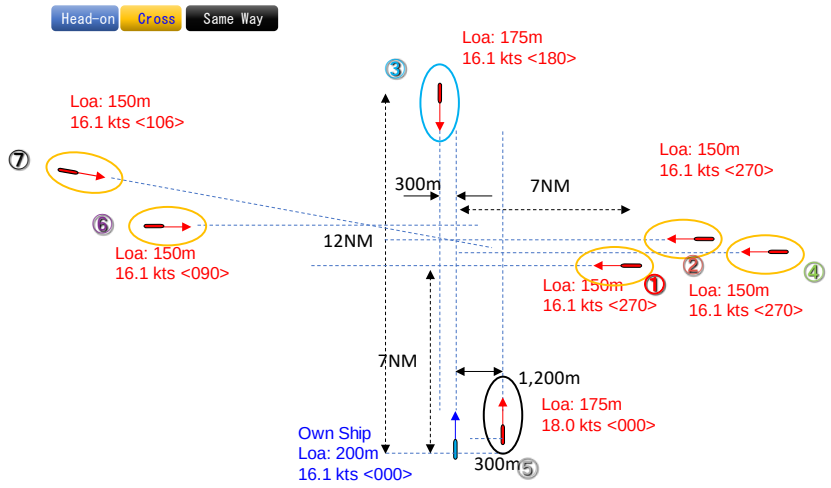

Figure 12: Scenario for Demonstration

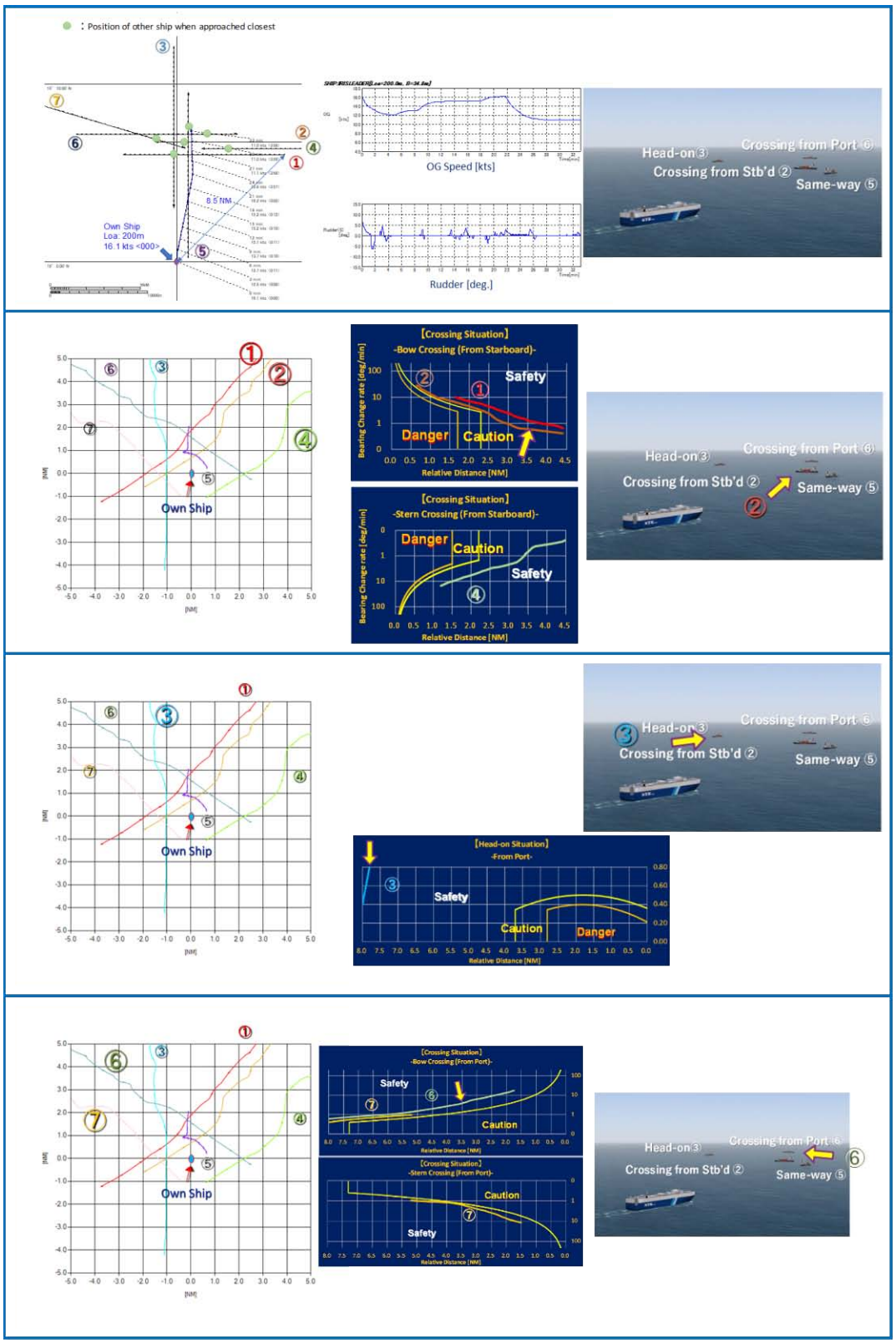

Figure 13: Example of Certification using Evaluation Area Diagram (Simulated Certification)

The relative tracks and evaluation area diagram of the ANS manoeuvring results are shown in the second and subsequent rows of Figure 13. As shown in the evaluation area diagram, there was a sufficient bearing change rate for crossing ship ② approaching from starboard, and it was passed within the "Safety area".

In order to avoid the same-way ship coming from port head, the course was changed to the starboard, therefore head-on ship ③ was passed within a sufficient “Safety area”. Crossing ships ⑥ and ⑦ from port were also passed within “Safety area”, and MASS passed these ships without becoming a stand-on vessel.

During this simulated certification, no navigation through caution or danger zones area was observed, and the ship's tracks and manoeuvring methods were also deemed appropriate, so it has been determined that there are no problems with certification.

In addition, the ClassNK guidelines state that if a ship ends up entering an "Caution area" or "Danger area" the duration of the intrusion will be taken into consideration, and an evaluation will be made by "experts" such as the captain, with a final decision on whether or not to grant certification.

SUMMARY

The Summary of this Paper is as Follows:

- Through large-scale verification experiments and questionnaire survey, a practical “Evaluation area diagram" for evaluating ANS was successfully introduced.
- The newly developed "Evaluation area diagram" is based on the idea that it is desirable for ANS to take advantage of its characteristic of being able to process a lot of information simultaneously without oversight anything and to perform risk reduction manoeuvres in advance.
- If it is possible to navigate in the “Safety area” using this “Evaluation diagram”, it can be explained that COLREG is complied with.
- Although it is judged that this evaluation method has reached a practical level, future issues are noted below.
  - It has been confirmed that if the hull size of a ship navigating with ANS increases, the “Evaluation area diagram” will expand. A sufficient number of data has not necessarily been obtained regarding the spread of the “Evaluation area diagram” due to the size of the autonomous ship. This is an issue for the future. (Some experimental results suggest that when MASS’s LOA is increased to 300m, evaluation area increases by 5% to 10%)
- Currently, when actually carrying out certification, if an autonomous ship enters a " Caution area" or "Danger area" it is necessary for experienced captains to judge the situation.
- ClassNK states in its guidelines “Guidelines for Automated/Autonomous Operation on ships (Ver2.0)” [8] that the evaluation area diagram introduced here will be used.

REFERENCES

1. K. Woerner, M.R. Benjamon, M. Novitzky et al: “Quantifying protocol evaluation for autonomous collision avoidance”, Autonomous Robots, Vol 43, pp 967-991, 2019.
2. P. Zhai, Y. Zhang, W. Shaobo: “Intelligent Ship Collision Avoidance Algorithm Based on DDQN with Prioritized Experience Reply under COLREGs”, Journal of Marine Science and Engineering, Vol.10, No.5, 2022.
3. Shinya Nakamura, Naoki Okada: “Study on Automatic Collision Avoidance Manoeuvre Using Full Mission Simulator”, Proc. MARSIM: International conference on marine simulation and ship manoeuvrability 2018, Halifax, Aug. 2018.
4. Tomoaki Yamada et al. “Study on Quantitative Evaluation Methode for collision Avoidance Function of Autonomous Manoeuvring System”, G-NAOE 2022.
5. Shinya Nakamura, Naoki Okada: “Development of Automatic Collision Avoidance System and Quantitative Evaluation of the Manoeuvring Results”, The International Journal on Marine Navigation and Safety of Sea Transportation (TRANSNAV), Vol 13, No.1, pp 133-141, 2019.3.

6. Shinya Nakamura *et al.* “Study on Automatic Collision Avoidance System and Method for Evaluating Collision Avoidance Manoeuvring Results”, Journal of Physics, Conference Series MTEC/ICMASS 2019 Vol.1357 (12033).
7. Shinya Nakamura, Naoki Okada: “Safety Evaluation of Automatic Collision Avoidance System”, Journal of Japan Institute of Navigation, Vol 142, p18-28, 2020.10 (Japanese).
8. ClassNK “Guidelines for Automated/Autonomous Operation on ships (Ver2.0)”, 2025.3.

This page is intentionally left blank

Designing High-Dense-Packed Electronic Equipment using Three-Dimensional Printed Wiring

Efimenko A. A.

ABSTRACT

Context: Many areas of modern electronic equipment, such as medical, automotive, portable, and special-purpose electronics, place increased demands on mass and volume. These devices often have irregular volume structures for accommodating electronic components. Therefore, 3D printed circuit boards are ideal for implementing such designs, and improving their efficiency, as well as optimizing the selection of mounting types, are pressing challenges.

Objective: The aim of this work is to develop a 3D printed circuit board method that is efficient in production and use, as well as a method for objectively selecting the optimal PCB option from the existing variety when designing miniature electronic equipment.

Method: The design and manufacturing method for manufacturing rigid-flexible printed circuit boards is based on traditional PCB manufacturing methods with an appropriate addition that allows for the achievement of three-dimensional design properties.

Keywords: a three-dimensional printed wiring; flexible printed circuit boards; rigid-flexible printed circuit boards; 3D-MID; optimal use of three-dimensional printed wiring.

Classification: DDC Code: 621.381

Language: English

Great Britain Journals Press

LJP Copyright ID: 392965
Print ISSN: 2631-8474
Online ISSN: 2631-8482

London Journal of Engineering Research

Volume 25 | Issue 6 | Compilation 1.0

Designing High-Dense-Packed Electronic Equipment using Three-Dimensional Printed Wiring

Efimenko A. A.

ABSTRACT

Context: Many areas of modern electronic equipment, such as medical, automotive, portable, and special-purpose electronics, place increased demands on mass and volume. These devices often have irregular volume structures for accommodating electronic components. Therefore, 3D printed circuit boards are ideal for implementing such designs, and improving their efficiency, as well as optimizing the selection of mounting types, are pressing challenges.

Objective: The aim of this work is to develop a 3D printed circuit board method that is efficient in production and use, as well as a method for objectively selecting the optimal PCB option from the existing variety when designing miniature electronic equipment.

Method: The design and manufacturing method for manufacturing rigid-flexible printed circuit boards is based on traditional PCB manufacturing methods with an appropriate addition that allows for the achievement of three-dimensional design properties.

The method for selecting a 3D printed circuit board option consists of two parts: a heuristic method and passive game theory.

Results: A design and engineering method for producing a rigid-flexible printed circuit board has been developed. Its main feature is its fabrication on a single base—a rigid printed circuit board.

A sequence of steps for implementing a heuristic method is presented, and 3D printed circuit assembly metrics and their characteristics are developed, serving as input for experts selecting the optimal option.

A method for using passive game theory to solve the same problem of selecting a 3D printed circuit board option is presented. A number of formalized metrics and coefficients have been developed for this purpose.

Conclusions: This paper addresses the problem of developing methods for creating printed circuit boards for three-dimensional printed wiring and selecting optimal electrical connection designs for electronic equipment design.

The practical value of the proposed methods lies in their ready-to-use nature.

Keywords: a three-dimensional printed wiring; flexible printed circuit boards; rigid-flexible printed circuit boards; 3D-MID; optimal use of three-dimensional printed wiring.

Author: Dr. Sc., Associate Professor, Odessa, Ukraine.

I. INTRODUCTION

Existing methods of three-dimensional printed wiring (TDPW) are technologically more complex, sometimes significantly so, than traditional rigid printed circuit boards (RPCB). Among these, rigid-flexible printed circuit boards (RFPCB) occupy a special place. These boards consist of a series of rigid PCBs connected by flexible printed circuit boards (FPCB). This design, while inherently capable of creating a three-dimensional structure and placing electronic components (EC) on the rigid parts in a manner similar to RPCBs, is more complex to design and manufacture. In the simplest case, rigid and flexible parts are manufactured separately and then combined using assembly operations. The flexible parts have the required number of conductor layers, and EC can be placed on them at a specific density, if necessary, to avoid interfering with their bending. The alignment of the conductors between the

flexible and rigid parts is subject to certain inaccuracies, which can be considered as inhomogeneities in the transmission lines, leading to signal reflection.

To improve manufacturing performance, it seems practical to fabricate RFPCB on a single rigid base, forming flexible sections after laying the conductive layers. This simplifies the design and manufacturing process for RFPCB and eliminates inhomogeneities in transmission lines when transitioning from the rigid to the flexible section and vice versa.

The selection of optimal design and technological solutions (DTS) always presents certain challenges associated with the difficulty of formalizing the selection problem and implementing optimization in purely mathematical terms. The selection of TDPW options is no exception. Currently, there are a number of TDPW methods and their modifications, each with a variety of properties, advantages, and disadvantages. The developer's task is to correctly evaluate them and select the best one to avoid redesigning the device and incurring excessive costs. In reality, there are no objective methods for solving such problems at a system level. Typically, developers' experience and the specified requirements for the products being developed are used for these purposes, which does not always allow for the correct decision-making.

II. PROBLEM STATEMENT

Modern electronic equipment (EE) and its devices are often characterized not only by their miniature size but also by the complex volumetric shape in which the electronic circuit, i.e., electronic components and associated electrical connections, must be housed. Effective use of rigid printed circuit boards with maximum volume fill factor for these purposes is highly problematic for many reasons. Therefore, design and technological solutions that minimize these problems have been implemented for quite some time. These solutions include flexible PCBs, rigid-flex PCBs and their associated assemblies, 3D-MID (three-dimensional molded interconnect device) technology, taking into account all the modifications developed to date. Each has its own characteristics and accordingly, advantages and disadvantages, which should not be considered absolute, but rather applied to the conditions in which they are used. However, their undoubted advantage, which allows for their effective use in irregularly shaped volumes, is their ability to create three-dimensional (3D) structures.

Thus, the existence of a multitude of DTS and corresponding methods for laying out electronic circuits in miniature irregular volumes, on the one hand, allows EE developers to select the most appropriate methods. On the other hand, there are no objective methods for optimally selecting specific DTS. Furthermore, changing conditions for the creation of electronic devices (ED), such as electronic components, materials, computer-aided design software, higher signal frequency ranges, etc., necessitate the need for new DTS and methods for selecting them for specific EE.

III. REVIEW OF THE LITERATURE

The design and manufacturing technology of electronic equipment and devices that meet modern miniaturization requirements and satisfy the need to integrate mechanics and electronics (mechatronics) are addressed in numerous studies and papers.

The further development of EE will largely depend on miniaturization. This involves the reduction in the size of electronic components and the use of flexible and rigid-flexible mounting bases, which allow for a significant reduction in the thickness of the structural base of electronic components and assemblies – printed circuit boards. Flexible structures, thanks to their strength, manufacturability, reduced material consumption, and other properties, are extremely diverse, and their use is only expected to increase in the future [1].

Flexible and rigid-flexible printed circuit boards are directly related to adaptive electronics. Due to their unique properties for solving problems of miniaturization, durability, and efficiency, the demand for their use will only increase in traditional areas of application and expand into

areas such as robotics, smart textiles, complex and flexible displays, and others. This, in turn, necessitates the development of more efficient, compact, and reliable solutions to shape the future of electronics [2].

Flexible printed circuit boards are a groundbreaking breakthrough in the world of electronics. One aspect of their use is the possibility of using them for volumetric 3D assembly. Here, they offer corresponding advantages due to their flexibility and the ability to create various shapes. These advantages can be summarized as follows [3]:

- Flexibility in forming any shape and size;
- Low weight;
- A large number of miniature ECs in a small area for the production of miniature EDs;
- Minimization of interboard connections due to a reduction in the number of electrical connectors and, consequently, soldered joints;
- More vibration-resistant;
- High heat resistance due to the use of a polymer such as polyimide;
- High reliability due to a reduced number of components, interconnections, and solder joints;
- Easy installation in volumes with irregular geometry and confined environments.

Disadvantages that may limit their use in certain environments should also be noted [3, 4]:

- High cost compared to rigid printed circuit boards;
- Possible reduced durability due to damage caused by excessive bending, folding, or repeated twisting;
- Difficulty in repairing if damaged;
- Limitations in the use of heavy and large ECs;
- Limited number of conductive layers;
- Problems with testing boards and assemblies based on them;
- Thin flexible circuit boards are more difficult to manufacture with the same precision as rigid printed circuit boards;
- Difficulty in automating the placement and soldering of electronic components;
- Signal integrity issues associated with the thin material thickness, and bending can cause changes in signal reflection due to changes in the impedance of the signal transmission lines.

The tradeoffs between advantages and disadvantages must be considered for optimal utilization, which can be summarized in the following statements [4]:

- The advantages of the technology outweigh the higher cost, and design optimization allows for problems to be minimized;
- Flexible printed circuit boards are most appropriate for use in electronic devices where the shape and size require the printed circuit board to conform to the device's shape while keeping the dimensions as small as possible.

Some of these disadvantages are eliminated by using rigid-flexible printed circuit boards. They also offer other positive qualities.

RFPCB are a technology that combines the best of two design solutions: the stability of RFPB and the flexibility of FPCB) [5]. Rigid-flexible printed circuit boards are designed to provide bending and flexibility in specific areas. RFPCB designs offer several advantages:

- They are space-efficient because they eliminate the need for electrical connectors as circuit components and, consequently, additional electrical connections and contacts. This, in turn, positively impacts the reliability associated with electrical connectors;
- Reduced costs for assembly and installation operations, which are again associated with the reduction or complete elimination of electrical connectors;
- Greater flexibility in complex geometries – RFPCB technologies allow the creation of complex board shapes for 3D configurations.

However, several challenges arise when designing RFPCBs compared to rigid and flexible PCBs [5]:

- More complex design rules, as different requirements for rigid and flexible PCBs must be considered simultaneously, including bend radii, layer structures, material limitations, etc.;
- Signal integrity and EMI control can be more challenging not only in bend zones, but

especially when transitioning from the flexible to the rigid part and vice versa;
- Decisions about the placement of electrical connectors, if they need to be used between flexible and rigid parts;
- Assembly, installation, testing, and repair processes can be more complex because specialized equipment and manufacturing operations may be required;
- The cost of RFPCBs is typically higher, given the complexity of the design, materials, equipment, and processes used.

Many challenges associated with the design features of RFPCBs are addressed thanks to the support for the design of rigid-flex designs in the Altium Designer computer-aided PCB design system [6].

Rigid-flexible printed circuit board technology continues to evolve and improve, eliminating shortcomings and achieving new qualities.

[7] proposes a new manufacturing process technology aimed at overcoming some of these challenges. A RFPCB implementation with two flexible and eight rigid base layers is presented to meet the functional requirements for use in space 3D electronics. It should be noted that the materials and processes used are common to the production of both rigid and flexible PCBs, as well as their integration.

The author of [8] substantiates the innovative potential of flexible and rigid-flexible printed circuit boards and examines trends in these technologies and challenges to address. First and foremost, it is necessary to utilize increasingly advanced materials to achieve better performance in high-frequency signal transmission while simultaneously considering the growing interest in environmentally friendly and biodegradable materials, as well as resistance to extreme conditions for use in the aerospace and automotive industries. These and other developments are related to the use of multilayer printed circuit boards, their further miniaturization, and issues of production automation. Challenges to address include increasing signal frequencies to several GHz, the influence of parasitic effects, electromagnetic interference, and increased attenuation.

3D-MID technology [9] occupies a special place in three-dimensional printed wiring, which has now been adequately developed for use in a wide range of areas where it makes sense to combine electronic circuits with three-dimensional mechanical parts. 3D-MID devices can be ordered from contract manufacturing companies, or it is possible to acquire the technology and organize in-house production. It should be noted that the design of such devices is supported by the new 3D-MID tool Altium Designer [10]. However, it should be noted that 3D-MID technology is not effective for all electronic devices.

A comprehensive presentation of the state of the art in 3D-MID technology for the creation of modern EDs is offered in the book [11]. It systematically presents issues related to the technology itself, the materials used, assembly operations, quality and reliability, prototyping, development, and practical examples. The importance of 3D-MID technology is significant in the automotive industry. It is also important to note the important feedback: the development of 3D-MID solutions in the automotive industry stimulates further research for the development of this technology, whose importance is also growing in medical technology, telecommunications, industrial automation, and other fields.

Current research is aimed at improving the efficiency and economic feasibility of 3D-MID technology.

The paper [12] presents a technology for manufacturing three-dimensional electronic circuits that, in terms of its design characteristics, is close to 3D-MID, and its production largely utilizes flexible printed circuit board manufacturing processes. The electronic components are connected by meander-shaped or, one might say, sinusoidal lines. These lines stretch during thermoforming, i.e., the creation of the three-dimensional shape, while maintaining the functionality of the connections. The advantage of this technology is the ability to create three-dimensional electronic circuits of

arbitrary shapes and the fact that it primarily consists of standard printed circuit board manufacturing steps. The disadvantages of this technology include limited capabilities in terms of component packing density, the use of complex equipment and low-performance laser meander structuring processes, and the significant challenges of creating two or more conductive layers.

The paper [13] addresses the technological specifics of creating 3D-MID devices. Particular attention is paid to the leading process in the technology of forming interconnections on the surface of cast parts – laser direct structuring (LDS). This technology has been proven on many compact products – sensors, mobile phones, automotive and medical devices, etc. New opportunities are presented by the innovative WeLDS technology, which uniquely combines 3D-MID technology and laser welding of LPKF plastics to create strong and reliable connections of mechanical components. Additional capabilities provided by laser welding include effective sealing and protection of 3D-MID components and increased geometric complexity of parts and functional integration.

The authors of [14], as a specific case of 3D-MID technology, explore the possibility of creating an omnidirectional inductive wireless charging system for a mobile phone, in which 3D-MID coils are used instead of flat coils on rigid printed circuit boards. The obtained results allow us to conclude that 3D-MID technology offers potential for improving the performance of charging systems not only for mobile phones, but also for powering robots, mini-robots, and devices for medical and military applications.

The bottlenecks in the development of 3D-MID technology—high cost, limited design flexibility, long production cycles, and difficulties in processing complex geometries—are to some extent mitigated by the use of additive manufacturing technology [15]. This technology does not require molding tools, offsetting the high initial cost of injection molds and providing greater design flexibility and faster production cycles. The present work utilizes stereolithography (SLA) technology, which provides higher accuracy and better material properties compared to the more common 3D-MID additive manufacturing technologies of fused deposition modeling (FDM) and selective laser sintering (SLS). Components based on SLA 3D printing technology for 3D-MID demonstrate enormous potential for further miniaturization. It should be noted that the primary goal is not the width of the communication lines (conductor traces) — at this stage, a value of 150 μm has been achieved, but the arrangement of the ECs, the use of smaller chip packages, and pre-defined circuit configurations determine the overall size of the circuit carriers.

The paper [16] examines the development of stretchable electronics and whether it will be the next stage in the evolution of wearable technologies. Unlike FPCBs, which typically bend along a single axis, stretchable electronics are structures that can be stretched, twisted, and bent while maintaining their operational properties. Considering the proposed ideas and developments, such as a deformable printed circuit board on an anisotropic conductive film that can stretch, it is possible to discuss replacing RPCBs with deformable conductive films.

This paper presents a new method for creating three-dimensional printed circuit boards and devices that improves certain performance indicators, primarily economic ones. A method is also proposed that will assist EE developers in selecting optimal DTSs for the design basis of electrical connections. A literature review confirms that this problem exists and is relevant.

Materials and Methods

To better illustrate the types of three-dimensional printed wiring described in the literature review, we provide some typical illustrations.

Fig. 1 [3] shows a electronic unit obtained by mounting an ECs on a FPCB. The flexibility of the PCB base allows it to be bent in the desired directions, shaping the cavity in which it is to be installed.

Figure 1: FPCB with installed EC – electronic unit

FPCBs can also be used solely for electrical connections, i.e., without installed ECs. Such FPCBs, as a special case, are also called flexible printed cable and are shown in Fig. 2 [3]. However, they, too, and to an even greater extent due to the absence of ECs and the consequent risk of bending affecting the integrity of contact connections, possess the properties of flexibility and impart a three-dimensional structure.

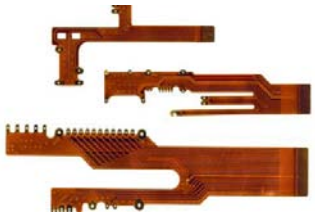

Figure 2: FPCBs – connecting cables

Figure 3 [17] shows a rigid-flexible printed circuit board assembly formed by rigid and flexible printed circuit boards with installed ECs. This example provides flexibility in the relative positioning of the RPCBs, as well as flexibility in external connection of the assembly to other devices.

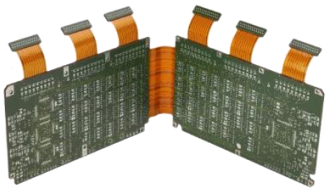

Figure 3: Rigid-flexible printed circuit unit

One of the design and technological solutions for creating a RFPCB is presented in the diagram in Fig. 4 [7].

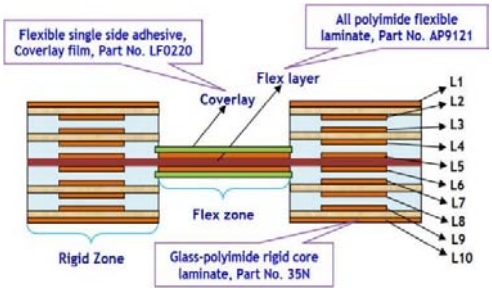

Figure 4: Schematic diagram of the arrangement of various layers in the RFPCB

RFPCB consists of two rigid zones and one flex zone connecting the rigid zones. Common to all zones is the flex layer, an all polyimide flexible laminate. The flexible zone also includes two conductive layers and flexible cover layers (coverlay), which are flexible single side adhesive, coverlay films on the outer layers. The rigid zones, in addition to the common flexible zone, consist of conductive layers L2 – L9 and outer layers L1, L10 of glass-polyimide rigid core laminate.

Fig. 5 [10] shows a 3D-MID mechatronic unit demonstrating the adaptation of electrical connections and installed ECs to the complex three-dimensional shape of a mechanical part.

Figure 5: 3D-MID mechatronic unit

One of the most attractive industries where the efficiency of using 3D-MID technologies is very high is medical technology. Fig. 6 [10] demonstrates some of these devices: elements of a hearing aid, dental equipment, and an antenna in a capsule.

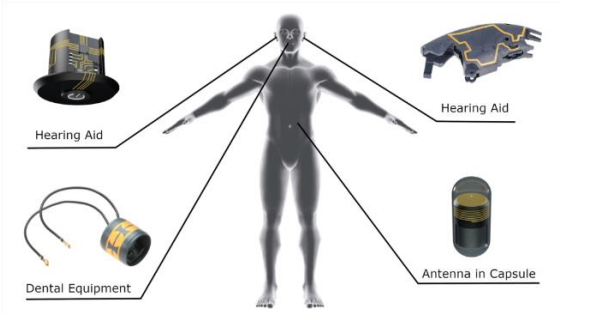

Figure 6: Use of 3D-MID devices in medicine

The use of FPCB-based technology for arbitrary-shaped devices is illustrated in Fig. 7 [12].

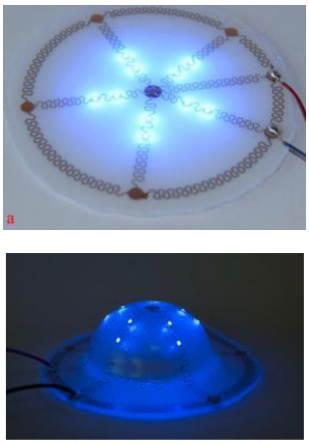

a

b

a – flat form before thermoforming;

b – 3D shape after thermoforming

Figure 7: Stages of manufacturing a lamp

The literature review materials and the preceding illustrations serve as the starting point for solving the previously stated problems: creating a cost-effective method for designing 3D printed circuit boards and devices, and a method that will assist electronic equipment designers in selecting optimal DTS for TDPWs.

The solution to the first problem is based on the assertion that RPCBs are the most widely used in production, attractive to electronic equipment designers, reliable, with a variety of design options, and therefore cost-effective. However, they do not fully possess the properties of TDPWs. Further research is devoted to imparting such properties.

The solution to the second problem is determined by the difficulties in formalizing the properties and quality indicators of the considered types of 3D printed connections and, accordingly, the possibility of using purely mathematical optimization methods. For this reason, it is proposed to use a heuristic method and passive game theory, adapted for solving design problems in [18] and [19], to select the optimal design for printed 3D electrical connections and EC assembly.

A method for creating a rigid-flexible printed circuit board: This design and manufacturing method is intended for creating printed circuit boards and, correspondingly, printed circuit assemblies that have a rigid-flexible three-dimensional structure for the placement and connection of ECs. It is suitable for electronic devices with limited volume and irregular structure to improve the layout characteristics of the equipment through more efficient use of the complex shape of the EE [20, 21].

The main driver for developing the proposed method was the economic component associated with the use of more complex technological processes in modern 3D printed circuit assembly methods compared to RPCB manufacturing technology, and the need to acquire new technological equipment, which in some cases is quite complex and expensive.

The objective of the study was to create a printed circuit board and unit based on a RPCB that fully exhibits the properties of a TDPW, i.e., can accommodate two or more rigid parts and a corresponding number of flexible parts for electrical and mechanical connection of the rigid parts and the creation of a 3D structure without the use of assembly and mounting operations; increase the packaging density in the irregular structure of an electronic device; reduce the cost of manufacturing printed circuit boards and the corresponding printed circuit assemblies and create conditions for maintaining signal integrity.

The proposed method is implemented as follows. Initially, a RPCB is manufactured using known technologies for single-sided, double-sided, multilayer, or other boards, taking into account

that the board's contour, both external and internal, must correspond to the 3D printed circuit unit. The flexibility of such a board is ensured by creating grooves on its surface in the bending direction of individual board sections. These grooves are deep enough to convert these sections from rigid to flexible. Subsequent assembly of the ECs is performed in a single process cycle on all rigid sections of the PCB separated by grooves. Bending the PCB sections at specific angles and directions allows for the creation of a 3D rigid-flexible printed circuit unit corresponding to the shape and dimensions of the electronic device where it will be installed.

The essence of the method is explained by the figures. Fig. 8 shows a RPCB with grooves 2.1 – 2.3. This creates flexible sections of the board between rigid sections 1.1 – 1.4, allowing sections 1.2–1.4 to be bent along lines 4.1 –4.3 at specific angles, creating a three-dimensional rigid-flexible structure. To ensure design flexibility, the groove depth must be such that dimension t is no greater than the combined thickness of the foil conductors and the adhesive used to bond them to the dielectric base of the RPCB.

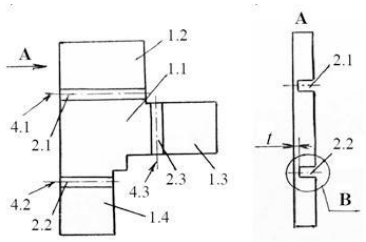

a b

a — front view;
b — side view

Figure 8: Flexible sections 2.1 – 2.3

The printed circuit board and the corresponding 3D printed circuit unit are manufactured and used as follows. A flat, rigid printed circuit board (Fig. 8) is manufactured using established technologies. Its contour must match the installation object and subsequent 3D structure formation. To achieve this, grooves 2.1 – 2.3 are created in the board, for example, by milling, at the locations and directions of their subsequent bending 4.1 – 4.3.

In this state, the printed circuit board undergoes electrical installation, i.e., installation of EC 3 and other components, for example for external connection, transforming it into a printed circuit unit (Fig. 9, a).

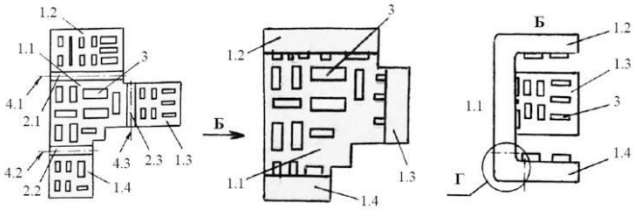

a b c

a -after installing ECs, b, c — front view and side view, respectively after bending individual parts

Figure 9: The printed circuit unit after installing ECs

By further bending individual sections 1.2 – 1.4 along directions 4.1 – 4.3 at specific angles, the flat printed circuit unit is transformed into a three-dimensional structure, the dimensions and shape of which correspond to the installation object (Fig. 9, b, c).

To strengthen the structure in the flexible sections, polyimide film 6.1, 6.2 can be applied, for example, to foil conductors 5, on both sides and to the walls of grooves 2.1–2.3 (Fig. 10, a).

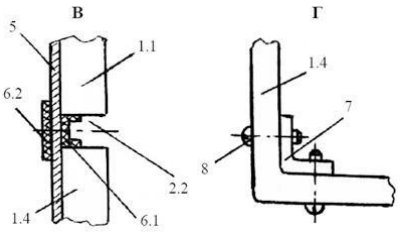

a b

a - flexible part, b - rigid parts

Figure 10: Mechanical reinforcement of parts of a printed circuit board to each other

If additional fixation of individual rigid parts 1.1 – 1.4 is required, fastening elements 7, 8 (Fig. 10, b) can be used.

Thus, a 3D printed circuit unit based on a RFPCB can be installed in electronic devices of various structures, which is especially relevant for devices with complex shapes and limited volume. The

proposed method does not claim to be universal, but in some cases it can be used as a more efficient approach.

Method for selecting a three-dimensional printed wiring: As mentioned above, two approaches are proposed as the basis for developing the method: using a heuristic method and the theory of passive games [18] and [19] (Fig. 11).

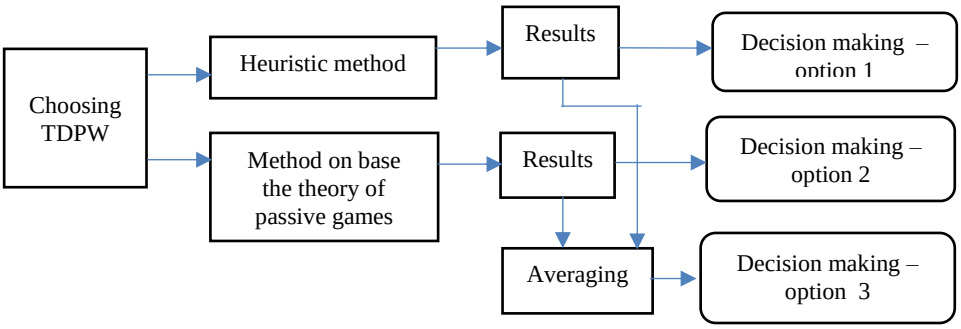

Figure 11: Sequence of selection of TDPW

Each of these approaches has its advantages and disadvantages. The first is less expensive and more efficient, but is somewhat subjective. The second, conversely, is more expensive to calculate indicators, but minimizes subjectivity in determining selection results. However, both require the use of weighting factors that take into account the capabilities and conditions of application of various types of TDPW, and their definition is rarely formalized. This also introduces a certain degree of error into the selection results. The decision to use a method is made on a case-by-case basis. Alternatively, both approaches can be used simultaneously and the results averaged.

The implementation of the first approach is based on the heuristic method described in [18]. A prerequisite for the experts' work is their competence in the given area of knowledge, as well as a number of initial data related to the specific development:

- A description of the task and challenges of creating an electrical connection design (ECD), determining the feasibility of using varieties of TDPW for this purpose;
- Possible layout diagrams of the electronic device being developed;
- Questionnaires for evaluating the proposed TDPW types;
- A description of the expert voting conditions;
- Determination of the ranges of possible expert assessment values in points from the minimum x_{min} , y_{min} to the maximum x_{max}, y_{max} respectively, for two groups of experts or two rounds of voting.

As initial data for experts to complete the questionnaire, it is proposed to use information with the classification and comparative characteristics of TDPW methods, presented in Table 1. These data can be considered an integral part of the method, as they can be used over a relatively long period of time, updated as new data emerges or as otherwise necessary. They are intended for use by experts when completing questionnaires.

Table 1: A three-dimensional printed wiring indicators and their characteristics

Indicator	The degree of implementation of TDPW methods			
	FPCB	RFPCB	RFPCB on a single base	3D-MID
1. PCB type: • Single-sided; • Double-sided; • Multi-layer	 Yes Yes Yes	 Yes Yes Yes	 Yes Yes Yes	 Yes No No
2. ECs: • surface-mounted; • through-hole; • embedded in the board body; • heavy and bulky	 Yes No No No	 Yes Yes Yes Yes	 Yes Yes Yes Yes	 Yes No No Yes
3. Adaptation to the body shape	High	High	Average	Very high
4. Density of ECs installation	Low	High	High	Low
5. Possibility of creating complex 3D shapes	High	High	Low	Very high
6. Accuracy of installation of ECs relative to the body	High	Average	High	Very high
7. Set of construction materials	Small	Large	Small	Very large
8. Weight ECD	Small	High	High	Very small
9. Heat resistance	High	Low	Low	Low
10. Signal integrity issues	No significant	Significant	Minimal	No significant
11. Difficulty of repair	Increased	High	Low	Very high
12. Problems with testing boards and units	Significant	Significant	Minimal	Significant
13. Potential reduction in durability due to excessive flexing	Significant	Significant	Not significant	No
14. Continuity of the RPCB technology	High	High	Very high	Very low
15. Complexity of technology	Not high	High	Not high	Very high
16. Comparative cost	Average	High	Low	Very high

The subjective factor of this method is overcome by developing and maintaining information data that classifies and characterizes the set of selected technical solutions inherent to certain DTSs, such as the RFPCB. The influence of the subjective factor is mitigated by the use of various statistical tests: the correlation coefficient, the Fisher test for equality of variances, and the Student's t-test. Automation of the selection process facilitates the practical application of the method. An example of the use of the proposed method is provided in the next section.

The implementation of the second approach involves the use of a number of TDPW indicators that have a mathematical representation [19]:

- The indicator of the specific mean time between failures of a connection – represents the time between failures of one connection, characteristic of a certain type of TDPW

$$t_{sp} = \frac{1}{(\sum_{i=1}^{n} \lambda_i + \sum_{j=1}^{d} \lambda_j)} / n, \quad (1)$$

where λ_i – failure rate of the i-th connection;

λ_j – failure rate of the j-th contact;

n – number of connections in the design TDPW;

d – number of contacts in the design TDPW;

- Indicator of the reduced delay time of information transmission

$$\tau_d = \sum_{i=1}^{n} \tau_i / \sum_{i=1}^{n} l_i, \quad (2)$$

where τ_i – signal delay in the i-th connection of the information transmission path;

l_i – length of the i-th connection;

- Automation factor for electrical connections

$$K_a = n_a / n, \quad (3)$$

where n_a – number of connections performed by automated methods.

In this case, this coefficient should be understood not only as connections on the boards, but also as connections on the boards inside the electronic module.

Additionally, it is proposed to use TDPW-specific indicators:

- Automation coefficient for mounting ECs on boards

$$K_{aec} = \frac{n_{aec}}{n_{ec}}, \quad (4)$$

where n_{aec} – the number of ECs that are installed using automated methods; n_{ec} – total number of installed ECs;

- Coefficient of the volume of the TDPW design

$$K_v = \frac{V_{com}}{V_{em}}, \quad (5)$$

where V_{com} – volume occupied by the TDPW design; V_{em} – volume of the electronic module;

- Coefficient of the weight of the TDPW design

$$K_m = \frac{m_{com}}{m_{em}}, \quad (6)$$

where m_{com} – weight of the TDPW design;

m_{em} – weight of the electronic module;

- Signal reflection coefficient in transmission line inhomogeneities

$$K_{ref} = \frac{S_{ref}}{S_{tr}}, \quad (7)$$

where S_{ref} – reflected signal amplitude;

S_{tr} – amplitude of the transmitted signal;

- Mounting space utilization coefficient; characterizes the reduction in volume of the electronic device body where the electronic circuit is placed using one of the TDPW methods, compared to rigid printed wiring

$$K_{isl} = 1 - \frac{V_{thd}}{V_{twd}}, \quad (8)$$

where V_{thd}, V_{twd} – the volume required for the placement of an electronic circuit using, respectively, a TDPW and a two-dimensional rigid printed circuit board;

- Indicator of adaptation of TDPW types to the shape of the body of the ED being developed

$$A_{\text{thd}} = \frac{n_{thd}}{N}, \quad (9)$$

where N – the number of body shapes available and suitable for placement electronic circuits; n_{thd} – the number of body shapes possible for the implementation of a specific type of TDPW.

The following body shapes can be used: cube, parallelepiped, cylinder, sphere, hemisphere, cone, truncated cone and others, as well as their combination in one design;

- TDPW flexibility indicator

$$I_f = \frac{n_{b\max}}{r_{\min}}, \quad (10)$$

where $n_{b\max}$ – the maximum permissible number of bends in the structure (for example, at an angle of 180°); $r_{\min}$ – minimum bending radius (for example in mm).

Having calculated the given coefficients and indicators, we can determine the optimal variant of the TDPW the electronic device being developed, using the theory of passive games [19]. An example of the method's use is given in the next section.

IV. EXPERIMENTS

Testing the practical feasibility of the RFPCB manufacturing method: The above-described technological processes for RFPCB manufacturing were experimentally performed to confirm their feasibility. The basis for the experiments were two blanks made of single-sided foil-clad fiberglass, one with a continuous foil layer, and the other with foil tracks.

One of the most critical processes is the production of grooves for flexible sections. High precision machining is required, as mentioned earlier, for example, by milling. The challenge lies in precisely removing the foil or foil traces from the fiberglass laminate, and preferably from the adhesive, without damaging these conductive elements. Chemical etching can replace mechanical machining. However, the fiberglass laminate must be etched to a sufficiently deep depth. A combination of these two methods—preliminary high-speed machining without precision and chemical etching of a small remaining portion of the fiberglass laminate without the risk of damaging the foil conductive traces - can yield good results.

The second issue regarding the production of grooves, i.e., flexible parts, is determining their width. It depends on the bend radius, the thickness of the rigid part of the PCB, the angle of rotation of the rigid parts relative to each other, and other characteristic dimensions of the RFPCB. Let's consider this using the example in Fig. 12, which contains the initial data for the calculation regarding the two most typical cases, taking into account the assumption that the bending radius of the flexible part r is equal to the thickness of the rigid part t.

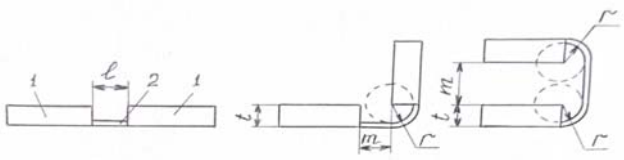

a b c

a - a workpiece; b - at a bending angle of 90° ;c - at a bending angle 180°: 1 – rigid part; 2 – flexible part

Figure 12: Determining the groove width on a workpiece

1. The bending angle of the rigid parts is 90°. The groove width l is determined using the following relationship

$$l = \frac{1}{4}2\pi t + m = \frac{1}{2}\pi t + m. \quad (11)$$

At m = 0, i.e. when the rigid parts are located in close proximity, the minimum groove width is

$$l_{\min} = \frac{1}{2}\pi t. \quad (12)$$

2. For the case of bending rigid parts by 180°

$$l = 2(\frac{1}{2}\pi t) + m = \pi t + m, \quad (13)$$

$$l_{\min} = \pi t. \quad (14)$$

Fig. 13 shows photographs of printed circuit boards with grooves made.

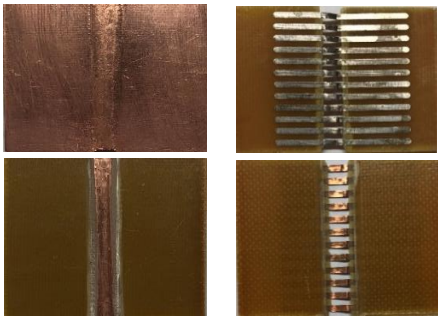

a b

Figure 13: Printed circuit boards with grooves: a – with a continuous foil layer; b – with foil tracks

Each version contains two images: the top one is from the foil side, the bottom one is from the fiberglass side and the grooves are made.

To increase the reliability of the flexible part, it must be made similar to the FPCB, i.e., a polyimide layer must be applied to one or both sides using a polyimide varnish. After this, the flexible part will be identical to the FPCB in its mechanical and electrical characteristics.

Fig. 14 shows photographs of the PCB with polyimide layers applied to both sides.

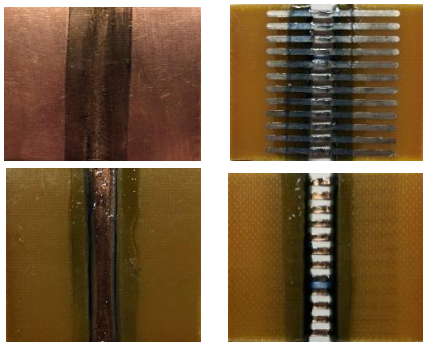

a b

a – with a continuous foil layer; b – with foil tracks

Figure 14: Printed circuit boards that meet the properties of the RFPCB:

On such RFPCBs it is possible to install ECs and other elements and give them a three-dimensional shape, which is demonstrated in Fig. 15, but only without ECs.

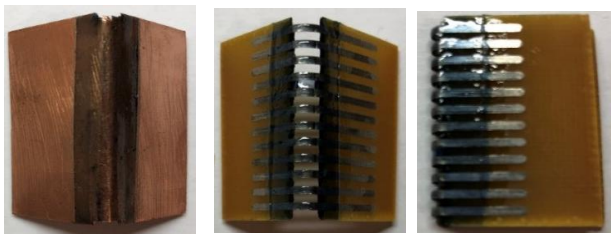

a b c

a – with a continuous foil layer and a 90° turn;
b – with foil tracks and a 90° turn;
c – with foil tracks and a 180° turn

Figure 15: RFPCBs converted to volumetric form

Selecting a three-dimensional printed wiring using a heuristic method: We will examine the use of this method using an example created according to the algorithm (Fig. 1)[18].

1. Initial data for completing the questionnaires:

- Select the type of TDPW to create an electronic module to be embedded in a given volume, for example, a medical device, a sketch of which is attached. A schematic diagram of the module and a list of electronic components are also provided. A distinctive feature of the volume allocated for the module is its irregular structure – a combination of a parallelepiped and a truncated cylinder. It is assumed that the printed circuit usit for this electronic module will be manufactured by contract manufacturing, and pre-production preparation with the purchase of new equipment is not necessary. Important factors for selecting the optimal option include manufacturing cost and reliability indicators;
- Quantitative data should include module dimensions and dissipated thermal power;
- Questionnaire forms;
- Voting conditions: two expert groups, each consisting of 5 people;
- The range of possible expert assessment scores: from 0 to 10 inclusive for both groups;
- A description of the TDPW indicators and their characteristics (Table 1).

2. Completion of questionnaires by experts. There should be as many questionnaire forms as there are experts involved, in this case – 10. The questionnaire form and an example of its completion are provided in Table 2. For a more objective assessment of the TDPW options and the assignment of points, we use the indicators and the degree of their implementation (Table 1). Regarding [18], this corresponds to the modified algorithm.

Table 2

Indicator	Points awarded for types of TDPW				Weighting factor, q_j
	FPCB	RFPCB	RFPCB on a single base	3D-MID	
1. PCB type: - single-sided; - double-sided; - multi-layer	 10 10 10	 10 10 10	 10 10 10	 10 2 0	0,1
2. ECs: - surface-mounted; - through-hole; - embedded in the board body; - heavy and bulky	 10 0 0 0	 10 10 10 10	 10 10 10 10	 10 0 0 10	0,08
3. Adaptation to the body shape	8	6	5	10	0,12
4. Density of ECs installation	6	10	10	5	0,1

5. Possibility of creating complex 3D shapes	8	6	5	10	0,11
6. Accuracy of installation of ECs relative to the body	8	6	8	10	0,04
7. Set of construction materials	10	8	10	5	0,06
8. Weight ECD	10	6	6	10	0,03
9. Heat resistance	10	6	6	5	0,04
10. Signal integrity issues	8	5	10	8	0,06
11. Difficulty of repair	8	6	10	4	0,03
12. Problems with testing boards and units	5	5	10	8	0,02
13. Potential reduction in durability due to excessive flexing	6	6	8	10	0,03
14. Continuity of the RPCB technology	8	6	10	2	0,05
15. Complexity of technology	10	7	10	4	0,05
16. Comparative cost	8	6	10	3	0,08
$\sum_{i=1}^{16} a_i q_j$	9,6	7,2	8,4	6,4	$\sum_{j=1}^{16} q_j = 1$

The use of weighting factors q_j eliminates the possibility of overcompensation between indicators and improves the reliability of selecting the optimal type TDPW. These factors are assigned by each expert, and the sum of these factors must equal one.

Indicators can be characterized by several components. In this example, these are indicators 1 and 2. In this case, the average value of indicator is calculated $a_{ip} = \sum_{i=1}^{n} \frac{a_i}{n}$.

The last row in the table represents the sum of the products of the assigned points by the weighting factor for each installation type and is the expert's final result. All experts in groups X and Y must complete the tables in a similar manner. The resulting expert data is summarized in Table 3 to convolve the indicators (the table format is given in [18]).

Table 3

Type of TDPW	x_1	x_2	x_3	x_4	x_5	$\sum_{i=1}^{5} x_i$	y_1	y_2	y_3	y_4	y_5	$\sum_{i=1}^{5} y_i$	$\sum_{i=1}^{5} x_i + \sum_{i=1}^{5} y_i$
1. FPCB	9,6	8,5	9,2	7,8	7,1	42,2	6,8	9,5	8,8	7,8	8,2	41,1	83,3
2. RFPCB	7,2	6,8	6,9	6,3	6,8	34,0	5,7	8,1	7,3	6,4	7,3	34,8	68,8
3. RFPCB on a single base	8,4	7,6	8,1	6,7	6,5	37,3	6,1	8,3	7,7	6,9	7,5	36,5	73,8
4. 3D-MID	6,4	5,7	6,6	6,5	6,2	31,4	5,2	7,1	6,9	6,2	6,7	32,1	63,5

As a result of processing the data in the table, the best installation is the one using the FPCB.

3. Determining the consistency of expert assessments based on the value of the correlation coefficient [18]

$$r(x,y) = K(x,y)/\sqrt{D_x D_y},$$

where

$$K(x,y) = \frac{\sum_{i=1}^{5}(x_i - m_x)(y_i - m_y)}{N-1} = \frac{7,56}{5-1} = 1,89;$$

$$D_x = 5,24;\quad D_y = 5,37;\quad \sqrt{D_x D_y} = 5,31;\quad r(x,y) = 0,36$$

Based on this, it can be considered that the agreement between the experts' assessments is satisfactory.

4. Assessing the equality of dispersion using Fisher's test. We calculate the value of $F = D_y / D_x = 1.025$ and compare it with the table F_T (table П.6 of appendix [22]). For the degree of freedom $m_{c.c} = N - 1 = 4$ and the chosen significance $\alpha = 0,05$, F_T = 6.39, which is greater than F, indicating that the experts' opinions are homogeneous.

5. Testing the hypothesis of equality of average values using Student's t-test:

- The Student's t-test is determined

$$t = \frac{m_x - m_y}{\sqrt{D}},$$

where

$$D = \frac{(m_x - 1)D_x + (m_y - 1)D_y}{N(N-1)} = \frac{(7,3-1)5,24 + (7,2-1)5,37}{5(5-1)} = 3,32,$$

$$t = \frac{7,3 - 7,2}{\sqrt{3,32}} = 0,055;$$

- The degree of freedom is calculated $m_{c.c} = 2N - 2 = 10 - 2 = 8;$
- In table П.4 of appendix [22], in the row corresponding to $m_{c.c}$ = 8, the t value closest to the calculated value is selected; this is t = 0.265. This corresponds to a value of $P_s(t)$ = 0.8;
- The significance level is determined $\alpha = 1 - P_s(t) = 0,2;$
- The condition $\alpha/2 < P_s(t) < 1 - \alpha/2$ is checked: 0.1 < 0.8 < 0.9.

This condition is met, thus confirming the hypothesis of equality of average values.

Thus, for the example under consideration, the type of TDPW defined in table 3 can be adopted – this is montage using a FPCB.

If these statistical tests did not satisfy the specified significance levels, then a re-vote would be necessary, changing the composition and/or number of experts in the groups.

Selecting a three-dimensional printed wiring using passive game theory. The initial data for this method are the indicators taken from [19] – (1) – (3) and those proposed in this paper – (4) – (10).

We calculate the values of these indicators and summarize them in Table 4.

Table 4

Type of TDPW	Values of the Indicators									
	t_{sp}, ч (K_1)	τ_d, с/м (K_2)	K_a (K_3)	K_{aec} (K_4)	K_v (K_5)	K_m (K_6)	K_{ref} (K_7)	K_{isl} (K_8)	A_{thd} (K_9)	I_f, 1/мм (K_{10})
1. FPCB (Y_1)	$7 \cdot 10^9$	$4 \cdot 10^{-6}$	0,9	0,9	0,05	0,1	0,1	0,8	0,7	10^3
2. RFPCB (Y_2)	$5 \cdot 10^9$	$6 \cdot 10^{-6}$	0,8	0,8	0,25	0,4	0,3	0,5	0,4	10^3
3. RFPCB on a single base (Y_3)	$6 \cdot 10^9$	$5 \cdot 10^{-6}$	0,8	0,9	0,2	0,3	0,1	0,5	0,4	$5 \cdot 10^2$
4. 3D-MID (Y_4)	$3 \cdot 10^9$	$7 \cdot 10^{-6}$	1,0	0,7	0,01	0,02	0,1	0,9	1,0	-

To facilitate subsequent processing of the results, the table provides additional designations for the TDPW types (Y_1) – (Y_4) and indicator values (K_1) – (K_{10}).

To convolution the partial quality indicators, it is necessary to perform a number of operations related to the following:

- Some of them are maximized, i.e., the higher the indicator, the better, while others are minimized, i.e., the lower the indicator value, the better;
- The partial indicators are different in physical nature, dimensionless, and, as a rule, differ significantly in magnitude;
- The partial indicators have different effects on the integral quality indicator, which is used to determine the optimal TDPW type.

Based on the above, the following steps must be taken:

- Divide the matrix (table 4) into two: one with the maximized quality indicators: (K_1), (K_3), (K_4), (K_8), (K_9), (K_{10}) and the other with the minimized indicators: (K_2), (K_5), (K_6), (K_7);
- Normalize the quality indicator values using the ratio

$$\Pi_{ijн} = \Pi_{ij} / \max \Pi_j ,$$

where $\max \Pi_j$ is the maximum value of the j-th quality indicator, i.e., the maximum value in each column;

- Determine the weighting coefficients K_w using expert analysis and multiply the partial indicators by them.

Let's create game matrices whose rows Yi correspond to the types of TDPW, and columns Kj correspond to the partial quality indicators, the calculated values of which Πij (Table 4) are entered into the cells of the matrices: table 5 – with the maximized indicators, and Table 6 – with the minimized indicators.

Table 5

Type of TDPW	Values of the Indicators					
	K_1	K_3	K_4	K_8	K_9	K_{10}
Y_1	$700 \cdot 10^7$	0,9	0,9	0,8	0,7	10^3
Y_2	$500 \cdot 10^7$	0,8	0,8	0,5	0,4	10^3
Y_3	$600 \cdot 10^7$	0,8	0,9	0,5	0,4	$5 \cdot 10^2$
Y_4	$300 \cdot 10^7$	1,0	0,7	0,9	1,0	-
$\max \Pi_j$	$700 \cdot 10^7$	1,0	0,9	0,9	1,0	10^3
K_{wj}, $(\sum_{j=1}^{6} K_{wj} = 1)$	0,2	0,15	0,15	0,25	0,15	0,1

Table 6

Type of TDPW	Values of the Indicators			
	K_2	K_5	K_6	K_7
Y_1	$4 \cdot 10^{-6}$	0,05	0,1	0,1
Y_2	$6 \cdot 10^{-6}$	0,25	0,4	0,3
Y_3	$5 \cdot 10^{-6}$	0,2	0,3	0,1
Y_4	$7 \cdot 10^{-6}$	0,01	0,02	0,1
$\max \Pi_j$	$7 \cdot 10^{-6}$	0,25	0,4	0,3
K_{wj}, $(\sum_{j=1}^{4} K_{wj} = 1)$	0,1	0,4	0,2	0,3

As a result of normalization and multiplication by the weighting coefficient, we obtain normalized weighted matrices: Table 7 – with the indicators that are maximized, and Table 8 – with the indicators that are minimized. Here we also perform the convolution of the indicator values.

Table 7

Type of TDPW	Values of the Indicators						Convolution $\sum_{j=1}^{6} \Pi^{*}_{\max ijn}$
	K_1	K_3	K_4	K_8	K_9	K_{10}	
Y_1	0,2	0,135	0,15	0,225	0,105	0,1	0,915
Y_2	0,14	0,12	0,135	0,14	0,06	0,1	0,695
Y_3	0,17	0,12	0,15	0,14	0,06	0,05	0,69
Y_4	0,08	0,15	0,12	0,25	0,15	-	0,75

Table 8

Type of TDPW	Values of the Indicators				Convolution $\sum_{j=1}^{4} \Pi^{*}_{\min ijn}$
	K_2	K_5	K_6	K_7	
Y_1	0,057	0,08	0,05	0,1	0,287
Y_2	0,086	0,4	0,2	0,3	0,986
Y_3	0,071	0,32	0,15	0,1	0,641
Y_4	0,1	0,016	0,01	0,1	0,226

To determine the optimal variant of the TDPW among those considered, we will perform a convolution of the total values of the maximized and minimized values of the quality indicators for each type of TDPW in the form of a private

$$Y_{opt} = \max\left(\sum_{j=1}^{6} \Pi^{*}_{\max ijn} / \sum_{j=1}^{4} \Pi^{*}_{\min ijn}\right).$$

We obtain the following Y values for the TDPW types: FPCB = 3.188; RFPCB = 0.705; RFPCB (on a single base) = 1.076; 3D-MID = 3.319.

In this case, the optimal solution would be to use 3D-MID technology to create an electronic module using TDPW.

The obtained results cannot be taken as estimates, as the values of the individual indicators were assigned without taking into account the actual initial data and corresponding calculations. The purpose of the provided examples is to demonstrate the practical application of the proposed methods.

V. RESULTS

The result of this work is the development of a design and manufacturing method for rigid-flexible printed circuit boards and methods for selecting a three-dimensional printed wiring using a heuristic approach and passive game theory. These methods, while seemingly completely different in their focus, are in fact united by the common goal of creating an optimal design for electronic modules using TDPWs.

A design for a rigid-flex printed circuit board and some manufacturing process features are proposed and described. The main feature of this board is that it is manufactured on a single base—a rigid PCB—for both the rigid and flexible sections. Its manufacturing processes are essentially the same as those used for traditional RPBs and share significant similarities. Experiments were conducted to fabricate RFPBs on a single base, revealing some of the design and manufacturing features and confirming the feasibility of creating 3D printed circuit design and their industrial production.

A sequence of steps for implementing a heuristic method is presented. TDPW indicators and their

characteristics are developed, which serve as initial data for experts selecting the optimal TDPW option. The practical application of the method is demonstrated through an example, which also includes statistical verification of expert data to eliminate subjectivity in their testimony. This example demonstrates the feasibility of its rapid implementation, especially if the processing of expert indicators is automated.

A method for using passive game theory to solve the problem of selecting an TDPW option is presented. A series of formalized indicators, supplemented by indicators from [19], have been developed for this purpose. The given example of TDPW selection clearly demonstrates its application, which, with appropriate automation, also presents no significant difficulties. However, it should be noted that determining the initial data for calculating the indicators is quite labor-intensive. However, this, in turn, is rewarded with more accurate results, as they are less susceptible to the influence of subjective factors.

If it is necessary to obtain the most reliable results possible, it is recommended to use both methods to solve the same problem, and determine the final result by averaging or other approaches.

VI. DISCUSSION

The results obtained regarding the design and manufacturing method for the single-base RFPCB allow us to discuss its practical application. A study of its characteristics revealed its competitiveness compared to other types of TDPW. This is all against the backdrop of its design simplicity, technological continuity, and the cost-effectiveness of production and manufacturing development. This should be complemented by the originality of the adopted solutions, which were confirmed by the priority and formal review process in the application for the proposed invention [20].

The choice of technical solutions under conditions of uncertainty and risk plays an important role in new developments, as suboptimal solutions to the assigned problems lead to suboptimal results and, in many cases, to the reworking of the work performed. Therefore, the importance of making the right decisions is undeniable, but, on the other hand, methods for obtaining reliable results and ease of use are needed. There is a considerable amount of theoretical research in this area, but there is a lack of developments with a systematic approach and, consequently, methods that would describe the practical implementation of the selection of design and technological solution in the early stages of design.

In this regard, the research conducted and the results obtained in this paper will, to a certain extent, fill the existing gap and provide developers with a tool for the correct selection of DTS. A distinctive feature of the proposed methods is their applicability in a variety of settings. The heuristic method allows for quick and cost-effective implementation, but is somewhat subjective. The method using passive game theory is largely free of subjective decisions, but requires more effort for optimization. The choice of the appropriate method is left to users, taking into account their specific circumstances. For particularly challenging developments, it is possible to use both methods to solve a specific problem and make a final decision.

VII. CONCLUSIONS

This paper addresses the problem of developing methods for creating printed circuit boards for three-dimensional printed wiring and selecting optimal electrical connection designs for them during the design of EE. The novelty of the obtained results lies in the following:

1. A design and manufacturing method for creating RFPCB has been further developed. This method utilizes a single blank to produce both rigid and flexible components. This method eliminates the need to manufacture separate rigid-flexible PCB components from different materials and perform assembly operations to connect these components. This improves the productivity and efficiency of RFPCB manufacturing and their associated printed circuit units, enhances their layout characteristics, and eliminates the potential

loss of signal integrity when transitioning from a rigid to a flexible component and vice versa.

2. A heuristic method and a method based on passive game theory for selecting the optimal DTS option for TDPW have been further developed. To this end, a set of metrics for assessing the degree of TDPW implementation has been proposed. A number of formal indicators and coefficients for assessing the types of TDPW have also been developed.

The practical value of the proposed methods lies in their readiness for use, as demonstrated by the production of RFPCB samples and calculation examples.

Prospects for further research. Regarding methods for selecting TDPW types, in order to improve reliability and simplify use, it is advisable to continue research on the following issues:

1. Detailing TDPW indicators and their characteristics to simplify the work of experts and overcome subjectivity.
2. Increasing the number of formal indicators and coefficients and developing initial data for their calculation.
3. Creating software and databases to automate calculations.
4. Expanding the range of TDPW types and their modifications for consideration for potential use.

ACKNOWLEDGEMENTS

The author expresses gratitude to her wife, Efimenko Nina I. for her support during the writing of this manuscript.

Abbreviations

PCB is a printed circuit board;

TDPW is a three-dimensional printed wiring;

RPCB is a rigid printed circuit board;

RFPCB is a rigid-flexible printed circuit board;

FPCB is a flexible printed circuit board;

EC is a electronic component;

DTS is a design and technological solution;

EE is a electronic equipment;

ED is a electronic device;

3D is a three-dimensional;

3D-MID is a three dimensional molded interconnect device;

ECD is a electrical connection design.

Nomenclature

t_{sp} is a indicator of the specific mean time between failures of a connection;

τ_d is a indicator of the reduced delay time of information transmission;

K_a is a automation factor for electrical connections;

K_{aec} is a automation coefficient for mounting ECs on boards;

K_v is a coefficient of the volume of the TDPW design;

K_m is a coefficient of the weight of the TDPW design;

K_{ref} is a signal reflection coefficient in transmission line inhomogeneities;

K_{isl} is a mounting space utilization coefficient;

A_{thd} is a indicator of adaptation of TDPW types to the shape of the body of the ED;

I_f is a TDPW flexibility indicator;

l is a groove width on the PCB workpiece.

REFERENCES

1. Ovcharenko V.E., Efimenko A.A., Tokareva E.V., Chalaja E.V. [Prospects for the use of flexible and flexible-rigid structures in electronic equipment] Technology of instrument making, 2016, no. 3, pp. 22 - 24. (Rus)
2. Azizi Othman [The rise of flexible and rigid-flex PCBs] Asia electronic university, January 2022/researchgate.net/publication/385493718_The_Rise_of_Flexible_and_Rigid_Flex_PCBs.
3. [Introduction to flex PCBs: the basics and benefits]/viasion.com/blog/introduction-to-flex-pcbs.
4. [What are flexible PCBs, and how are they manufactured?]/ansys.com/simulation-topics/what-are-flexible-pcbs.

5. Tara Dunn [Rigid-flex PCBs: advantages and challenges], 2024/resources.altium.com/ru/p/rigid-flex-pcbs-advantages-and-challenges.
6. Ben Jordan [Rigid-flex support in Altium Designer], 2024/resources.altium.com/ru/p/support-rigfid-flex-altium-designer.
7. Henumanth C., Amrendra Pratap Singh, Selvi R. et al. [Materials and manufacturing technology for high reliability rigid-flex multilayer PCB for space 3D-electronics packaging]. Engineering research express, may 2024, no.6(2)/researchgate.net/publication/380119867_Materials_and_manufacturing_technology_for_high_reliability_rigid-flex_multilayer_PCB_for_space_3D_electronics_packaging. DOI:10.1088/2631-8695/ad43b7
8. Krzyszt of Niedzwiedz [Flexible PCBs and rigid-flex circuits: key trends defining the future of this technology, 2024] /intechhouse.com/blog/flexible-pcbs-and-rigid-flex-circuits-key-trends-defining-the-future-of-this-technology/.
9. Nisan A. [Eight trends that will change electronics]. Surface mounting, 2011, no. 1, pp. 12-15. (Rus)
10. [3D-MID future manufacturing]/https://3d-circuits.com/en/3d-mid/#section.
11. Franke J. [Three-dimensional molded interconnect devices (3D-MID). Materials, manufacturing, assembly, and applications for injection molded circuit carriers]. Carl Hanser Verlag GmbH & Co. KG, 2014.-368 p./ https://doi.org/10.3139/9781569905524.
12. Vanfleteren J., Bossuyt F., Plovie B. [Flex PCB based technology for randomly shaped circuits]. CMST – Center for microsystems technology, IMEC – Ghent university, Belguim, 2017/academia.edu/78593884/flex_pcb_based_technology_for_randomly_shaped_ circuits.
13. [Laser technology for mechatronic interconnect devices MIDs]/Ipkf.com/en/industries-technologies/electronics-manufacturing/3d-mids-with-laser-direct-structuring-Ids.
14. Kamotesov S., Lombard P., Semet V. et al. [The potential of 3D-MID technology for omnidirectional inductive wireless power transfer]. 13th International Congress molded interconnect devices (MID), sep 2018, Germany. 101109/ICMID.2018.8526962.hal-02152067.
15. Piechulek N., Lei Xu, Flohlich J. et al. [Miniaturization potential of additive-manufactured 3D mechatronic integrated device components produced by stereolithography]. Micromachines, 2025, 16(1), 16/https://doi.org/10.3390/mi16010016.
16. Gibbons A. [Are stretchable electronics the next evolution in wearable technology?], 2021 /allaboutcircuits.com/news/are-stretchable-electronics-the-next-evolution-in-wearable-technology/
17. [PCB fabrication and manufacturing services] /hilelectronic.com/pcb-fabrication/?gad_ source=18.
18. Efimenko A.A. [A heuristic method for selecting the optimal design of electrical connections for electronic devices]. Proceedings of Odessa Polytechnic University, 2011. no. 2(36), pp. 228 – 233. (Rus)
19. Efimenko A.A. [Selection of optimal designs of inter-block electrical connections for electronic devices]. Radio Electronics, Computer Science, Control, 2011, no. 1, pp. 15 – 23. (Ukr)
20. Efimenko A.A. [Flexible-rigid printed circuit board and corresponding three-dimensional printed assembly on a single base]. Application for invention no. a 2025 00305. Ukraine, 01/24/2025. (Ukr)
21. Efimenko A.A. [Rigid-flexible printed circuit board on a single base]. Proceedings of the XXVI International Scientific and Practical Conference, Odesa, 2025, pp. 39 - 41. (Ukr)
22. Frolov V.A. [Analysis and optimization in applied problems of designing radio electronics devices]. Kyiv, Higher School, 1991, 310 p.